NATIONAL AERONAUTICS AND SPACE ADMINISTRATION

Space Programs Summary 37-52, Vol. I

Flight Projects

For the Period May 1 to June 30, 1968

GPO PRICE $ _____

CSFTI PRICE(S) $ _____

Hard copy (HC) 3.00

Microfiche (MF) .65

ff 653 July 65

N68-36632

(ACCESSION NUMBER) (THRU)

35 1

(PAGES) (CODE)

CR 97215 30

(NASA CR OR TMX OR AD NUMBER) (CATEGORY)

FACILITY FORM 602

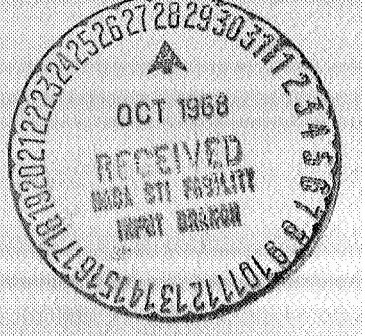

JET PROPULSION LABORATORY

CALIFORNIA INSTITUTE OF TECHNOLOGY

PASADENA, CALIFORNIA

July 31, 1968

NATIONAL AERONAUTICS AND SPACE ADMINISTRATION

Space Programs Summary 37-52, Vol. I

Flight Projects

For the Period May 1 to June 30, 1968

JET PROPULSION LABORATORY
CALIFORNIA INSTITUTE OF TECHNOLOGY
PASADENA, CALIFORNIA

July 31, 1968

SPACE PROGRAMS SUMMARY 37-52, VOL. I

Copyright © 1968
Jet Propulsion Laboratory
California Institute of Technology

Prepared Under Contract No. NAS 7-100
National Aeronautics & Space Administration

Preface

The Space Programs Summary is a bimonthly publication that presents a review of engineering and scientific work performed, or managed, by the Jet Propulsion Laboratory for the National Aeronautics and Space Administration during a two-month period. Beginning with the 37-47 series, the Space Programs Summary is composed of four volumes:

Vol. I. *Flight Projects* (Unclassified)

Vol. II. *The Deep Space Network* (Unclassified)

Vol. III. *Supporting Research and Advanced Development* (Unclassified)

Vol. IV. *Flight Projects and Supporting Research and Advanced Development* (Confidential)

Approved by:

W. H. Pickering, *Director*
Jet Propulsion Laboratory

PRECEDING PAGE BLANK NOT FILMED.

Contents

PLANETARY–INTERPLANETARY PROGRAM

I. *Mariner* Mars 1969 Project 1

A. Introduction 1

B. Project Engineering 3

C. Systems 6

D. Engineering Mechanics 10

E. Guidance and Control 25

ADVANCED STUDIES

II. Advanced Planetary Missions Technology 31

A. Introduction 31

B. Project Engineering 31

C. Propulsion 34

D. Environmental Sciences 41

I. *Mariner* Mars 1969 Project

PLANETARY–INTERPLANETARY PROGRAM

A. Introduction

1. Mission Description

The primary objective of the *Mariner* Mars 1969 Project is to make two flyby exploratory investigations of Mars in 1969, which will set the basis for future experiments—particularly those relevant to the search for extra-terrestrial life. The secondary objective is to develop Mars mission technology.

The spacecraft design concept is modeled after the successful *Mariner IV* spacecraft, considerably modified to meet the 1969 mission requirements and to enhance mission reliability.

The launch vehicle is the *Atlas/Centaur* SLV-3C, used for the *Surveyor* missions. This vehicle, developed by General Dynamics/Convair Company for the Lewis Research Center, has a single- or double-burn capability in its second stage and a considerably increased performance rating over the *Atlas D/Agena D* used in the *Mariner IV* mission.

Mariner Mars 1969 missions will be supported by the Air Force Eastern Test Range launch facilities at Cape Kennedy, the tracking and data acquisition facilities of the Deep Space Network, and other NASA facilities.

The six planetary-science experiments, selected by NASA for the *Mariner* Mars 1969 missions, are listed in Table 1.

2. Project Status

During this period, the bulk of the operations with the proof-test model (PTM) spacecraft was completed. Assembly and subsystem testing on the first flight spacecraft progressed (assembly was completed at the end of the period), and assembly of the second flight spacecraft began; some operations are ahead of schedule. A second combined subsystem test exercising the television and data storage subsystems and the image processing laboratory was conducted, generally validating these equipments and their compatibility.

A revision of the spacecraft/DSIF telecommunications interface control document and the compatibility test plan for this interface were issued. In the mission design and analysis area, the planetary quarantine plan and the mission plan portion of the mission plan and requirements document were completed. Selection of preferred arrival dates was accomplished. Design of the mission operations software system was completed, and development of the individual programs continued during the period. The eighth project quarterly review was conducted on May 21 and 22, 1968.

Table 1. *Mariner* Mars 1969 scientific investigation

Experiment	Scientific Investigator	Affiliation
Television	R. B. Leighton[a]	CIT
	B. C. Murray	CIT
	R. P. Sharp	CIT
	N. H. Horowitz	CIT
	A. G. Herriman	JPL
	R. K. Sloan	JPL
	M. E. Davies	Rand Corporation
	C. Leovy	Rand Corporation
	B. A. Smith	New Mexico State University
Infrared spectrometer	G. C. Pimentel[a]	UCB
	K. C. Herr	UCB
Ultraviolet airglow spectrometer	C. A. Barth[a]	University of Colorado
	F. C. Wilshusen	University of Colorado
	K. Gause	University of Colorado
	K. K. Kelly	University of Colorado
	R. Ruehle	University of Colorado
	J. B. Pearce	University of Colorado
	E. F. Mackey	Packard-Bell Electronics Corporation
	W. G. Fastie	Johns Hopkins University
Infrared radiometer	G. Neugebauer[a]	CIT
	G. Munch	CIT
	S. C. Chase	Santa Barbara Research Center
S-band occultation	A. J. Kliore[a]	JPL
	G. Fjeldbo	Stanford University
	S. I. Rasool	Goddard Institute of Space Science
Celestial mechanics	J. D. Anderson[a]	JPL
	W. L. Martin	JPL

[a]Principal investigator.

3. Selection of Preferred Arrival Dates

To accomplish the scientific objectives of the *Mariner* Mars 1969 missions, the principal investigators, acting in concert with the project scientist, selected the following preferred launch/arrival date combinations in early May:

(1) Early launch: July 31, 1969 arrival, equatorial pass.

(2) Late launch: August 5, 1969 arrival, polar pass.

To achieve the desired scientific objectives, it is expected to be necessary (1) to provide an intermediate scan-platform clock- and cone-angle value pair in addition to the initial and final values, and (2) to provide for a second limb crossing for the ultraviolet spectrometer (UVS) for at least one of the passes.

The selection approach consisted of an initial independent selection or identification by each investigator of the parameters that would be suitable for his experiment. Project personnel supplied the detailed trajectory, encounter, pointing, and timing data. These independent selections and supporting data were presented and discussed at a series of bi-weekly meetings from March to May, where the selection of the above dates was made.

Two basic restrictions were imposed. The arrival window was confined to the period July 27 (later revised to July 29) to August 15 and the minimum arrival day separation was 5 days. A nominal time of arrival at 2 h after Goldstone zenith toward Mars was used for the trajectory data; it is recognized that variations from this time are possible in the final selection of the detailed aiming and timing parameters.

In considering the surface features, there was general agreement on August 5 for the polar pass. This date permits viewing of many features of long-standing historical interest, some from the permanency of their visual appearance and others from their long-time, slow-rate-of-change variability. The southern wave-of-darkening will have just started over the region near the polar cap if this is a "normal" spring season. The problem of where to look for the edge of the cap is a difficult one. With the arrival date of July 31 for the equatorial pass, far-encounter pictures from this mission could be available for updating of the platform pointing and timing for the polar pass.

With an August 5 date indicated for the polar pass, the equatorial pass could be either early or late in the available arrival period and still satisfy the 5-day separation requirement. For the purpose of overlap of coverage on the lighted side, again over historically interesting areas, the early arrival was desired and the date of July 31 was indicated.

Although the descriptions given in the two preceding paragraphs are in visual imaging terms, the selection process with respect to surface features involved agreements among the infrared radiometer, infrared spectrometer (IRS), and TV investigators. Dark-side time coverage and terminator-crossing conditions for the infrared experiments can be met, since they are relatively independent of arrival date and are determined by the detailed encounter parameters. This is done by initiating the near-encounter sequence based on 24 pictures and selecting a final clock angle that provides adequate dark-side time coverage, beyond dark-limb calibration for the IRS, and terminator crossing at desirable latitudes.

To satisfy a prime requirement for the UVS, alignment of its slit at a second lighted limb crossing is required. This is caused by the sensitivity of the UVS instrument to stray light and a resulting exponential instead of a linear inverse dependence on slant range for the measurement of molecular species (specifically nitrogen) in the lower atmosphere. The slant range distances at the first limb crossing are smaller for the later arrival dates. However, even at the last possible arrival dates for a nominal closest approach of 3000 km and timing for 24 pictures, the values are too large for the accomplishment of this portion of the experiment with the degree of accuracy and sensitivity desired. The ranges are totally out of bounds for the arrival dates of August 5 and July 31 desired for surface feature coverage. Delaying the start of the near-encounter sequence sufficiently to bring the UVS slant range down could forfeit up to ⅙ to ¼ of the light-side data. A solution to this problem is to perform the lower atmosphere (400 to 100 km) portion of the UVS experiment with the scan platform at the minimum cone angle of 101 deg. The platform slew to this final cone angle would be performed earlier than in the slewing strategies previously considered.

For the equatorial pass, the effect on the other three onboard experiments is to view different areas at larger emission angles and slant ranges and smaller sun incidence angles than are needed for two or three pictures (equivalent to about 50 to 100 s of data for the infrared instruments). For the polar pass, the same solution might be possible; however, the data indicate that a forward cone slew could also be used to preserve the desirable viewing characteristics for the observation of the polar cap. There is a maximum cone-angle value imposed by the heating of the IRS radiator plate. These alternatives seem much less detrimental than shortening the light-side viewing time or decreasing the altitude of closest approach, which also is not too effective in achieving decreased slant range. It was recommended that this type of encounter strategy be used for at least one of the passes in order that the molecular nitrogen portion of the UVS experiment can be performed in an optimal manner. The same strategy could be used in both passes if the other experiments are not too degraded.

The requirements of the S-band occultation experiment are met by the selection of appropriate launch periods for the two passes. The equatorial pass provides latitudes of occultation near 10 and 80 deg independent of launch date. To obtain significant separation in latitude for the polar pass, it must be launched late. These considerations determined the association of the early launch with the equatorial pass and the late launch with the polar pass.

For the celestial mechanics experiment, there is no significant need for specific arrival or launch dates. While lower approach speeds and lower altitudes of closest approach would have some advantage, the amount of improvement in the value of the experiment is not large for the available ranges of these variables.

B. Project Engineering

1. System Integration

a. Spacecraft design considerations in selecting the spacecraft/Centaur separation orientation. The *Mariner* Mars 1969 spacecraft will be separated from *Centaur* after *Centaur* has been oriented to satisfy certain objectives. These objectives, which are related to spacecraft system design constraints, are:

(1) Provide ready sun acquisition that simplifies spacecraft turns and minimizes battery drain.

(2) Enhance acquisition ease by the DSN by directing the low-gain antenna pattern in the direction of the deep space station responsible for acquisition.

(3) Prevent the sun from entering the field-of-view of the Canopus tracker or the science instruments.

The spacecraft tip-off rates will be 3 deg/s maximum and about 1 deg/s minimum. Assuming the minimum value, it is possible for the spacecraft to drift 17 deg before the attitude control stops the rotation. In addition, the spacecraft can drift during the time it is in the earth's shadow at a rate of ± 0.3 mrad/s due to the rate deadband. From available curves it appears that the time spent in the shadow, after *Centaur* separation, could be as long as 35 min. Assuming the shadow time is minimal, the spacecraft could drift up to 16 deg around each axis.

For optimistic drift rates, it appears that the spacecraft can drift 33 deg from its separation vector before sun acquisition begins or it can drift 208 deg if the maximum rates occur. This indicates that the spacecraft separation should occur along the sunline. However, this analysis is preliminary and further studies will be conducted.

b. Analysis of PTM chamber test maximum power data. The highest power loads observed during the proof-test model (PTM) chamber tests appear to have occurred on May 19, 1968, at which time DC-25 (near-encounter phase) was in effect, gyros were on, and near-earth

voltages were being simulated. Analysis of the power data (Table 2) shows the spacecraft to be running slightly lower in power than the allocated levels when everything is on and turning.

Table 2. PTM chamber test power data

Power parameter	Main inverter output, W	Booster regulator output, W
Rating[a]	200	250
Observed[b]	174	203
Correction[c]	31	33
Estimated actual[d]	205	236
Allocated[e]	218	263

[a]Maximum steady-state rating.
[b]Data from system test complex data system telemetry.
[c]Additional loads at full near-encounter power (i.e., additional 21 W when both data storage record motors running, additional 10 W when scan motor slewing).
[d]Sum of observed and correction.
[e]Power calculated by power profile based on allocated values.

2. Spacecraft System Test and Operations

a. Introduction. Mariner Mars 1969 spacecraft system test and operations progressed on schedule during May and June 1968 (see SPS 37-50, Vol. I, Fig. 10, p. 42). Some electrical operations on spacecraft M69-2 and M69-3 (first and second flight spacecraft, respectively) were performed ahead of schedule due to early delivery of some equipment and on-time delivery of other units. During May and June the major portion of the proof-test model (PTM) spacecraft system test program was completed and all environmental testing (space simulation, vibration, acoustic, and pyrotechnic shock) was completed.

b. Spacecraft M69-1 (PTM).

Space simulation test, part I. Part I of the space simulation test began on April 26, 1968 (SPS 37-51, Vol. I) and was terminated after 115.5 h of spacecraft operation in the vacuum environment because of the failure of certain science instrument operational support equipment (OSE) stimuli that required repairs before the test could be resumed with satisfactory results. During the break, other repairs and improvements in the spacecraft configuration were also made. Part I was resumed on May 4 and continued satisfactorily through completion on May 10, accumulating 124.8 h of spacecraft operation after the break.

Space simulation test, part II. Spacecraft M69-1 was prepared for part II of the space simulation test during the period May 10–13. Preparation included the removal of externally mounted test equipment, stimuli, test cables, and other hardware that would interfere with the compilation of good data for temperature control subsystem performance evaluation.

Space simulation test, part II, was satisfactorily conducted during May 13–20 in the 10-ft space simulator. Part II of the test was developed to verify spacecraft temperature control design. In addition, spacecraft temperature control margins were verified by operating the spacecraft in hot and cold temperature configurations. Following completion of part II, a system verification test was performed that demonstrated the spacecraft had not been degraded by the thermal environment.

Vibration test. The PTM spacecraft was returned to the spacecraft assembly facility on May 21 for the vibration test. Preparation included assembly of the spacecraft to the launch configuration (installation of solar panels, etc.) and the installation of instrumentation accelerometers at key locations. Final preparation was completed on June 3 after the spacecraft was installed on the vibration equipment in the environmental and dynamics test laboratory.

The vibration test was performed during the period June 3–7 to verify that the spacecraft would operate satisfactorily during and after exposure to vibration levels based on the expected environment from the *Atlas* and *Centaur* launch vehicles during the boost phase. The spacecraft was vibrated in three different axes: (1) the Z axis, (2) the X axis (vibration equipment attached to bay I), and (3) an X–Y axis (vibration equipment attached to bay VIII). Following vibration in each axis, a brief test was performed to verify that spacecraft performance had not been degraded by vibration.

Acoustic test. An acoustic test was performed on June 10 in the acoustic chamber. The purpose of the acoustic test was to evaluate the performance of the PTM spacecraft during exposure to type-approval acoustic levels based on the expected environment from the *Atlas/Centaur* at liftoff. No spacecraft problems were observed during the test. A spacecraft verification test was satisfactorily completed following the acoustic test.

Pyrotechnic shock test. A pyrotechnic shock test was performed on the PTM spacecraft to: (1) evaluate spacecraft operation during the detonation of pyrotechnic devices, (2) determine the nature of pyrotechnic shocks by measurement with accelerometers, and (3) demonstrate spacecraft pyrotechnic compatibility with the electromagnetic interference sources encountered on the launch complex at the Air Force Eastern Test Range

(AFETR). During the test on June 12, the spacecraft was operated through significant portions of its flight sequence while each spacecraft pyrotechnic device and the spacecraft/*Centaur* adapter V-band pyrotechnics were fired at the appropriate time. Spacecraft operation throughout the test was nominal.

Weight, center of gravity, and propulsion subsystem alignment. Spacecraft M69-1 weight, center of gravity location, and the required adjustment to the propulsion subsystem thrust axis were measured on June 14 and 15. Spacecraft weight was 835.9 lb. The measured center of gravity location in spacecraft coordinates was $\overline{X}=+0.456$ in., $\overline{Y}=+0.473$ in., and $\overline{Z}=-9.034$ in. The alignment error after adjustment of the propulsion subsystem thrust axis was 0.019 in.

Simulated precountdown. The launch precountdown test was simulated on June 21. The purpose of the precountdown was to perform the most detailed spacecraft verification permitted within the limits of the launch configuration and the launch complex equipment (LCE). No significant problems were encountered during the precountdown operation.

Simulated countdown. On June 24, a simulated countdown was performed on the PTM spacecraft using the LCE and system test complex. The purpose of the simulated countdown was to provide training for personnel who take part in the spacecraft launch operations at AFETR and to develop an optimum sequence for conditioning the spacecraft for launch and taking engineering measurements that will aid in postlaunch acquisition and spacecraft performance analysis. During the test, several prelaunch conditioning problems were observed that would have caused holds in the spacecraft countdown.

Power transient and power profile measurements. A combined power profile and power transient measurements were performed on June 26 and 27 after the spacecraft had been restored to the system test configuration following the simulated countdown. The purpose of the power profile was to determine the power dissipation of each spacecraft subsystem in all of its pertinent steady-state electrical modes of operation. The purpose of the power transient survey was to obtain oscilloscope photographs and oscillograph recordings of transients associated with subsystem power changes, individually and in logical combinations. Spacecraft operation was nominal during both operations and good data were obtained.

c. Spacecraft M69-2.

Assembly. Assembly of spacecraft M69-2 began on May 22, 1968 when the octagon structure and superstructure were installed on the low-level positioner. As flight-qualified equipment became available, they were installed. By the end of June, spacecraft M69-2 assembly was largely completed.

Power subsystem test. A test was performed on June 6 to verify proper operation of the spacecraft power subsystem before applying spacecraft power to other spacecraft subsystems. No major problems were encountered during the test.

Initial power application. Initial power application to spacecraft subsystems commenced on June 7 and continued through the remainder of the month. The objective of the initial power application procedure was to safely apply spacecraft power to the newly assembled spacecraft. Consequently, a detailed procedure was used in which several key parameters were measured for each power line. Cognizant personnel representing both sides of the power interface were required to agree that the measurements were correct before the interface could be connected.

Subsystem interface tests. Subsystem interface testing began on June 7, shortly after initial power application began. Interface tests were conducted to: (1) minimize the chance of equipment damage caused by improper interfacing, and (2) functionally test all interfaces between subsystems and verify agreement of their signal characteristics with applicable documentation. The duration of interface and subsystem testing is dependent on the availability of other subsystems and the number and complexity of the interfaces involved.

Subsystem tests. Following the verification of subsystem interfaces, each newly installed subsystem underwent a detailed subsystem test. The subsystem test provided a detailed evaluation of subsystem performance while operating on spacecraft power and allowed a preliminary determination of any possible effects the subsystem may have had on the spacecraft environment.

d. Spacecraft M69-3.

Assembly. Assembly of the second flight spacecraft (M69-3) began following the installation of the spacecraft structure on its low-level positioner on June 18, 1968. Assembly started on schedule.

Power subsystem test. The initial portion of the power subsystem test was performed on June 27. No significant problems were encountered.

C. Systems

1. Planetary Quarantine

The planetary quarantine plan was completed and published in late May; some of its considerations are presented in this article.

The probability P_C of contaminating Mars with viable terrestrial organisms carried on, or ejected from, the *Centaur* launch vehicle or *Mariner* Mars 1969 spacecraft is allocated among identified potential sources of contamination.

A mathematical model is developed to investigate the contribution of each of the ejecta sources. A value of $P_C = 3 \times 10^{-5}$ for each flight is then apportioned between the ejecta sources, as one class, and *Centaur* or spacecraft impact, as another class. The resulting apportionment of P_C for each launch is

$$P_{C_{alloc}}(LP) = 2.4 \times 10^{-5} \quad (1)$$

$$P_{C_{alloc}}(SP) = 6.0 \times 10^{-6} \quad (2)$$

where

$P_{C_{alloc}}(LP)$ = portion of P_C allocated to large population sources (*Centaur* or spacecraft impact)

$P_{C_{alloc}}(SP)$ = portion of P_C allocated to small population sources (*Centaur* or spacecraft ejecta)

To meet the apportioned probability of contaminating the planet with large population sources, the launch vehicle target point will be biased by a precalculated amount for each launch/arrival date combination. The launch vehicle firing tables will implicitly incorporate these biases.

Figure 1 is a branch diagram of the probability of *Centaur* and/or spacecraft impact. The diagram can be simplified to that portion shown in solid lines, if the following assumptions are made:

(1) Given that the launch vehicle (LV) executes a deflection maneuver, $P_I(LV) \ll 10^{-5}$.

(2) The spacecraft will not experience an attitude-control (AC) gas valve failure.

(3) Given that the spacecraft executes two maneuvers, $P_I(SC) \ll 10^{-5}$.

(4) One maneuver is always required.

It can be shown that these are valid assumptions; thus, the simplified branch diagram is used.

The small population sources of contamination that have been identified are listed in Table 3. Each of the sources was examined, and the probability of contaminating Mars was determined. From this, the overall probability of contaminating Mars with organisms from small population sources was calculated by

$$P_C(SP) = \sum_{i=1}^{10} P_C(SP_i) \quad (3)$$

Table 3. Probability of contaminating Mars with small population sources

Source of contamination	$P_C(SP_i)$, nominal estimate	$P_C(SP_i)$, conservative estimate
Centaur AC engine exhaust products	nil	nil
Centaur vernier engine exhaust products	nil	nil
Centaur main engine blowdown products	nil	nil
Centaur outgassed material	nil	nil
Centaur surface material	nil	5.5×10^{-8}
Spacecraft outgassed material	nil	nil
Spacecraft midcourse motor exhaust products	nil	nil
Spacecraft surface material	7×10^{-12}	2.2×10^{-8}
Spacecraft AC gas	2.2×10^{-11}	9.8×10^{-7}
Infrared spectrometer coolant gases	nil	nil
	2.9×10^{-11}	3.2×10^{-6}

Table 3 contains the calculated values of $P_C(SP_i)$ that are based on conservative and nominal estimates of the contamination event probabilities and number of organisms. There are nine contamination event probabilities, such as P_{E_i}, the probability that viable organisms are ejected by the ith source; P_{SE_i}, the probability that viable organisms survive the ejection process; etc.

The allocation to $P_C(SP)$ is based on the conservative values from Table 3.

$$P_C(SP) = 5.5 \times 10^{-8} + 2.2 \times 10^{-6} + 9.8 \times 10^{-7}$$
$$= 3.2 \times 10^{-6}$$

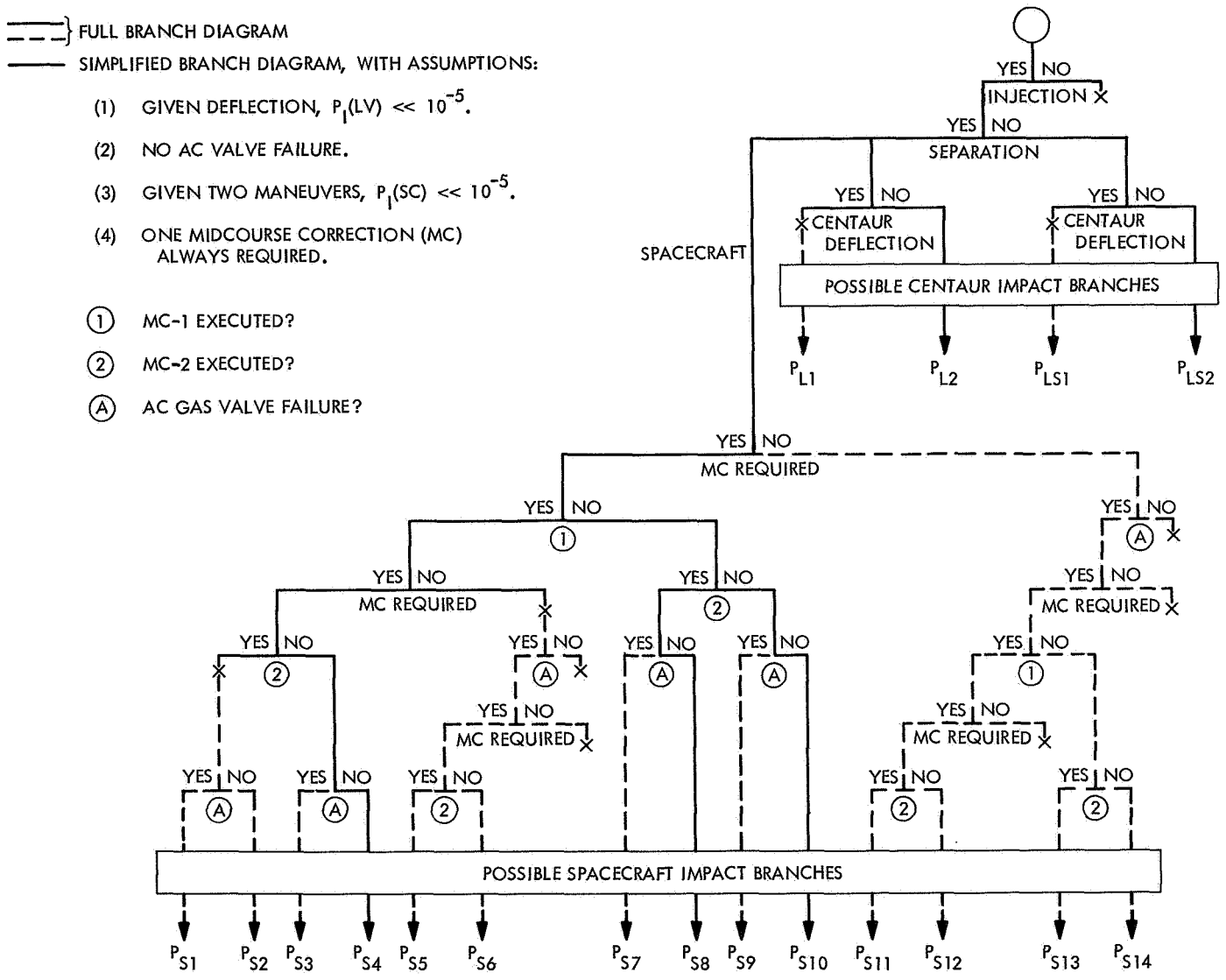

Fig. 1. Full and simplified branch diagrams of probability of Centaur/spacecraft impact

To account for the possibility that additional small population sources may be identified, the final allocation to small population sources is increased to

$$P_{O_{allloc}}(SP) = 6.0 \times 10^{-6}$$

The remainder of the 3.0×10^{-5} is allocated to large population sources, and, thus, Eqs. (1) and (2) are applicable.

2. Launch/Arrival Targeting Plan

A flexible targeting plan has been adopted and is illustrated in Fig. 2. The plan features near-uniform distribution over the launch/arrival date space, as a base, plus 13 launch dates for each of two preferred arrival dates. There are a total of 76 launch/arrival date combinations, including the 26 for the current preferred arrival dates of July 31 and August 5, 1969. The other arrival dates are being targeted to cover the possibility that different preferred dates may be selected before actual launch.

Two important effects of the difference in the rotational rates between earth and Mars are:

(1) For each earth day of delay in arrival, the longitude band surveyed would shift by ≈ 9.7 deg to Mars' east.

(2) For each hour of delay in arrival, the longitude band surveyed would shift by 14.6 deg to Mars' west.

Thus, a 40-min shift in time of arrival would cause the spacecraft to observe a longitude band that corresponds to a 1-day shift. The spacecraft has sufficient maneuver capability to easily allow a 40-min change in time of arrival while at the same time having no detrimental effect on the distance the aim point can be moved in the B-plane. Hence, any targeted arrival time could be changed to represent an effective 1-day change in arrival date; thus, the launch/arrival date pairs in Fig. 2 cover the longitude band for essentially every day in the arrival period.

Examination of Fig. 2 reveals that there are 39 distinct launch dates (most with more than one arrival date). Of these dates, all but eight correspond to an arrival date that is one of the preferred arrival dates or is within one day of one of the two preferred dates. Thus, there are 31 launch days (out of 39) when the spacecraft can view

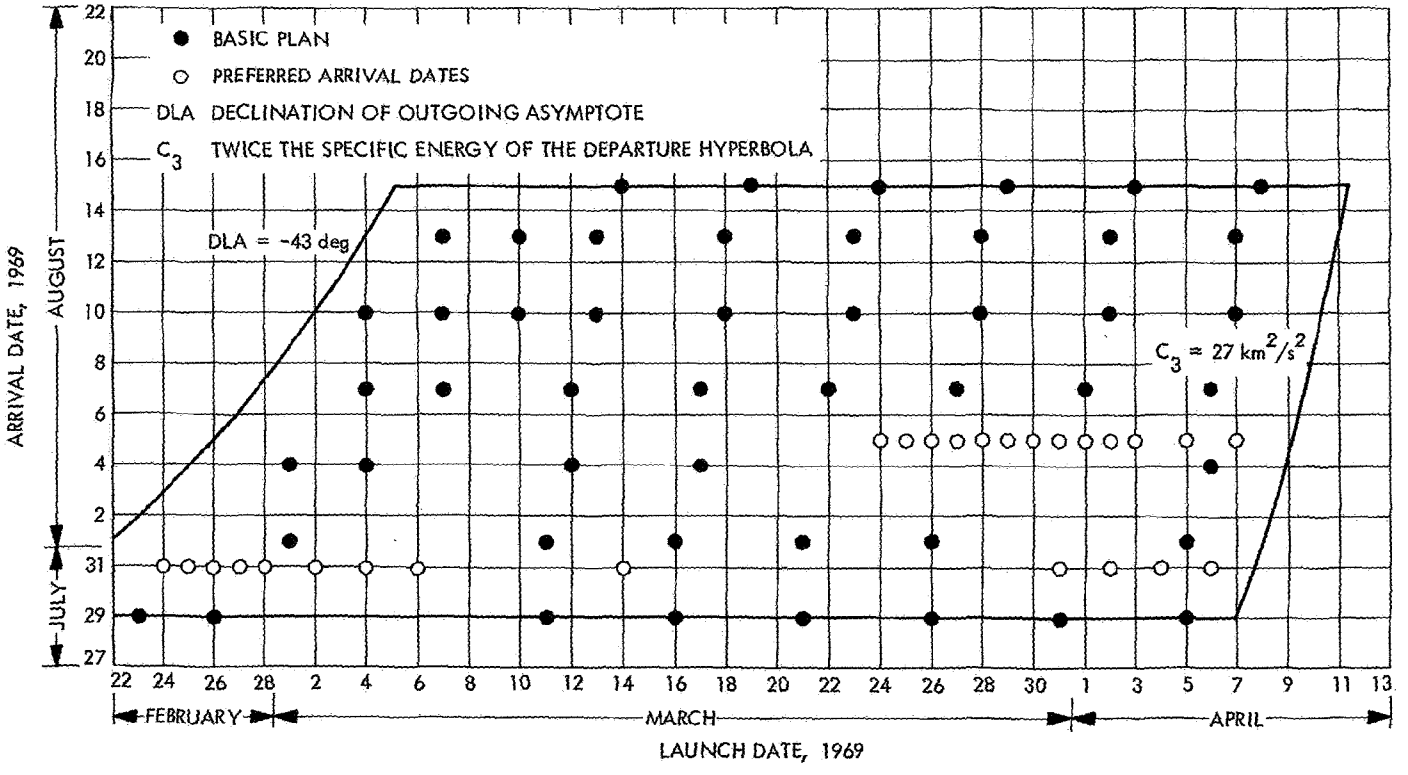

Fig. 2. Launch/arrival targeting plan

the longitude band corresponding with one of the presently preferred arrival dates.

3. System-Test-Complex Data System

During this period the system-test-complex data system (STCDS) provided support for parts I and II of the proof-test model (PTM) space simulator test and for several types of environmental PTM tests. The simulator and environmental tests required relocation of the data input subsystem (DIS) and data display equipment in a facility remote from the computer and use of 4000-ft cables to communicate data to and from the computer. This mode of operation may have aggravated printer problems encountered in normal operations and introduced some additional ones.

Two program assemblies were made, each including increased processing capability relative to the previous versions, and assembly of all the fixes or "patches" made to correct software errors in the previous version.

The test director display and its associated software were developed to an operational condition, including the addition of a data channel required to communicate program control information from the remote display keyboard to the computer. The display also includes a small line printer and a cathode-ray tube (CRT) unit which displays different "pages" of test data on request by the test director in a format similar to that available on the subsystem line printers located on the system-test complex.

All modules required for the second DIS were received and assembled into the six equipment housing racks that constitute DIS-2. The signal input cable junction module was also constructed and installed, and taper-pin interconnection of input signal terminals with module terminals was begun. The input subsystem and the second unit of the test director display were expected to be tested and ready for user acceptance by mid-July. This equipment will essentially complete two data systems that provide for simultaneous test support of the two system-test complexes used primarily to qualify the flight spacecraft. The DIS was assembled on a very tight time schedule, and, because of the late availability of DIS-2, interfacing of the STCDS with the test complex for the first flight spacecraft was accomplished using DIS-1, which supported the PTM testing.

The low-speed analog data system and its interfaces with the PTM spacecraft are not yet tested or operational. The plan to acquire a second such module for DIS-2 was canceled. However, the high-speed analog data system used to support autopilot tests is now operational, and both the low- and high-speed modules will probably be shared between the two test complexes.

The efficiency of the 16.2-kbit/s real-time processor (SPS 37-51, Vol. I) was improved and the processor is presently awaiting acceptance test. This processor will provide printing and limited real-time plotting of the ultraviolet/infrared spectrometer spectral data, and will be supplemented by a nonreal-time plotting capability using the STCDS image processing laboratory-formatted tapes as a data source. This plotting capability uses the direct-couple computer system in the scientific computer facility and its associated Stromberg-Carlson Corporation 4020 high-speed CRT plotter for rapid production of science data plots.

During PTM test support, overall STCDS performance was somewhat marginal; i.e., a lower than desired probability of support at scheduled or committed times was obtained. Also, specific hardware and software difficulties, some of a recurring nature, reduced reliability during support periods to a level less than that expected. The principal problems were in the following areas: (1) continued hangups (stoppage of printing) and garbled printer text on the systems line printer, (2) deficiencies in the processing of the 16.2-kbit/s data stream and in some of the engineering and science special processors, (3) perturbation of memory cells by some software anomaly, (4) various problems relating to technical and operational support and real-time maintainability of the system, and (5) failure to obtain correct operation of some types of data modules.

A problem-failure reporting system was set up to provide a quick means for communicating failure information to the STCDS staff. All significant problems were evaluated in terms of the level-of-effort required to remedy them, and appropriate action items were assigned. Solutions have been proposed for all major problems encountered during PTM test support activities.

A tape recording system was set up for recording all serial PTM spacecraft data streams so that simulation data could be reproduced for use in data system checkout instead of real spacecraft data. Software drivers and hardware simulators proved valuable in the development and preliminary checkout of STCDS software, but proved to be consistently inadequate for use in final acceptance tests because of the fixed data formats characteristic of such simulators.

D. Engineering Mechanics

1. Introduction

The engineering mechanics effort for *Mariner* Mars 1969 includes responsibility for four subsystems (structure, cabling, temperature control, and mechanical devices) and a number of broad supporting functions (mechanical systems, applied mechanics, electronic parts engineering, materials engineering, and electronic packaging). Mechanical systems and electronic packaging, together with elements of other functions, are part of the spacecraft mechanical design. The applied mechanics function includes structural and dynamic analysis and testing, with particular attention to launch-phase dynamics. Progress of the subsystem and supporting efforts has been reported in SPS 37-41, -42, -44, and -46, Vol. VI, and SPS 37-49, Vol. I.

2. Spacecraft Mechanical Configuration

The *Mariner* Mars 1969 spacecraft mechanical configuration has been established since last reported (SPS 37-44, Vol. VI). The current spacecraft configuration and its subsystems are shown in Fig. 3. Basic changes from the *Mariner* Mars 1964 configuration not previously reported are:

(1) A half set of temperature control louvers has been attached to the ultraviolet spectrometer to obviate large temperature changes that could occur as a result of power fluctuations and thermal test and analysis uncertainties.

(2) The design of the thermal shield covering bay II (the propulsion subsystem) has been established. It is shaped to allow adjustment of the propulsion assembly to point the thrust vector through the spacecraft center of mass.

(3) The optics cover for TV camera B has been removed from the spacecraft design although the capability to replace it is retained.

3. Structure Subsystem

The *Mariner* Mars 1969 structure subsystem has been fully flight qualified for all structural loads anticipated during the mission. None of the structural components required any design modification as a result of the qualification program. Figures 4 through 7 illustrate some components of the structure subsystem.

The most serious problem encountered during the fabrication of the structure subsystem elements was the difficulty of producing adhesive bonded joints that would meet the requirements of the hardware design. The two hardware elements that contain critical bond joints are the solar panel structure and the high-gain antenna structure.

During production of the solar panel structures, a very serious problem was discovered by routine quality assurance testing of adhesive peel-strength. Production peel-test sample results and an extensive laboratory-controlled peel-test program have supported the conclusion that a structurally unacceptable bond joint (bonding failure) can result even though procedures reflecting current industry standards are followed for cleaning and bonding aluminum. The acid etch solution, when mixed exactly to specification in clean glass containers, has randomly produced weak bond joints (less than 10% of normal joint peel-strength). These low-peel strength bond joints exhibit a dangerous lack of resistance to bond-line fracture propagation. Unfortunately, sufficient data to specify an etch solution that will consistently produce high-peel-strength bond joints in aluminum structures are presently not available.

The random nature of the bonding failure made it possible that a weak structural bond could have occurred in any of the bonded structures, even though the associated process control bonding samples were of good quality. Since no immediate solution to the bonding problem existed, the *Mariner* Mars 1969 solar panels were fabricated using the existing cleaning and bonding procedures and then proof-loaded in such a manner that the critical bond joints were certified to be structurally sound.

In previous spacecraft programs the certification of bond quality on honeycomb core-to-face-skin bond lines has been based largely on the results of sample coupon testing and visual verification that the flight part was cleaned and bonded in accordance with current procedures. To assure the discovery of any low-strength bonding and of any voids in the bond line, a method of pressurizing the *Mariner* Mars 1969 high-gain antenna honeycomb structure was developed that proof-loads the core-to-face-skin bond line, thereby certifying it to be structurally sound.

When this inspection method is applied to heavy honeycomb structures with thick face skins (0.016 in. or greater), it will only detect very large voids in the bond line. Its primary usefulness in this case is that of general proof-loading of the bonded joints. By contrast, when the pressure inspection method is applied to thin face-skinned

FOLDOUT FRAME 1

FOLDOUT FRAME 2

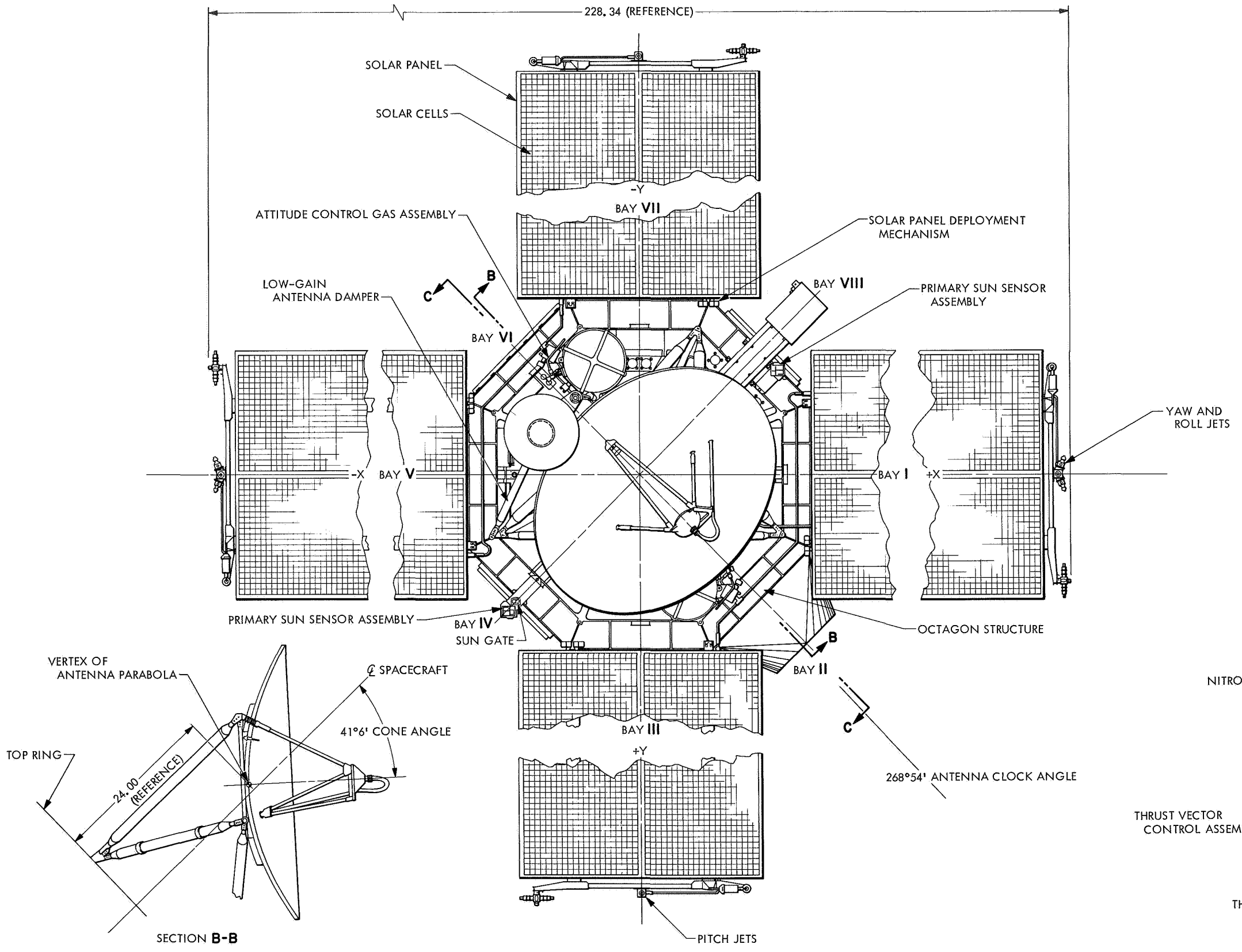

FOLDOUT FRAME 3

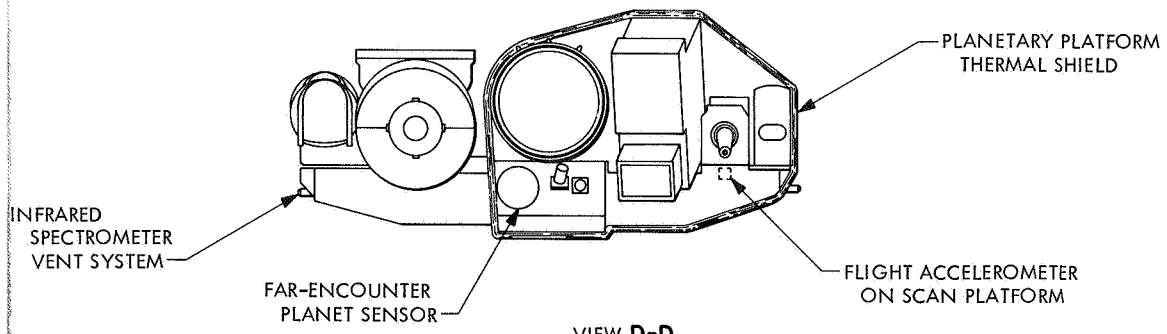

VIEW **D-D**
(ROTATED 84° COUNTERCLOCKWISE)
(LOUVER OMITTED FOR CLARITY)

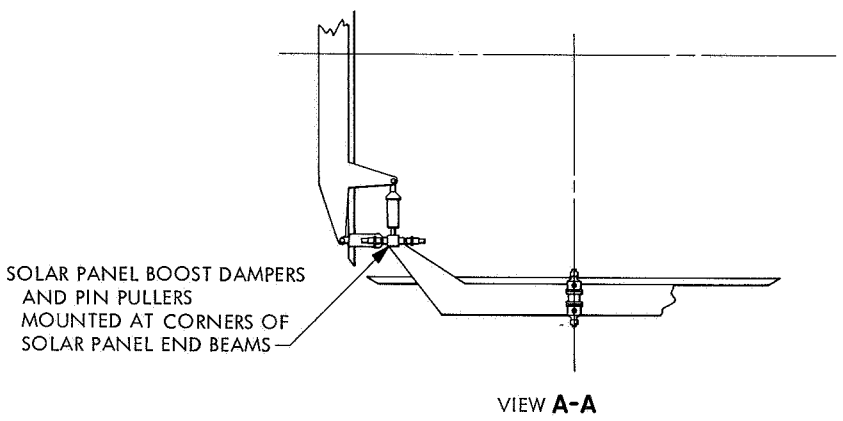

VIEW **A-A**

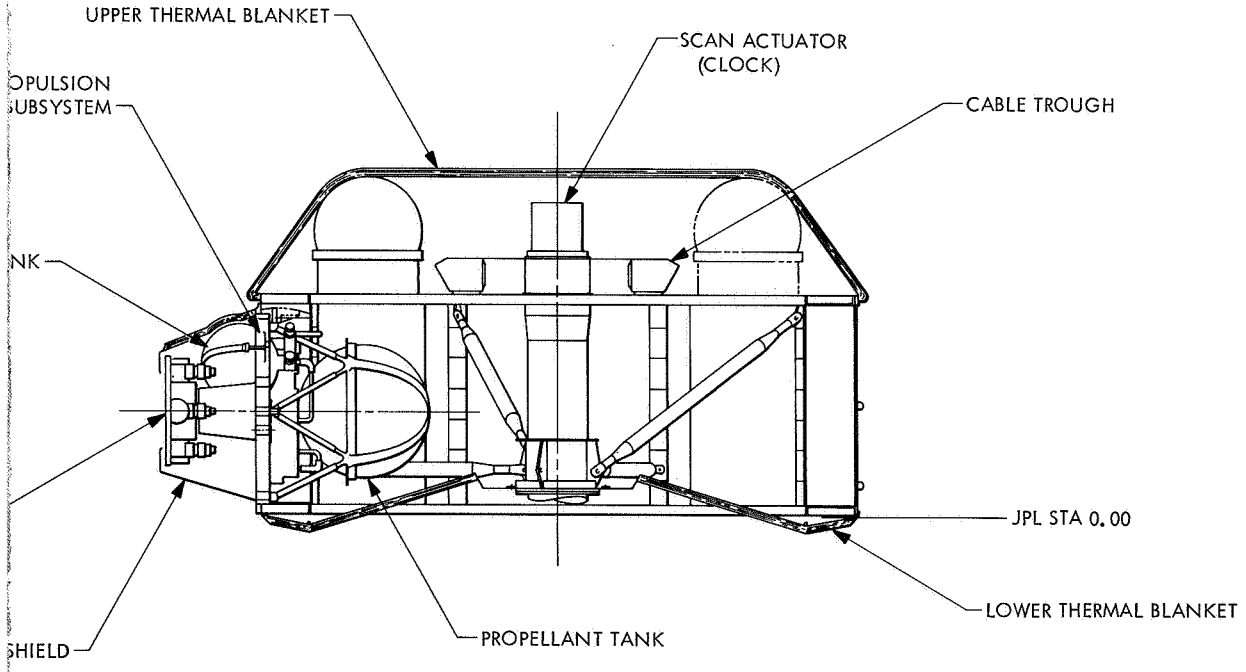

SECTION **C-C**
(ROTATED 135° CLOCKWISE)

FOLDOUT FRAME 4

FOLDOUT FRAME 5

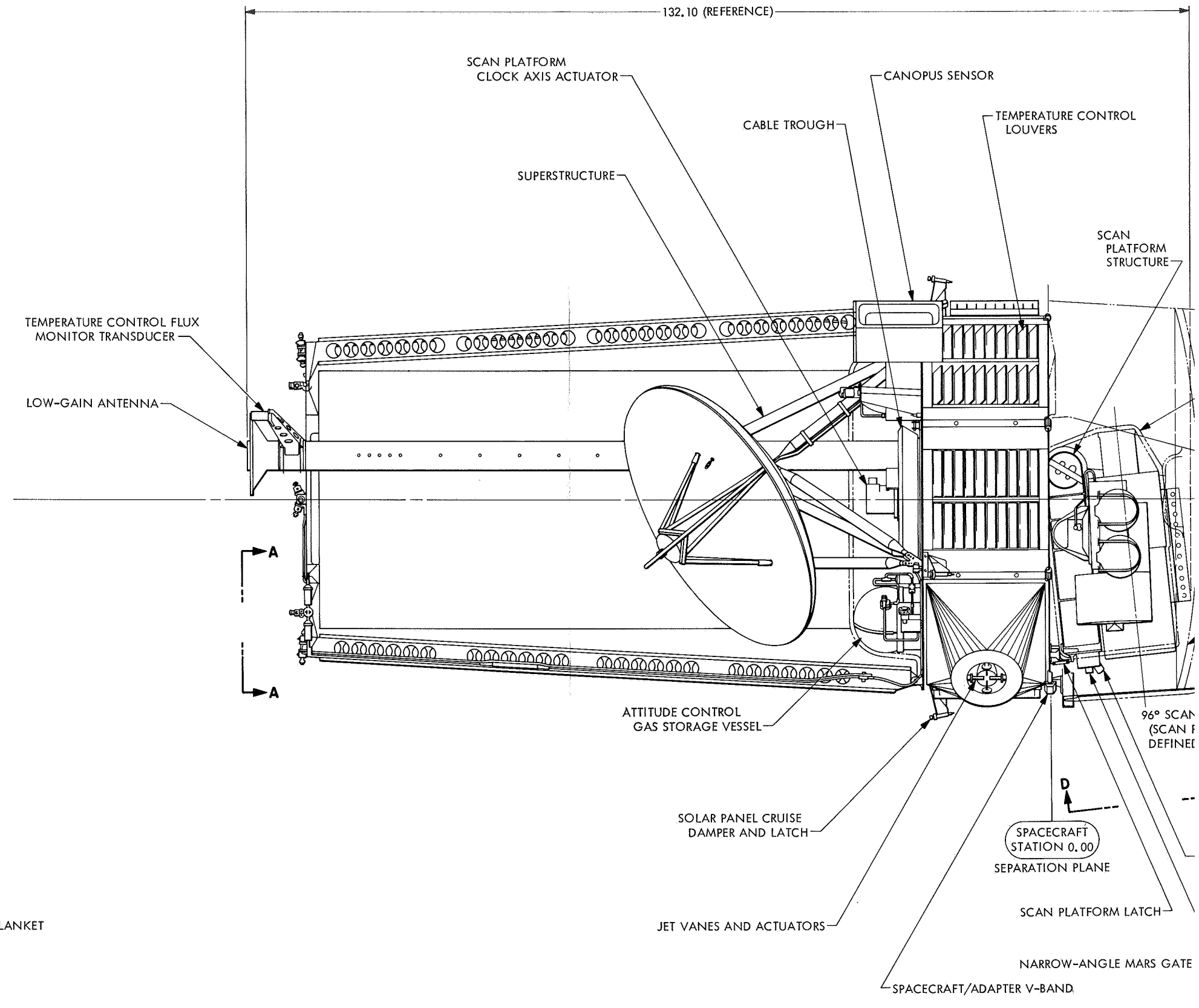

FOLDOUT FRAME 6

FOLDOUT FRAME 7

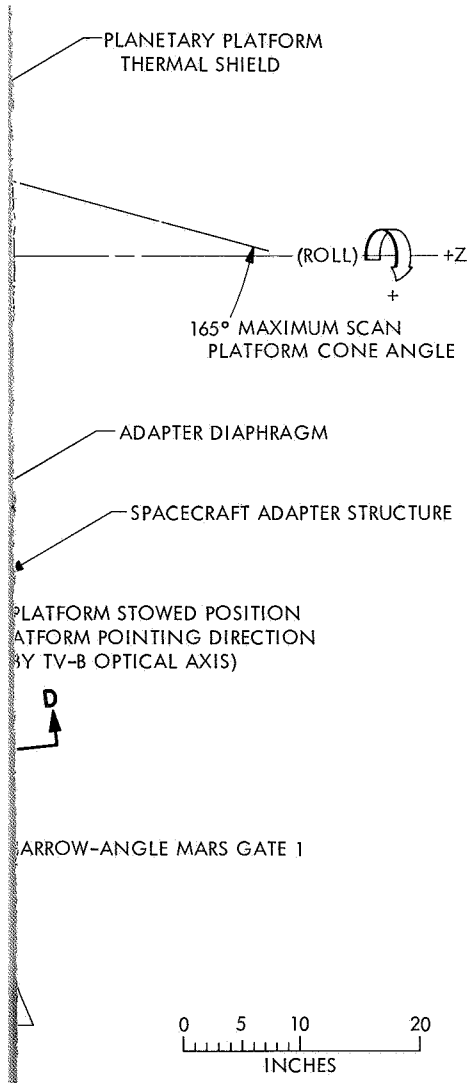

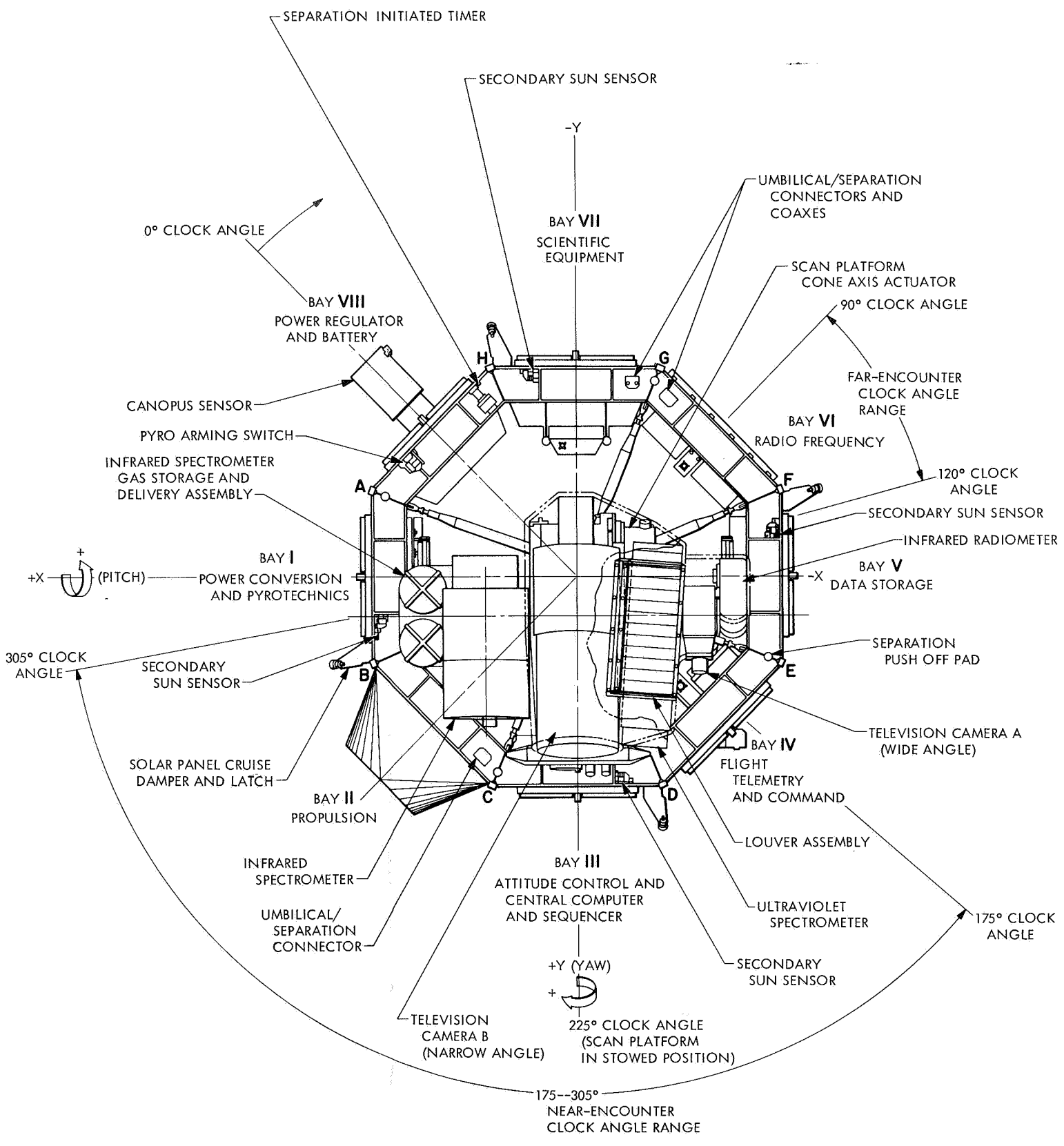

Fig. 3. *Mariner* Mars 1969 spacecraft mechanical configuration

PRECEDING PAGE BLANK NOT FILMED.

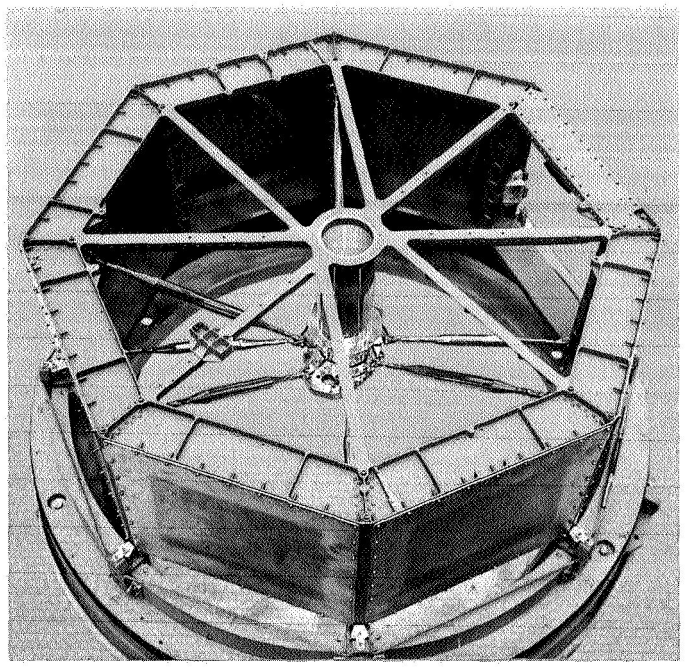

Fig. 4. Spacecraft octagonal structure

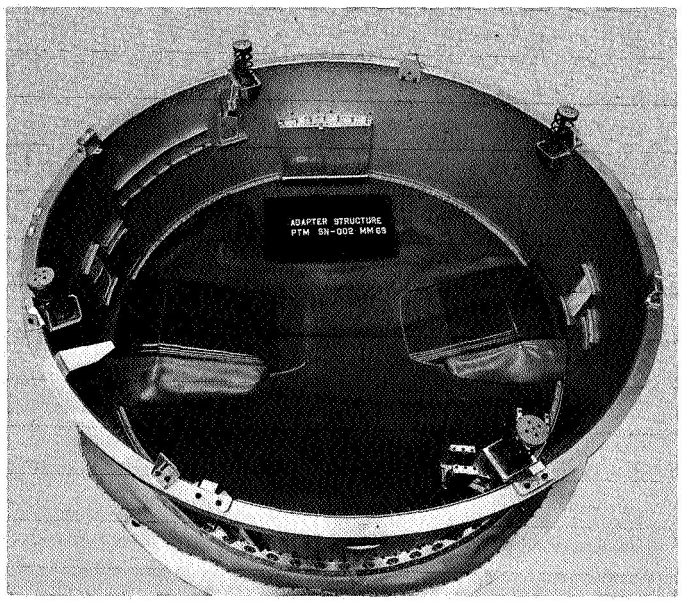

Fig. 5. Spacecraft adapter

honeycomb (0.005 in. or less, as in the high-gain antenna), it can detect voids as small as 0.10-in. diam, thus providing significant new information about the bond line in addition to the simple *go, no-go* results of the proof pressure loading.

The pressure testing of the high-gain antenna honeycomb structure was achieved by (1) simultaneously sealing the edge of the honeycomb sandwich with a core fill material, and potting copper-tube pressure taps into the edge seal, and then (2) injecting air into the sandwich through the pressure taps. A few seconds were required for the pressure in the sandwich to equalize through the perforated core; then the face skins were inspected for bulges, which indicated bond-line voids. The entire process required approximately 1 day and replaced a less informative ultrasonic inspection method requiring approximately the same length of time.

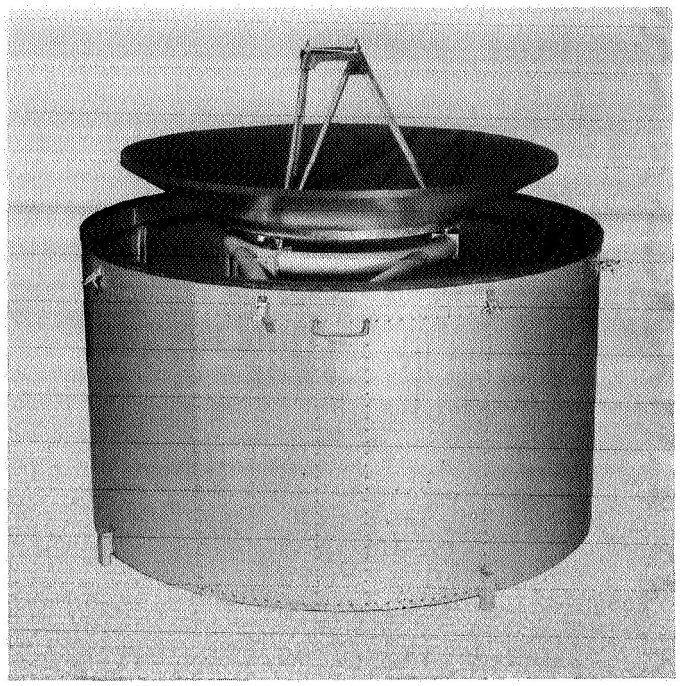

Fig. 6. High-gain antenna

4. Cabling Subsystem

The cable harnesses for the seven bay-mounted electronic assemblies utilized in *Mariner* Mars 1969 consists of three distinct types:

(1) *Mariner* Mars 1964 configuration, adapted for use on electronic assemblies I, IV, V, and VI.

(2) A new *Mariner* Mars 1969 design developed for use on electronic assemblies III and VII.

(3) A modified *Mariner* Mars 1964 version for use on electronic assembly VIII.

In the adaptation of the *Mariner* Mars 1964 configuration, several minor design changes were incorporated to aid in the fabrication and use of the support hardware. The cable support brackets were redesigned to allow separation of the support tubing from the center support

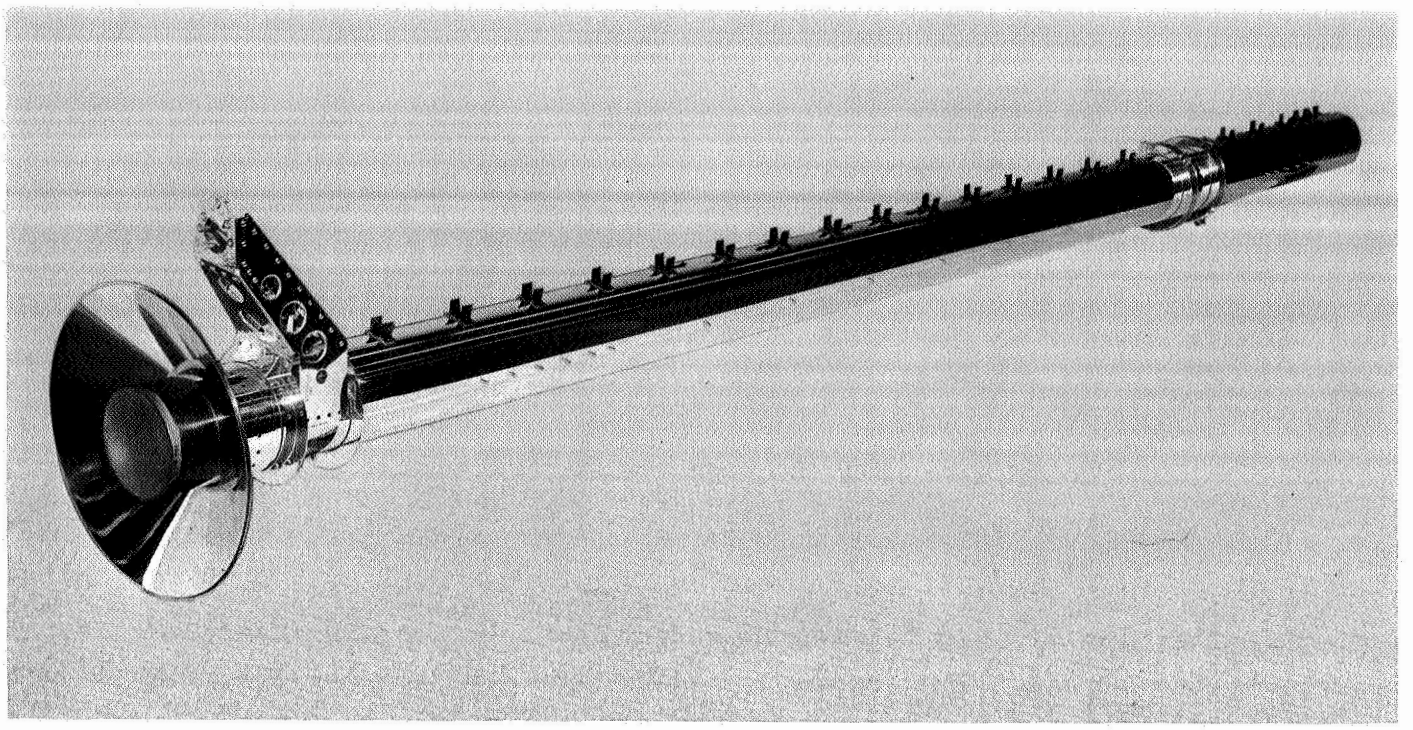

Fig. 7. Low-gain antenna

post. The center support post itself is a new design that attaches to and becomes a part of the electronic assembly chassis. The direct access connectors, formerly located on the lower cable support bracket, were transferred to the upper support bracket. This design was necessitated because of the very limited access to the lower cable support brackets when the *Mariner* Mars 1969 science scan platform is in the latched position.

In electronic assemblies III and VII, previously described in SPS 37-41, Vol. VI, a new rack and panel plug-in arrangement was developed. The cable design required to conform to the new configuration consisted of two widely separated core sections supported by two integral stiffening rails running the full length of the chassis. End brackets are provided to support the interfacing connectors that connect to the spacecraft lower ring harness and to the operational support equipment direct-access connectors. The connectors are floated on the cable side, while the mating connectors on the electronic module carry two alignment pins to engage and align the cable connectors before mating.

Potting techniques, used to provide strain relief for cables that are excessively flexed, are not required by this design. A new sealing process using CRN shrinkable tubing and Solithane 881 was incorporated, which allows limited contact motion while simultaneously protecting the normally exposed contact area from contaminants. The design also simplified rework capability of the cable harness.

Electronic assembly VIII is the power regulator assembly and is a new design for the *Mariner* Mars 1969 spacecraft (Fig. 8). This assembly is a composite of the other two types. The cable is supported by a single rail and connected to the spacecraft structure and electronic assemblies in a manner similar to that of the *Mariner* Mars 1964. Connector-supporting end-plates are not included because the battery rides "piggy-back" on the inboard surface of bay VIII, which necessitates a shallow design for the electronics modules. The cable then must lie as flat as possible to avoid interference with the installation of the battery and possible damage to the cable.

5. Applied Mechanics

Confidence in the structural integrity of the spacecraft has been achieved from a combination of analysis and development tests. This complementary, integrated program provides a basis for analytical extrapolation to modified designs or failure mode conditions.

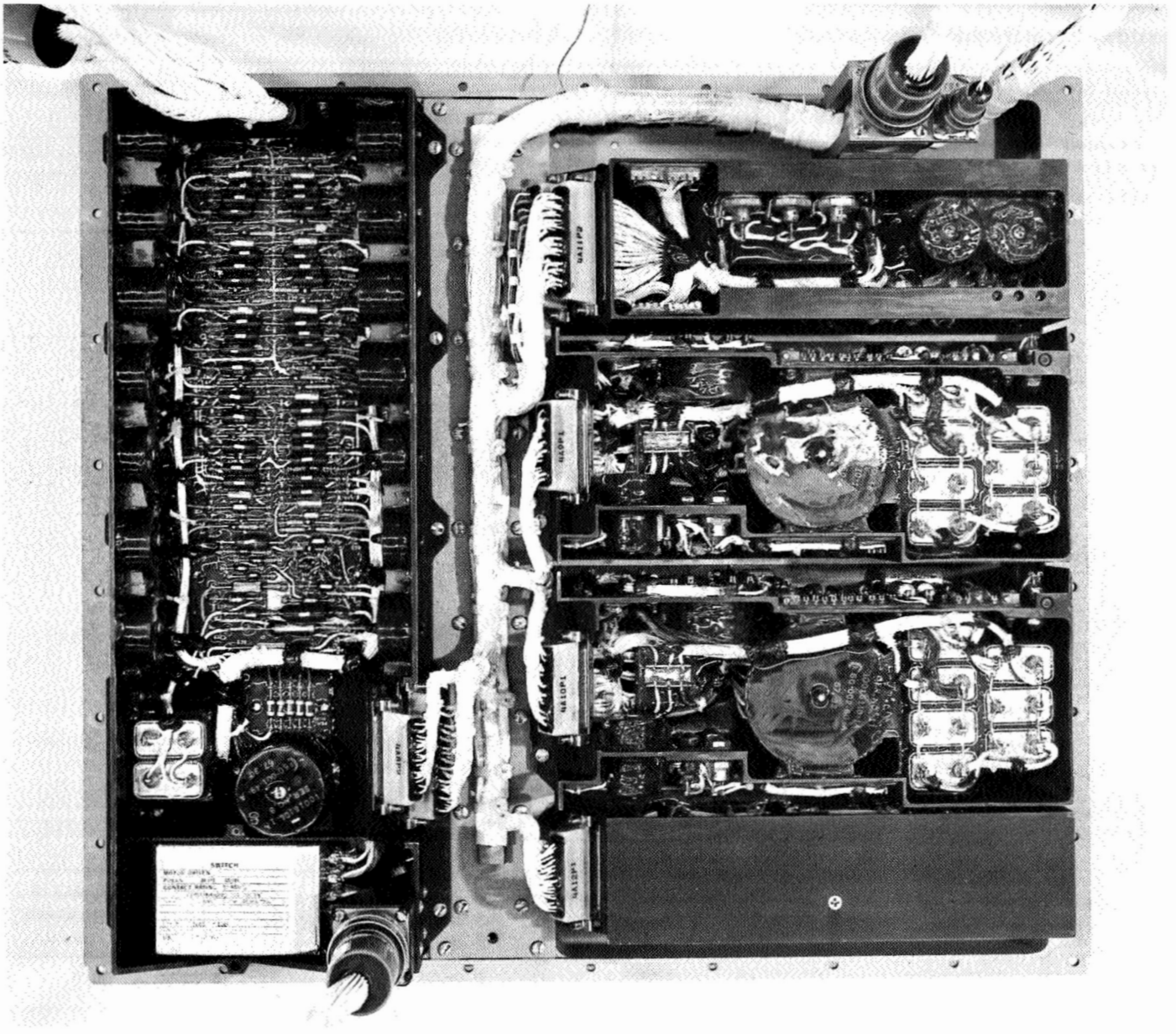

Fig. 8. *Mariner* Mars 1969 electronic assembly VIII cabling

a. Analysis. The primary objectives of the analysis program are to support design decisions, to provide pretest confidence, and to form the basis for responding to later problems and changes. The procedure used to attain these objectives has been greatly facilitated by the use of two large computer programs denoted as structural analysis and matrix interpretive system (SAMIS) (Ref. 1) and modal combination (Ref. 2).

The SAMIS program was used to predict the static and modal characteristics of the structural subsystems individually and in various combinations. Figure 9 indicates how a typical subsystem was idealized as a mathematical model for the calculation of input data for this computer program.

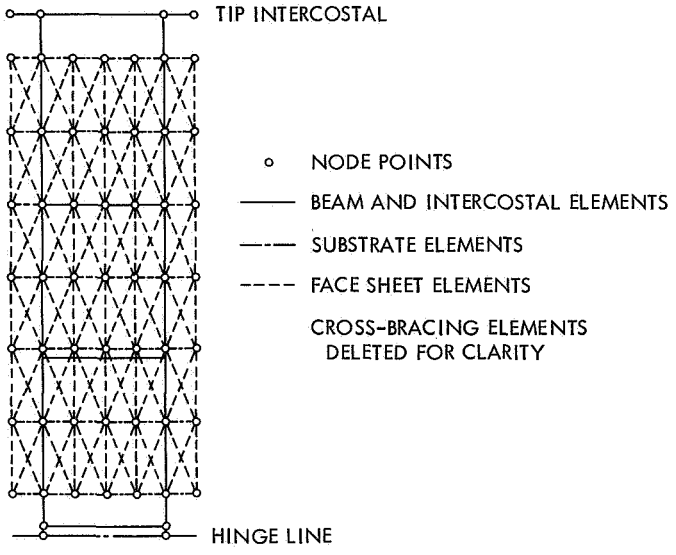

Fig. 9. Finite element model of solar panel

The modal combination program was used to predict the modal characteristics of combined structural subsystems and to predict the damped response to sinusoidal input excitation. Table 4 summarizes the subsystem modes used to predict the forced-vibration response of the complete spacecraft in its launch configuration. By inputting all of these modal characteristics together with assumed damping values, the program provided response plots similar to Fig. 10.

b. Development tests. In the spring of 1968, the development test model (DTM) was subjected to three types of structural tests: static, modal, and forced vibration.

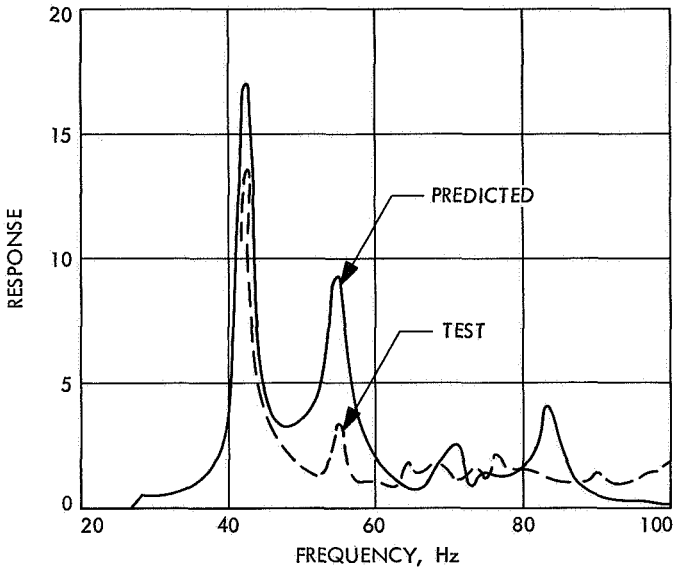

Fig. 10. Frequency response of infrared spectrometer mounted on the planetary scan platform

Table 4. Component modes included in composite analysis

Component	Number of modes				Frequency range, Hz	Number of independent modes
	Rigid body	*Constraint*	*Attachment*	*Normal*		
Bus/adapters	6	0	7	11	45–157	24
Planetary scan platform	6	3	0	6	61–158	6
Propulsion subsystem	6	3	0	6	110–228	6
Solar panels (4), each	6	1	0	10(4)	19–124	40
Solar panel dampers (4 pairs), each	6(4)	0	0	2(4)	0	8
High-gain antenna	6	3	0	6	113–230	6
Low-gain antenna	6	2	0	6	15–177	6
Low-gain dampers (2), each	6(2)	0	0	2	0	2
						98

The primary objectives of these DTM tests were to increase confidence in the analyses and to eliminate structural difficulties prior to the proof-test model forced-vibration tests.

Static tests were conducted on the spacecraft primary structure, consisting of the complete octagon structure attached to the spacecraft and *Centaur* adapters. Separate axial, lateral, and torsional design loads were applied to the top of the octagon. The resulting deflections were correlated with values predicted by analysis. Static tests were also conducted on each DTM solar panel.

Modal surveys were conducted on the primary structure, with and without the planetary scan platform. The first seven modes were surveyed in each case. These data were used to calculate the normalized form of the generalized mass matrix. Because the resulting values for the off-diagonal terms were acceptably small, it was concluded that good modal data had been obtained and that a reasonable mass distribution had been used.

Modal surveys were also conducted on the individual DTM solar panels, the high-gain antenna, and the propulsion subsystem. In general, the test results correlated quite well with the modal characteristics predicted by analysis as indicated in Table 5.

Table 5. Solar panel modal characteristics

Mode shape	Predicted frequency, Hz	Test frequency, Hz
First torsion	18	23
First spar bending	27	29
First in-plane bending	37	34
Second torsion	57	63
Second spar bending	76	78
Third torsion	96	94

Forced-vibration tests were conducted on the launch configuration of the DTM mounted on top of a large electromagnetic shaker (Fig. 11). Shaker excitation was applied along three lateral axes plus the axial axis of the spacecraft. For the majority of test runs, the shaker was controlled, using an instantaneous peak select system, by one of six accelerometers mounted at the separation plane. The specified level thus remained essentially constant during each sinusoidal sweep from 5 to 200 Hz. The specified level was incrementally raised until the design ultimate load level was obtained for that excitation direction. Data from 75 accelerometers and 15 strain gages were recorded. Analysis of these data and the absence of structural failures and clearance problems have engendered high confidence in the ability of the proof-test model to successfully survive a forced-vibration test to design limit loads.

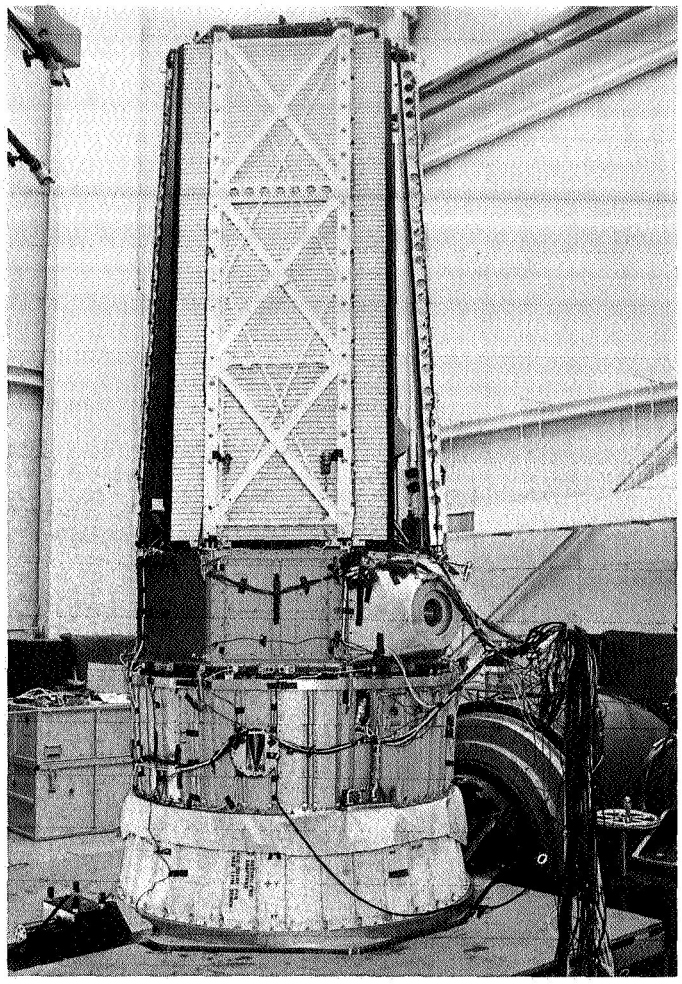

Fig. 11. *Mariner* Mars 1969 development test model

Test data for direct correlation with analytical predictions were provided by low-level runs conducted with the shaker control accelerometer at the base of the *Centaur* adapter in the 5- to 200-Hz excitation frequency range. Slow sweep, sinusoidal shaker input excitation tests were conducted for two lateral spacecraft axes and for the axial axis. Figure 10 presents a typical predicted and measured response for one of the instruments mounted on the planetary scan platform. This comparison indicates that the first two response frequencies were predicted quite well, but that more structural damping is present than was assumed in the analysis, especially for the second and higher frequencies.

c. Spacecraft separation analysis. Separation analyses have been performed to determine the induced spacecraft angular rate and scan platform clearance with respect to the adapter. A worst-case analysis indicates a spacecraft residual rate of 2.2 deg/s. Clearance is primarily a function of lateral translation (motion perpendicular to spacecraft longitudinal axis) and not angular rate. The most critical clearances between the components on the scan platform and the adapter during separation for this worse case are shown below.

Component	Dynamic clearance, in.
Infrared radiometer and umbilical	0.5
Infrared spectrometer and adapter	0.5
Ultraviolet spectrometer and adapter	2.0
Narrow-angle TV and adapter	1.5
Infrared spectrometer cooling unit and adapter	1.0

Statistical error analyses of tip-off rate induced by separation have been made (Fig. 12). Mechanical tolerances are assumed either uniformly distributed (cases 2 and 4) or normally distributed (cases 1 and 3). In two cases (1 and 2), the separation springs are adjusted to minimize tip-off rate due to center of gravity offset.

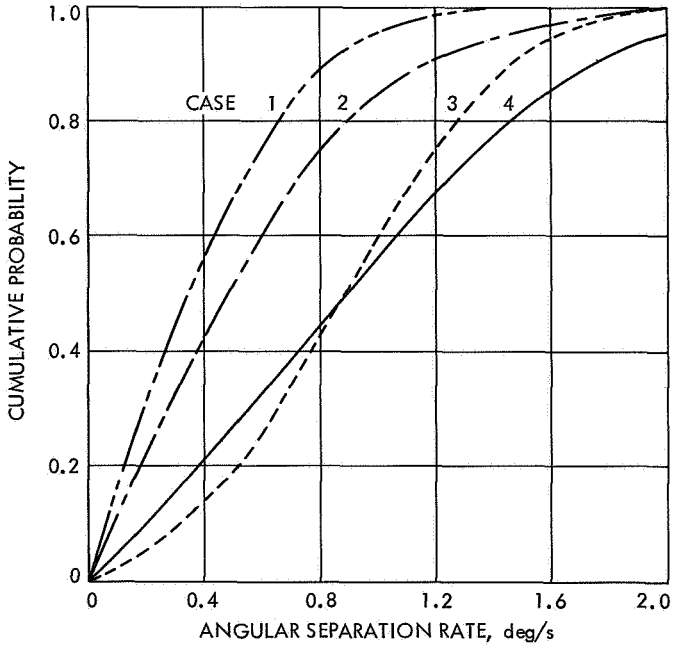

Fig. 12. Spacecraft angular separation rate

References

1. Melosh, R. J., Diether, P. A., and Brennan, M., *Structural Analysis and Matrix Interpretive System (SAMIS) Program Report,* Technical Memorandum 33-307. Jet Propulsion Laboratory, Pasadena, Calif., Sept. 1, 1966.
2. Bamford, R. M., *A Modal Combination Program for Dynamic Analysis of Structures,* Technical Memorandum 33-290. Jet Propulsion Laboratory, Pasadena, Calif., Aug. 15, 1966.

6. Materials Engineering

During the design and fabrication phases of the *Mariner* Mars 1969 spacecraft, several significant materials and process evaluations were undertaken in support of various subsystems. In addition, numerous routine tests were conducted to determine whether specific materials met spacecraft requirements.

a. Adhesive bonding. The Ti-6Al-4V pressure vessels used on the propulsion and attitude-control subsystems are seated on a rubber gasket which is adhesively bonded to the support ring. Difficulty was encountered during the bonding of the rubber gasket to the support ring since the adhesive would not cure completely. Specifically, the materials used were SE-555 Red/SG-50 silicone rubber and RTV-60/Thermolite-12 silicone adhesive. Contact with material suppliers revealed that a plasticizer is added to the SE-555 Red/SG-50 for ease in fabrication. The plasticizer reacts with the catalyst (Thermolite-12) of the adhesive (RTV-60), resulting in an uncured bond.

Other organizations have solved this problem by pretreating the SE-555 Red/SG-50 with Thermolite-12 prior to bonding. Since no details were available, a series of tests was conducted to determine the time necessary for the pretreatment to be effective. Preliminary results indicated that pretreatment followed by a 4-h drying cycle prior to bonding gives a fully cured adhesive when applied, whereas shorter times result in a partially cured product. Additional tests were conducted at the 4-h level, which indicated that the process is repeatable.

The following procedure was effective for complete curing of RTV-60/Thermolite-12 in contact with SE-555 Red/SG-50:

(1) Apply Thermolite-12 directly to the silicone rubber.

(2) Allow to dry 4 h at room temperature.

(3) Wipe away any excess Thermolite-12.

(4) Bond liner to support structure in accordance with JPL specifications.

It is important that the Thermolite-12 in step (1) be applied over the entire rubber surface to be bonded. Since it does not readily "wet" the silicone rubber, considerable brushing is usually necessary. The technique used was to brush on the Thermolite-12, allow to set for 1 min, rebrush the surface, and allow to set again. This was repeated until all silicone rubber had been coated.

b. Magnetic shield welding. Welding difficulties were encountered during fabrication of Conetic AA magnetic shields for the vidicon used in the TV subsystem camera head. The shield consisted of a flat sheet welded normal to a rolled and welded cylinder. The tungsten inert gas (TIG) technique was initially used. Welds made by the TIG technique consistently showed lack of penetration as well as considerable cracking in the heat-affected zone. Since high weld integrity was needed for the shield to withstand launch vibration loads, a joining technique evaluation was initiated.

Two alternate approaches were evaluated, electron beam welding and brazing. The latter showed promise in that the required heat treatment could be applied simultaneously with the brazing cycle. Analysis of the electron-beam-welded joints showed excellent penetration and sound welds. Preliminary analysis of brazed samples also appeared very promising; however, further evaluation of brazing cycle parameters was precluded by schedule constraints. Consequently, the electron beam welding technique followed by an annealing treatment was chosen for fabrication of the shields.

7. Mechanical Devices

a. Solar panel boost dampers/low-gain antenna dampers. The viscous shear dampers for *Mariner* Mars 1969 (SPS 37-44, Vol. VI), as exemplified by the solar panel boost dampers (Fig. 13) and the low-gain antenna dampers (Fig. 14) have successfully completed environmental (type approval and flight approval) and functional testing. Careful attention to piston and cylinder surface finishes, seal material and geometry, and seal gland design resulted in trouble-free performance. There were no cases of fluid leakage. Recent tests have confirmed that the damper characteristics remain unchanged after a period of more than 6 mo of storage and testing.

b. Solar panel cruise dampers. The solar panel cruise dampers for *Mariner* Mars 1969 are the same as those employed on *Mariner* Venus 67 and *Mariner* Mars 1964 (SPS 37-27, Vol. VI). The bracket configuration has been modified to accommodate repositioning of the solar panels. The cruise dampers are designed to provide the following functions:

(1) Absorb the kinetic energy of a deployed solar panel.

(2) Position the deployed solar panel.

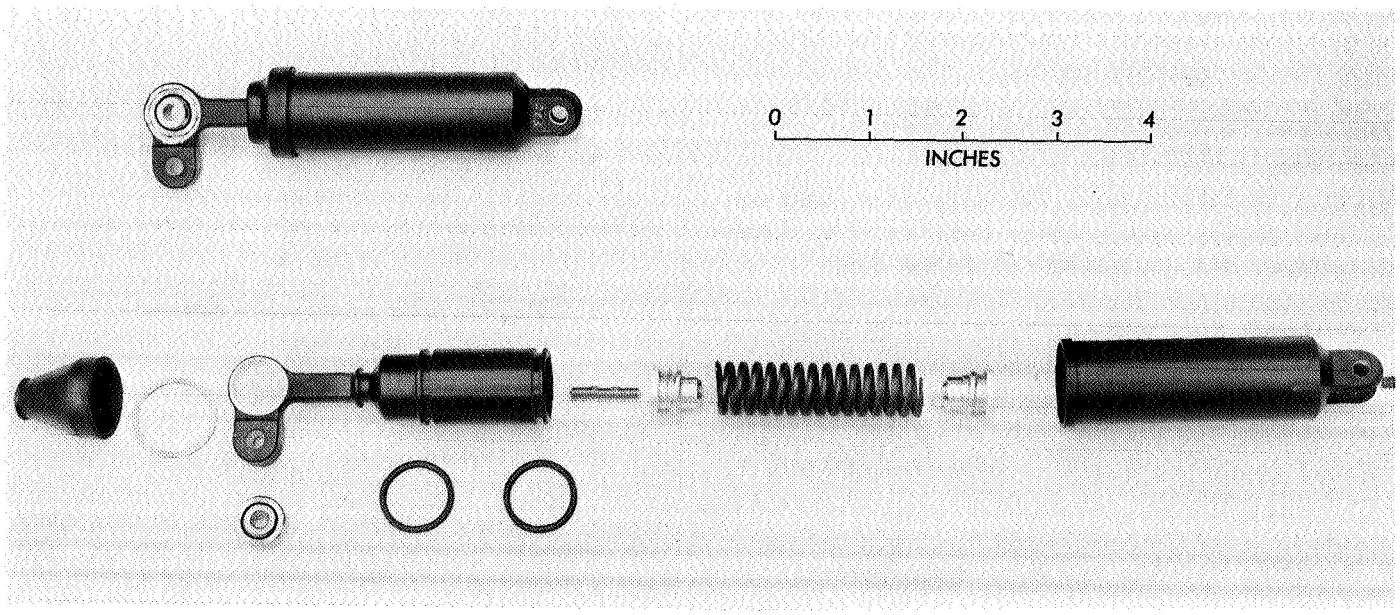

Fig. 13. Solar panel boost damper

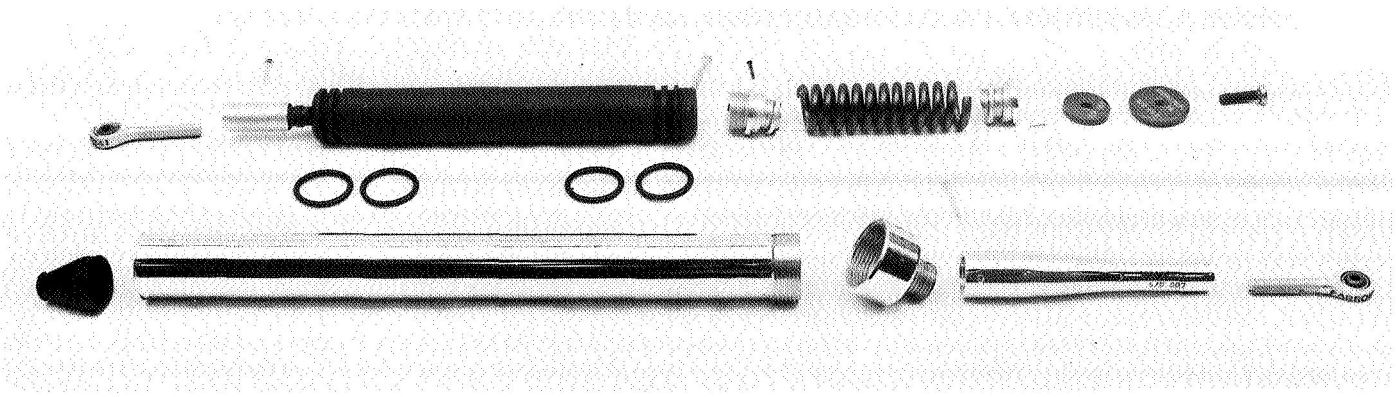

Fig. 14. Upper low-gain antenna damper, exploded view

(3) Damp solar panel oscillations during the midcourse motor firing.

The cruise damper consists of two springs and a dashpot in parallel. The damping force is generated by displacing a piston through a viscous, incompressible fluid. The effective spring constant and damping coefficient of each unit had to be determined to ensure adequate energy absorption capability and proper vibration control of a deployed panel. The spring constant of 530 lb/in. ±10% was determined by force measurements at fixed displacements and zero velocity. Since the expected damped first-mode frequency of a deployed solar panel is 1.5 Hz, the units were actuated at fixed amplitude and at three measured frequencies between 1 and 3 Hz; i.e., at three distinct velocities. With the spring force and imposed velocity known, the peak force on each force-versus-time recording enabled calculation of an effective damping coefficient. The nominal measured damping coefficient was in the range of 65 lb-s/in. This method bypasses the problems of performing phase angle measurements at low frequencies or of evaluating less than ideal decay curves. Damper characteristics can be determined accurately with a minimum of operation time. Figure 15 shows a sample of the test data.

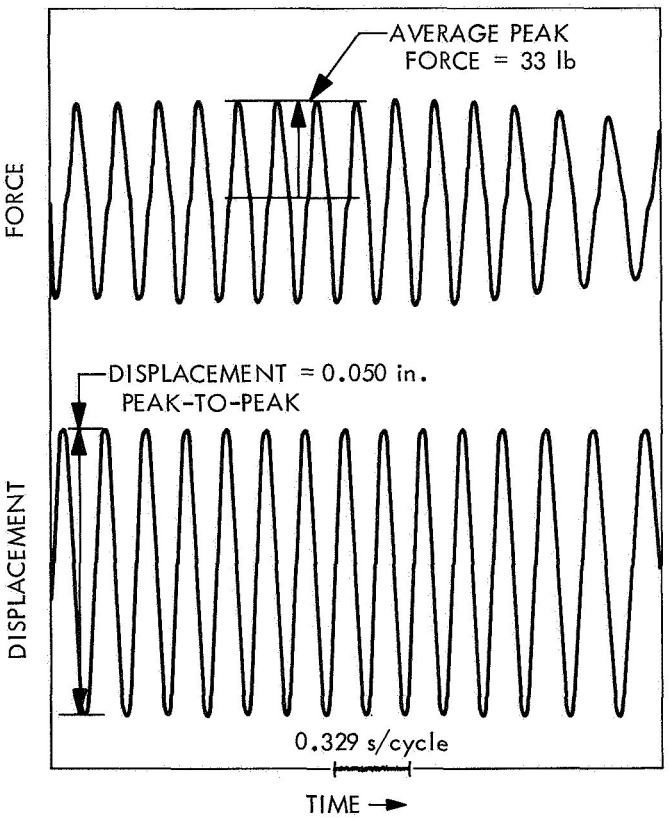

Fig. 15. Solar panel cruise damper test results

All *Mariner* Mars 1969 solar panel cruise dampers have passed environmental and functional requirements. In all cases where fluid leakage was observed, the problem was directly traceable to seals and glands damaged during seal installation. Surface refinishing and seal replacement constituted the corrective actions required.

8. Assembly, Handling and Shipping Equipment

The policy for acquiring assembly, handling, and shipping equipment (AHSE) is to either use *Mariner* Mars 1964 and *Mariner* Venus 67 equipment wherever possible or to modify it when necessary and to improve it when economically feasible (SPS 37-46, Vol. VI). Principal new equipment includes guides on spacecraft mounts, spacecraft protective cans, a protective can for the scan platform, a science stimuli platform, a universal ring adapter, and a time-saving suspension system for use in the 10-ft space simulator.

The spacecraft protective container is bigger in diameter and length due to the larger size of the *Mariner* Mars 1969. To accommodate the low ceiling areas about the Laboratory, the new container was split down the middle so it would not have to be hoisted up, over, and down onto the spacecraft. To prevent accidental damage during installation, the two halves are hinged like a clam shell from the universal ring adapter and are light enough to be easily handled by two men, yet rigid enough to be hinged at any angle from horizontal to vertical. Figure 16 shows one half of a container being hinged over a spacecraft mounted on a positioner tilted horizontally. Due to the unsatisfactory performance of electrically conducting plastic, as well as the danger to personnel to install it, a plastic bag is not used on the full-sized container (the metal container is self-sealing). A plastic bag is used, however, over a tubular frame when shipped in a van.

The larger diameter container required, in turn, an adapter that is semi-permanently bolted to the universal ring (Fig. 16). This adapter contains (1) the hoist points to lift the spacecraft, (2) access holes through which electric cables can be inserted for limited testing of the spacecraft while it is under the container, and (3) breather valves that limit the pressure inside the container.

A wider spreader bar assembly and longer hoist cables were procured; the design was sufficiently similar to the *Mariner* Mars 1964 hoist assemblies to allow some parts to be cannibalized. The longer solar panels required new

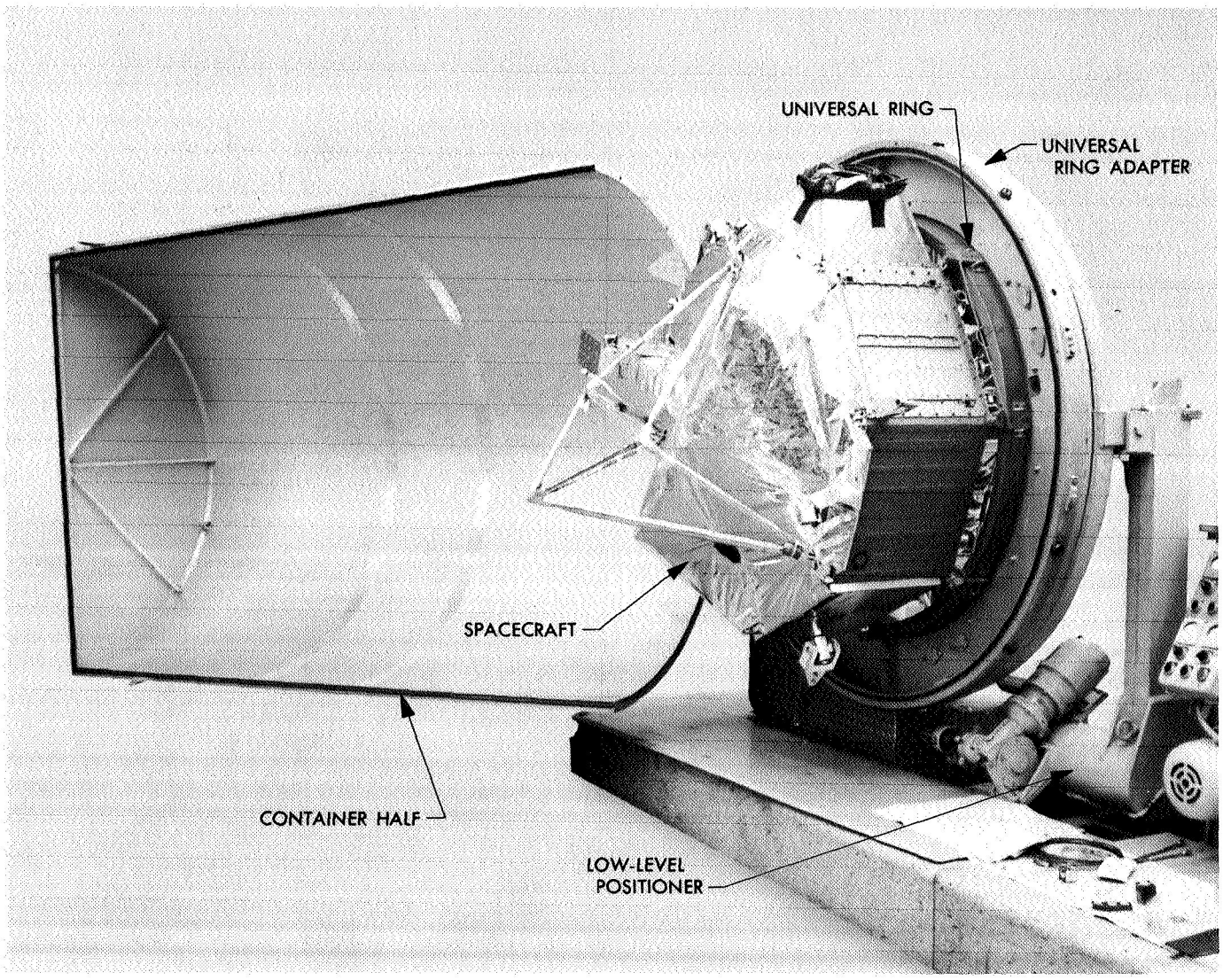

Fig. 16. One-half of spacecraft container hinge-mounted on universal ring adapter

solar panel handling frames as well as new bags to cover them. Minor modifications were also made to the solar panel transport trailer cradles. The longer low-gain antenna required an extension to the previous *Mariner* shipping container.

To obviate possible damage to the scan platform, guides were provided to restrict motion of the spacecraft during the last 6–8 in. of travel onto the universal ring as well as the flight adapter. To protect the scan platform when shipped on the trailer or when attached to the dolly, a protective can was designed that covers the platform; in addition, it supports the entire spacecraft together with its protective containers and universal ring.

The two TV cameras and the infrared spectrometer on the scan platform are checked in the system test operation by attaching stimuli for all three instruments to one science stimuli platform. The stimuli platform (Fig. 17) is temporarily bolted to the universal ring. Once each stimulus is properly aligned and secured to the stimuli platform, all three may be removed as a unit from the universal ring, stored, and then reinstalled with sufficient repeatability to obviate the time-consuming alignment procedure experienced in the previous programs.

The spacecraft suspension system in the 10-ft space simulator was designed to save installation time by mounting it on the end bell where spacecraft installation

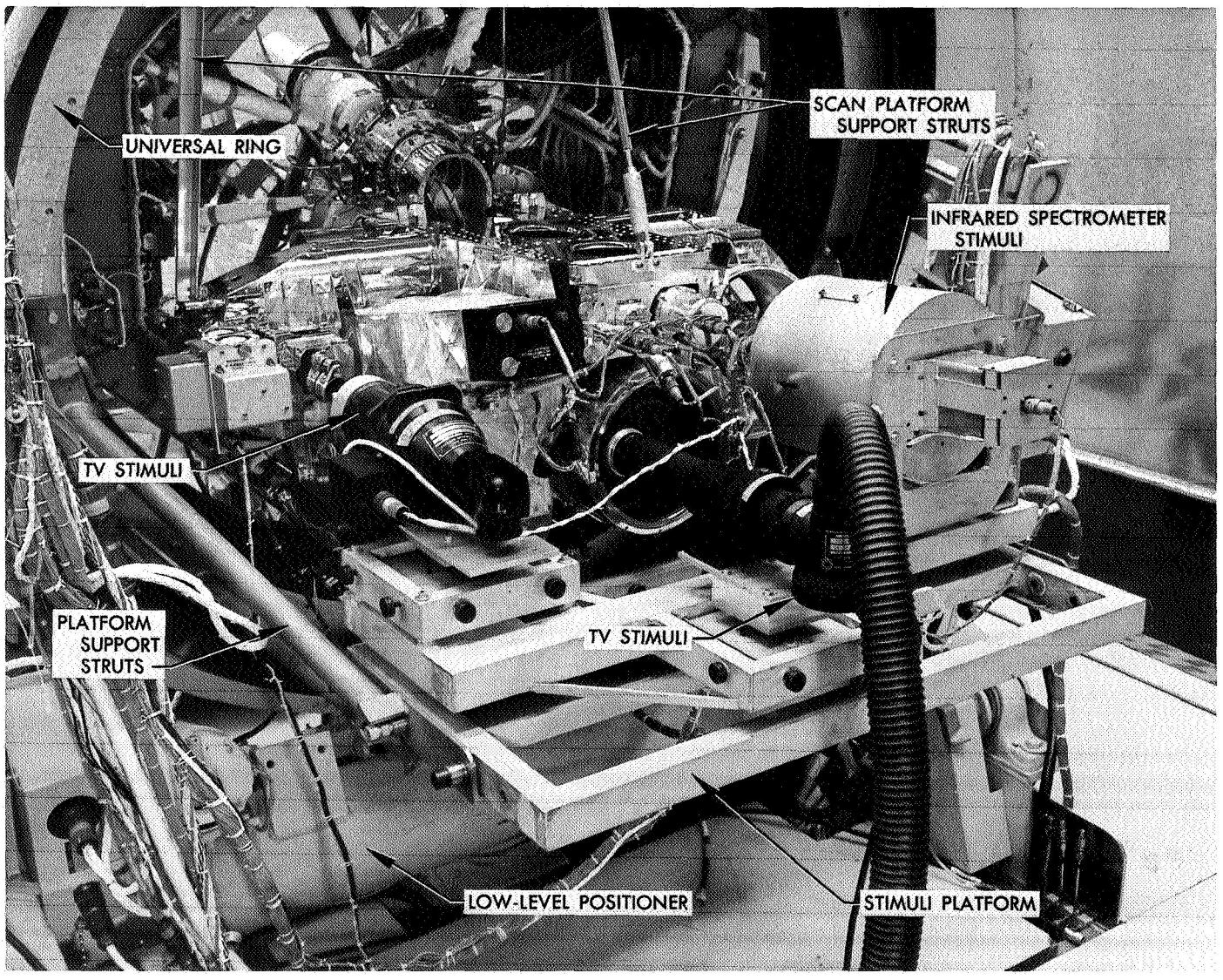

Fig. 17. Science stimuli platform in place for systems test

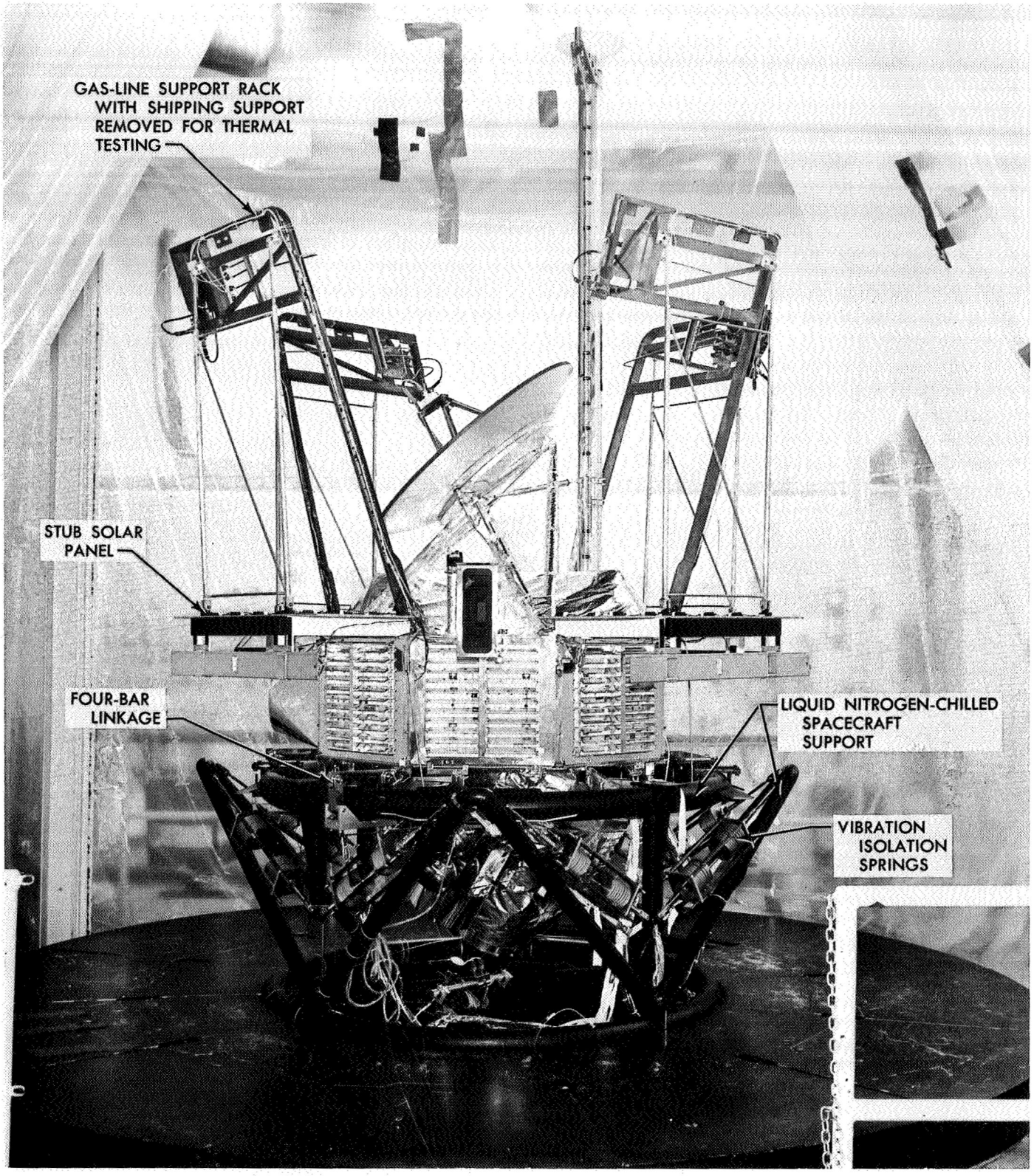

Fig. 18. Spacecraft on end bell of 10-ft space simulator

work can be easily performed in the open instead of the tight quarters inside the simulator (Fig. 18). The spacecraft is coupled to the system by three of its feet being attached to a four-bar linkage (Fig. 18) that allows for contraction and expansion differences. The linkage is polished stainless steel that is maintained at the same temperature level as the spacecraft feet by means of heaters. Vibrations over 2 cps inherent to this simulator are isolated by soft compression springs (Fig. 18).

When the stub solar panels (for thermal test) are mounted on the spacecraft and the attitude-control gas-line support racks are remounted, a transfer fixture is used to provide structural support for the gas line, thus assuring its safety. When the solar panels are not mounted on the spacecraft, the attitude-control gas system is supported on the frames that were originally used to ship the gas system from the fabricator. These shipping frames are also used in the space simulator to support the gas line. The removal of the heavy weldment that makes up the stiffening members leaves only a light shell which is acceptable for thermal testing in vacuum (Fig. 18).

The spacecraft is stored on a universal ring mounted either on a service dolly, a transport trailer, a low-level positioner (SPS 37-46, Vol. VI), or on the new extended leg assembly where the scan platform is easily accessible.

The revised mounting of the propulsion subsystem required a new weight and center of gravity fixture that attaches to bay II by the upper and lower octagon, but is located precisely from, but without placing any load upon, the propulsion system attach points (Fig. 19). The fixture is a whippletree-type that allows the bus to be supported on four points without danger of loading the bus in torsion if the four points are all not in the same plane.

As a general rule, the surface treatment for all AHSE was only to anodize to maintain a clean surface; no paint was applied where it could chip and contaminate.

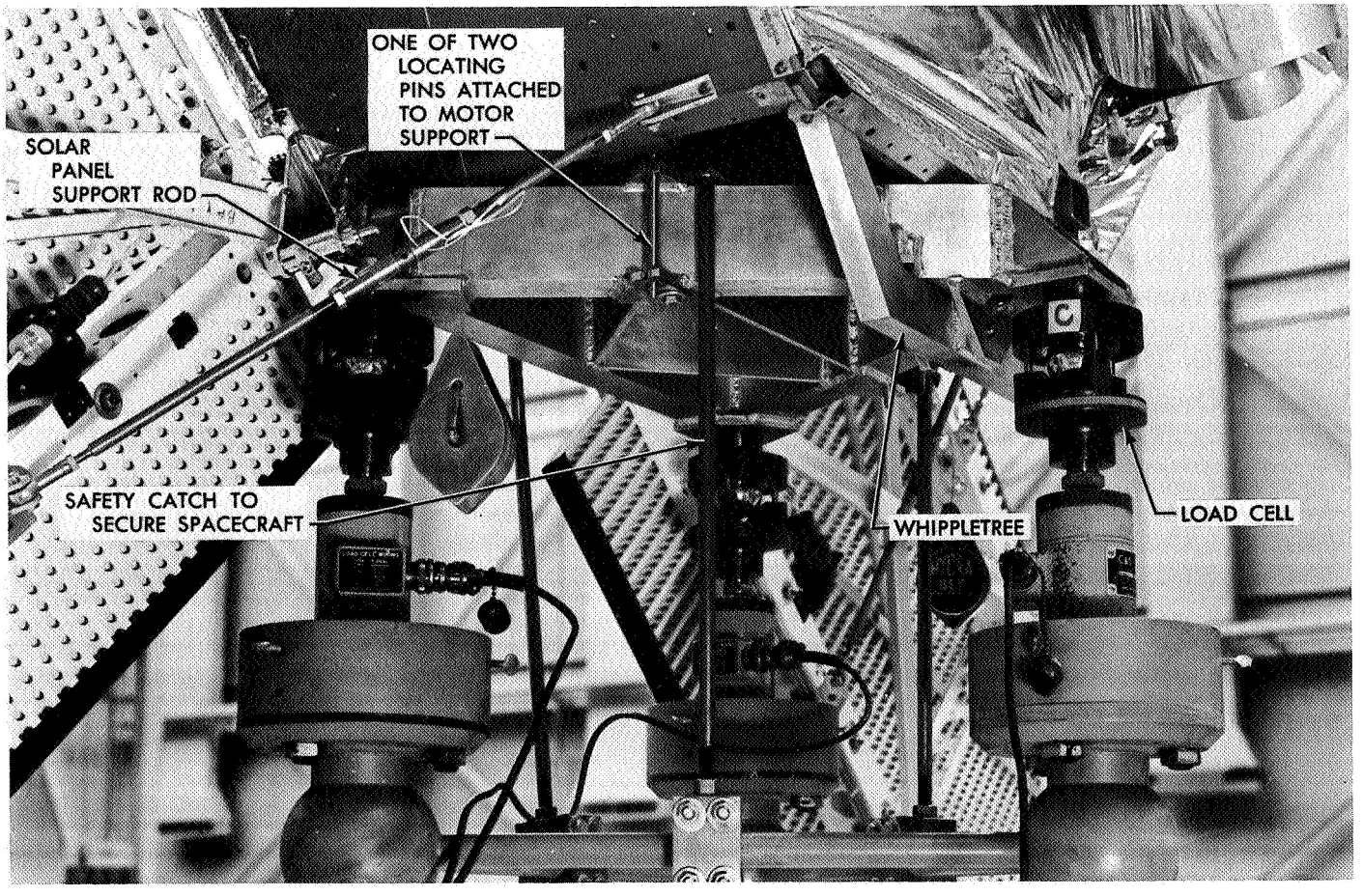

Fig. 19. Fixture to find center of gravity about centerline of the midcourse motor

E. Guidance and Control

1. Power Subsystem

a. Flight batteries.

Design modification. During the *Mariner* Venus 67 program, the battery design was found to be marginal at type-approval vibration levels. This was manifested by fractures occurring in plate lead wires during vibration. Although the magnitude of these defects was not sufficient to totally impair battery performance, there was some functional degradation.

After an analysis of the vibration characteristics of the *Mariner* battery was completed, modifications were made to the internal cell design and chassis to ensure an adequate margin beyond type-approval requirements. These changes were made primarily to limit plate-pack displacement and chassis flexing during vibration.

Two designs were tested as part of the *Mariner* Mars 1969 type-approval test program, one having restrained plates and the other having unrestrained plates, both in chassis of new design.

Vibration testing. Batteries 101, 102, 103, and 104 were vibration-tested at the JPL Environmental Test Laboratory in accordance with project requirements for type-approval testing. The vibration levels and duration in each axis were as noted in Table 6.

Batteries 101 and 102, of the primary design with restrained plate packs, were vibrated through all axes. No anomalies or defects were observed during or after the vibration testing. This design met all vibration requirements for type-approval testing.

Batteries 103 and 104, of the alternate and secondary design with unrestrained plate packs, were then vibrated at the type-approval levels. Battery 104 completed vibration (both sinusoidal and random noise) in the x and y axes, but failed during random noise in the z axis. Battery 103 also failed during z-axis random noise, the first vibration to which it was exposed. Instrumentation on the batteries clearly indicated that the mode of failure was shorting of positive plates against negative lead wires and breaking of plate lead wires, caused by large displacements of individual plates.

Table 6. *Mariner* Mars 1969 type-approval vibration test levels

Sinusoidal frequency range, Hz	Vibration level, *g*	Duration (each axis)
5–30	0.75	1.0 min/octave, 5 to 2000 to 5 Hz
30–250	7.5	
250–600	4.5	
600–2000	13.5	
Noise	18.1	1 min

Test conclusions. The unrestrained plate-pack design does not meet the type-approval test requirements. The frictional forces (plate-pack pressure) holding the plates are far exceeded by those vibration-induced forces on the plates causing a high magnitude of plate displacement. The flight battery design with the restrained plate pack meets all requirements for *Mariner* Mars 1969 type-approval testing.

b. Boost converter relay. The power subsystem was modified to include positive identification of the state of the boost converter relay during the mission. This relay toggles the boost converter relay to "inhibit" and "enable" positions, and its state was to have been registered and ascertained by log book entry. During launch, the relay is in the enable position where it remains for a nominal mission. There was concern, however, that should the relay change state by some spurious means during the mission, the log book entry describing its state would be false.

The design modification to monitor the state of the relay during the mission utilizes the current transducer output of the $-y$ solar panel. The transducer output passes through the relay before the flight telemetry subsystem such that the solar panel current output is telemetered when the relay is enabled.

The enabled relay permits the booster converter to provide power pulses to the dc power bus in the event a power transient causes the battery to share the spacecraft power load with the array. The pulses are designed to shift the operating point to a more desirable operative mode in which the battery does not unnecessarily contribute its stored energy to the spacecraft. The relay operation is automatically inhibited when the spacecraft solar panels are not facing directly toward the sun, as during maneuvers.

2. Destructive Life Testing of Convoluted Flexible Tubing

a. Introduction. Convoluted flexible tubing is used in the *Mariner* Mars 1969 attitude-control gas system in eight

separate locations. All are within the low-pressure distribution portion of the gas system, which carries the nitrogen gas to the attitude-control jet valves located at the tip of each solar panel. The four flex tubes located at the solar panel hinge points are subjected to the greatest amount of flexing during fabrication, assembly, and testing of the spacecraft prior to flight.

To establish a realistic number of flex cycles permissible prior to launch, a test program was initiated to determine the maximum number of cycles that representative samples of flexible tubing could withstand before failure.

b. Test configuration. A test fixture (Fig. 20) was fabricated to closely simulate the configuration of the solar panel hinge area. The test fixture contained a driving motor, which cycled the test piece at about 7 cycles/min, and an electric counter to record total cycles. A pressure gage (0–30 psi) and a manual shutoff valve permitted pressurization of the test sample, thus providing a convenient method of verifying failure by monitoring pressure. Since the total volume of the unit under test was approximately 1.2 in.^{3}, even the slightest leak would result in an immediately readable pressure drop on the gage.

Normal operating pressure of the low-pressure portion of the *Mariner* Mars 1969 gas system is 15.0 $\pm$1.2 psig. The tests described in this report were made at a pressure of 20.0 psig to increase severity of the test.

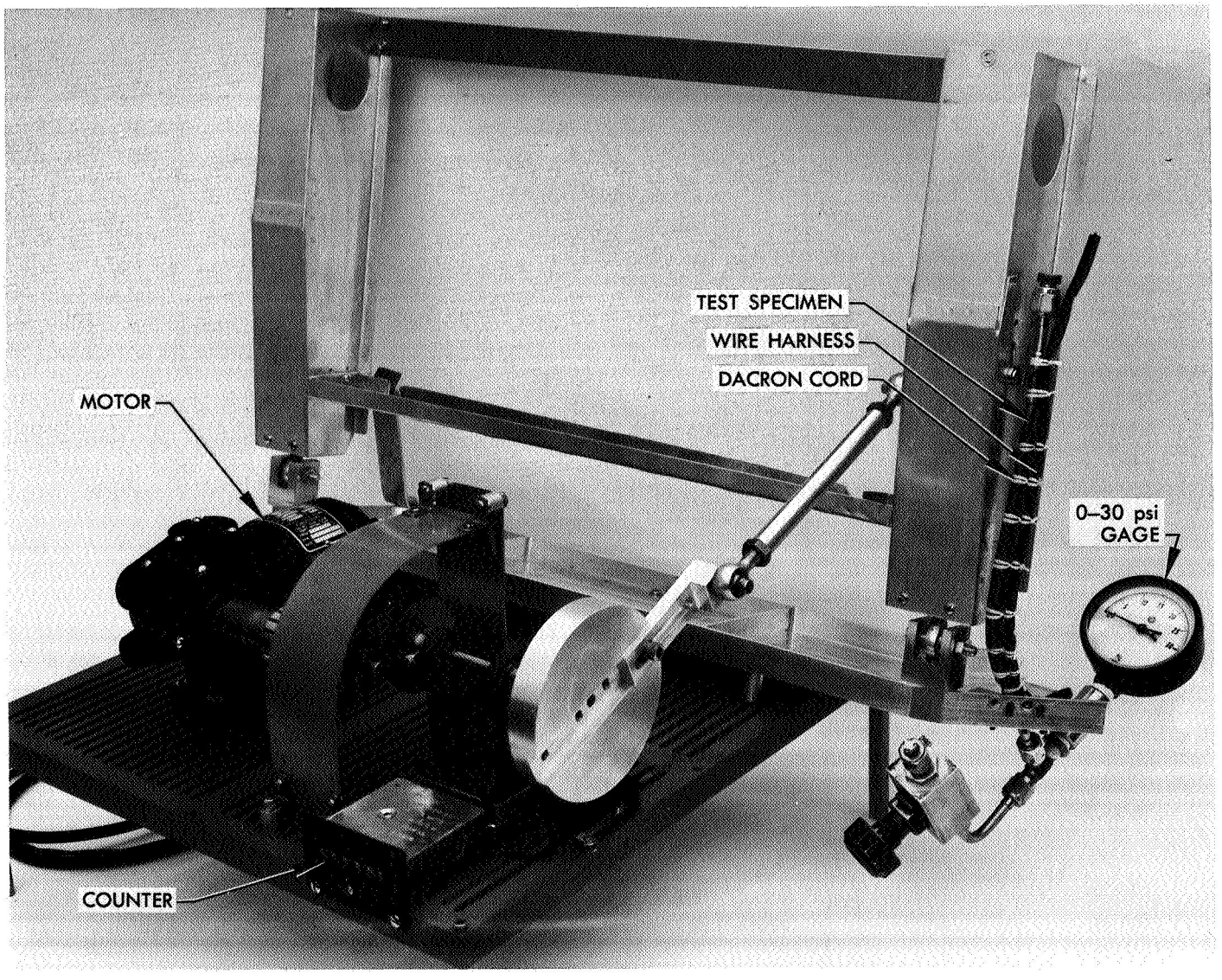

Fig. 20. Convoluted flexible tubing test configuration

c. Test samples. Two samples of convoluted flexible tubing[1] were used in this test. The samples were hydrogen-annealed to the "dead soft" condition after forming, and were selected at random from stock intended for use in the *Mariner* Mars 1969 gas systems. *Mariner* Mars 1964, the forerunner of *Mariner* Venus 67 and *Mariner* Mars 1969, was originally designed to use flexible tubing that had not been annealed after forming. Failures at low cycle range on *Mariner* Mars 1964 (200–500) showed that this was unacceptable, and fully annealed tubing was substituted.

End-fittings identical to those used on flight configuration were welded to the tube samples. To fabricate the end-fittings, 321 stainless steel was used. This is also the material from which the tubing was formed. AN-type B nuts and sleeves were then attached to both end-fittings, and zero leakage was achieved by using copper cone seals in all B-nut connections. Proof pressure test was performed at 40 psig, and no leakage at any point was allowed.

A short section of wire harness (Fig. 20) was secured to the convoluted tubing with Dacron lacing cord. This very closely approximates the flight configuration of the *Mariner* Mars 1969 attitude-control gas system.

Final leak check was performed by pressurizing the test sample to 20 psig, and allowing it to remain overnight in a static condition. No drop in pressure was permitted and none was experienced at this stage of the test.

d. Test results. Test samples were cycled individually beginning with serial number 30. After nearly 3 days of cycling, a slight pressure drop was noted at 7902 cycles. "Snoop" leak-test solution was applied to the tubing sample and cycling continued until a definite indication of leakage was detected in the tenth convolution above the lower end of the tube.

The second sample (serial number 31) was set up in precisely the same manner and cycled at the same rate. After 14,802 cycles, the line pressure dropped to 19.8 psig. The snoop solution again was used and leakage was found in the twelfth convolution from the lower end of the tube.

The tubing used in this application is annealed to a very soft condition and is very susceptible to damage from mishandling or other external causes. Future tests could be useful in arriving at a compromise between long flex life and physical durability, or in finding other materials that exhibit long flex life and greater resistance to damage.

e. Conclusions. Based on estimates and data gained from *Mariners IV* and *V*, the solar panel hinge should not be subjected to more than 500 cycles during fabrication, assembly, and testing. Assuming that the convoluted flexible tubing sustains no damage from external sources, its life expectancy far exceeds the requirements of this mission. However, no specific safety factor can be assumed on the basis of results from only two test samples.

[1]Fabricated by Anaconda Metal Hose Div., Anaconda American Brass Co., Waterbury, Conn.

F. Space Sciences

1. Infrared Radiometer

Subsystem-level type-approval vibration testing of the proof-test model (PTM) infrared radiometer was not completed prior to delivery to the Spacecraft Assembly Facility (SAF) due to the motor shaft redesign schedule (SPS 37-51, Vol. I). The radiometer containing the redesigned shaft was vibrated on the PTM spacecraft at type-approval levels in early June 1968. A partial verification of the data indicated that the PTM apparently survived this launch environment. However, complete verification cannot be accomplished until all the data have been analyzed. The performance of the radiometer during solar simulator testing of the spacecraft was satisfactory.

Flight acceptance tests for the first and second flight radiometers were completed. The third flight radiometer is undergoing calibration test.

The electromechanical portion of the radiometer, namely the motor/scan detent (positioning) assembly, was subjected to a high-vacuum test program to determine its susceptibility to cold welding. The scan detent assembly was bolted to a mounting plate which was suspended from the chamber feed-through plate by heater cables (Fig. 21). Two copper–constantan thermocouples were attached to the motor and two on the mounting plate. A glass-coated heater wire was wrapped around the motor for temperature control but was not required during test. Instrumentation included an electromagnetic pickup device mounted close to the inertial weight of the motor. This weight has four iron screws embedded in the circumference. When the motor was stepped, the pickup would give a pulsed output representing the time interval from one position to the next. A

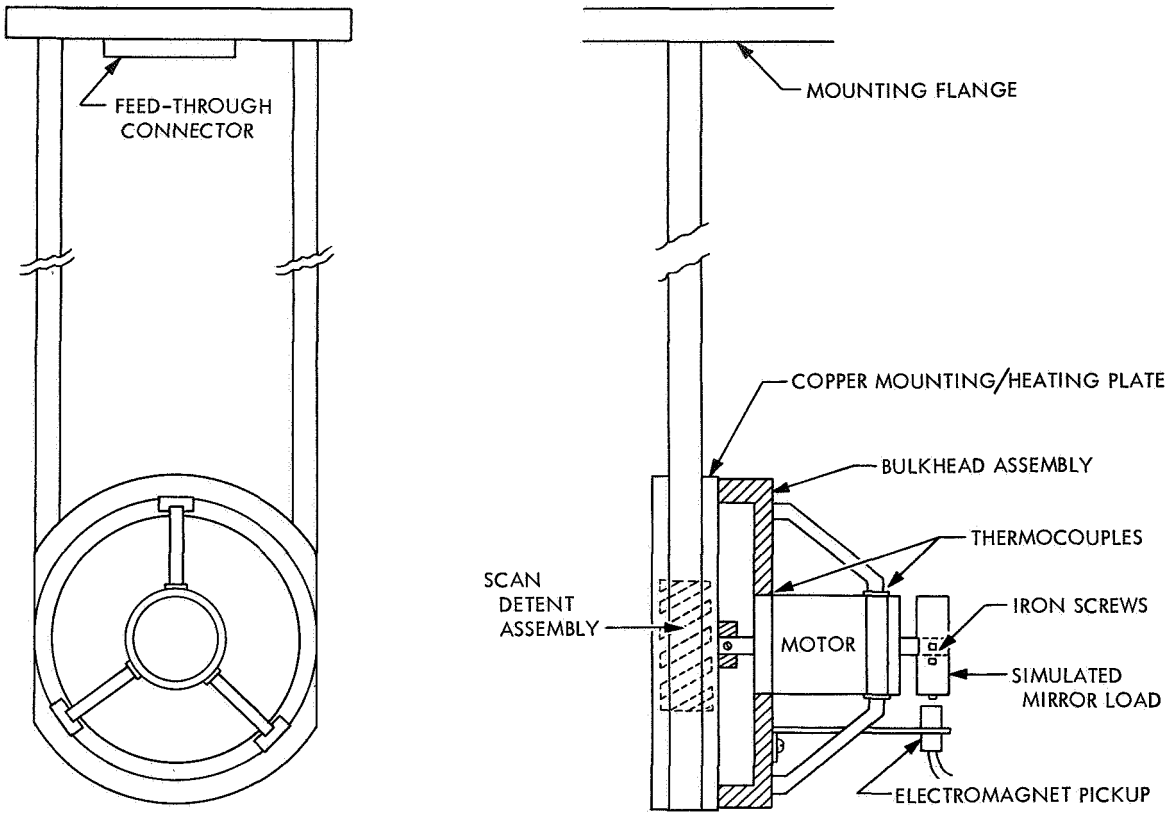

Fig. 21. Motor/scan detent assembly of the infrared radiometer

change in time interval would denote friction caused by cold welding in the assembly.

The testing program consisted of a non-operating period of 168 h, simulating the cruise mode, and an operating period of 336 h. Initially, the chamber pressure was reduced, with the motor not operating, to approximately 2×10^{-10} torr and 55°C. Following the 168-h non-operating period, the chamber temperature was reduced to 0°C and, after stabilization, the motor turned on. The motor was then operated for a period of 336 h at approximately 10^{-10} torr, and normal stepping rate of 4 steps/min. No degradation of scan detent assembly operation was noted during any portion of the testing.

2. Alignment Verification Instrumentation

a. Introduction. A method to measure the relative angular alignment of the planetary instruments mounted on the scan platform of the *Mariner* Mars 1969 spacecraft has been developed and reported previously (SPS 37-49, Vol. I, pp. 25–26). The purpose of these measurements is to detect errors in the instrument pointing directions. Each instrument is aligned to its base reference plane before being mounted on the platform. However, subsequent misalignment of the internal optical axis or the instrument/scan platform interfaces can result from moving the instruments, spacecraft testing activities, shipping the spacecraft to the Air Force Eastern Test Range, etc. This method permits a last-minute measurement of the instrument alignment at the JPL Spacecraft Assembly Facility and the Air Force Eastern Test Range without disturbing the instruments.

b. Hardware description and function. Subsequent to the last report, the hardware required to take the measurements was acquired and assembled (Fig. 22). The configuration consists of three main parts: (1) a collimator mounted on a transit base and supported on a tooling bar with its stand, (2) an angle mirror independently supported on an adjustable instrument stand, and (3) a reference optical flat.

The collimator is an off-axis reflecting type designed to prevent central obscuration and to tolerate the wide spectral range of the science instruments. It is fitted with a microscope and retractable beam splitter to allow autocollimation in the visible range. Light sources can

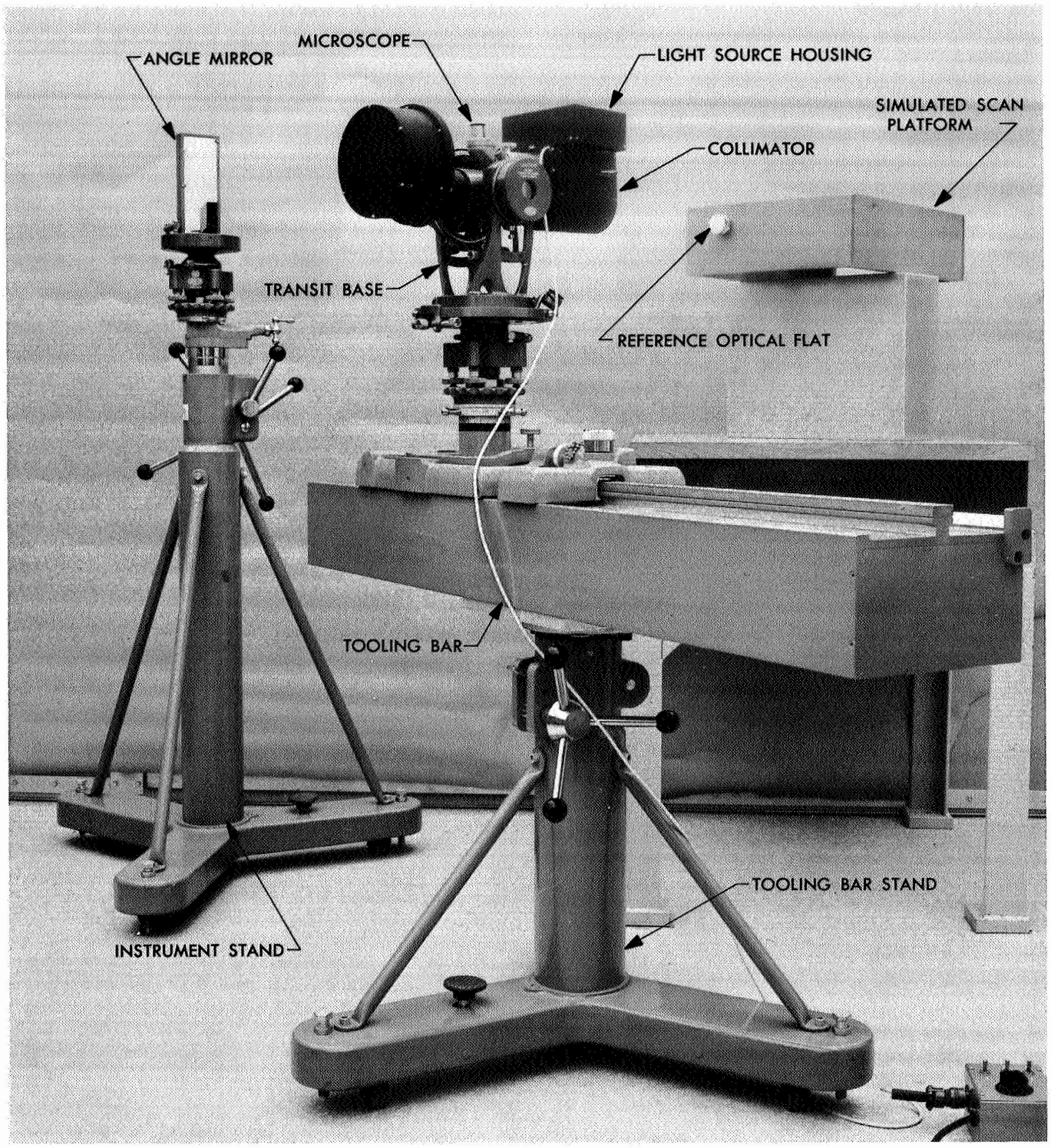

Fig. 22. Instrument alignment verification configuration

be selected in the ultraviolet, infrared, and visible ranges; a slide positioner is used to select different reticle patterns. The collimator stimulates the instruments and appears as a distant source. A definite pointing direction is associated with the collimator (negative to the direction an instrument would look to see the distant source). The weight and size (aperture) of the collimator were limited by the size of available transit bases.

The transit base is a one-piece truss type with a special ball-bearing-mounted spindle to accommodate the collimator. This permits the pointing direction of the collimator to be controlled and measured with respect to the reference angle mirror. Angular readings of the collimator positions are obtained from circles with 20-s vernier readouts.

The angle mirror is a first surface optical flat accurate to one-fourth wavelength and large enough to permit all the instruments to be referred to it from their positions on the scan platform. It is mounted on a base with leveling and tangent screws and is supported on an adjustable instrument stand that can be adjusted to the proper height relative to the scan platform. During measurements, the angle mirror is fixed in position and acts as an alignment reference, or tie point, to which the angular measurements on the instruments and the reference optical flat on the scan platform can be referred. This permits angular measurements to be made independently of the horizontal and vertical translations of the collimator between the instruments.

The reference optical flat is a steel spool with faces 1.5 in. in diameter. One face is bolted to the front of the scan platform. The other is a polished, optically flat reflecting surface that can be defined in terms of the xyz coordinates of the scan platform. The reference optical flat is used to establish a reference plane relative to the pointing direction of the scan platform. The final pointing directions of the instruments relative to the scan platform can be calculated by normalizing all angular measurements to the optical flat reference plane.

c. Alignment procedures. The alignment system was used to verify the expected alignment procedures as spacecraft operations schedule permitted. The infrared radiometer, infrared spectrometer, and wide-angle TV procedures were attempted. Some simplifying modifications were implemented and no insurmountable problems were encountered. The response of the instruments was as predicted with the exception of the infrared spectrometer which showed the pointing direction of the instrument to be somewhat dependent on where the collimated beam enters the telescope. The reason for this phenomenon could not be determined in the limited time available for testing and is being investigated further. The resolution of the measurements was as predicted. The remaining procedures will be tested as the instruments are made available.

3. Infrared Spectrometer

The proof-test model (PTM) infrared spectrometer (SPS 37-51, Vol. I) was used to support PTM spacecraft testing, including space simulation, vibration, acoustic, and pyro shock testing. During verification after vibration, it was determined that the channel 1 (HgGe) detector was not operating properly. An investigation of this anomaly is in progress.

The first flight unit has undergone flight acceptance thermal vacuum and vibration tests. During the post-vibration calibration verification test, excessive noise appeared in channel 2 and the cause is being investigated. The second flight unit is being assembled, and the third flight unit is in the final stages of fabrication.

A life test of the infrared spectrometer gear train has been performed in the JPL molecular-sink facility. This test consisted of a non-operating "soak" to simulate spacecraft cruise conditions (50 h at 10^{-11} torr and 40°C) and an extended operating period at −40°C. The test proceeded as planned through the simulated cruise phase. The motor was then operated for 122 h at −40°C when it stopped. Several attempts were made to restart the motor with no success. The chamber was then backfilled to 1 atm with dry nitrogen and another attempt to start the motor was also unsuccessful. The assembly was then removed from the chamber for analysis.

Recent tests revealed an embrittlement problem associated with the storage of gaseous hydrogen in an Inconel 718 vessel. An extensive test program was started to determine a safe operating pressure for the present vessel. To date the tests have shown a lowering of the threshold stress intensity. However, at the operating pressures of the bottles, the tests also indicated that the worst-case failure would be a leak in the vessel rather than a bursting of the vessel. The exact degree of threshold lowering, and whether or not this will affect the sustained pressure holding capability, is still to be determined.

II. Advanced Planetary Missions Technology

ADVANCED STUDIES

A. Introduction

An Advanced Planetary Missions Technology Program has been established under the cognizance of the JPL Assistant Laboratory Director for Flight Projects. Mission and system studies and scientific and engineering work are being performed to support planning and advance the state-of-the-art applicable to future planetary missions. The current technological activities are reported in this chapter of the SPS, Vol. I.

B. Project Engineering

1. Biological Monitoring of the Capsule Mechanical Training Model During SADL Assembly

a. Introduction. A primary requisite to establish low microbial burden assembly procedures of a space capsule is a rigorous monitoring program capable of providing step-by-step visibility of the accumulation of microbiological burden on the hardware during assembly.[1]

[1]Kales, P. A., et al., *CMTM Biological Monitoring Plan,* 1967; Brewer, W. A., et al., *Assembly of CMTM for Purposes of Determining Areas of Contact During the Assembly Process,* 1967; Botan, E. A., and Lumney, E. J., *Development of Procedures for Estimating the CMTM Microbial Burden, Part IV,* 1967 (JPL internal documents).

The Sterilization Assembly Development Laboratory (SADL) is a "pilot plant" to develop methods for controlled assembly and terminal sterilization of space hardware. A capsule mechanical training model (CMTM), a 14-ft-diam mechanical mockup of the major subassemblies expected to comprise a capsule (Fig. 1), is being assembled and disassembled in the SADL (SPS 37-50, Vol. III, pp. 71–74, and Ref. 1) under varying environmental and test constraints to generate data relative to:

(1) The biological burden existing on "as received" CMTM hardware.

(2) The burden buildup at various stages of assembly.

(3) The burden indigenous to occluded, mated, and inaccessible areas in the assembly.

(4) The effect of environment on accumulated burden.

This data will provide a basis for the selection of optimum assembly procedures and the design and operation of support facilities (Ref. 2).

b. Sampling sites. The biological burden is estimated by attaching sterile 1- × 2-in. stainless-steel strips (coupons) to selected sampling sites on the CMTM hardware (Fig. 1) and removing them at specified intervals. The procedures conformed with those set forth in Ref. 3. The monitoring plan[2] determines where and when to sample and the area ratio that should be sampled.

One of the major factors in the biological monitoring of spacecraft assembly is the distribution of burden relative to capsule configuration. To determine the area to be sampled, the surface areas of all CMTM subassemblies were divided into expected burden-level zones:

(1) Handled areas—areas contacted by assemblers.

(2) Direct fallout areas—areas that are horizontal upward-facing flat surfaces, ridges, flanges, etc.

(3) Indirect fallout areas—areas that are vertical or slanted surfaces.

(4) Extremely low burden areas—areas that are downward-facing or inside surfaces.

All zone types, except type 1, were established by examining the physical configuration of the hardware. The type 1 zone was identified by having the CMTM assemblers wear gloves dusted with fluorescent tracer powder. All subassemblies of the CMTM were periodically scanned with an ultraviolet lamp (during assembly) and all visible areas of fluorescence were mapped and photographed. Prior to each assembly operation, the hands and wrists of the assemblers were scanned under an ultraviolet lamp to assure particle density to provide an adequate fluorescent signature. The assembly procedures used in this test were strictly followed in subsequent tests, thus establishing, through repetition, a true index of contamination resulting from personnel contacts.

[2]The biological monitoring plan is based on work performed by the AVCO Corp., Lowell, Mass., JPL Contract 951624.

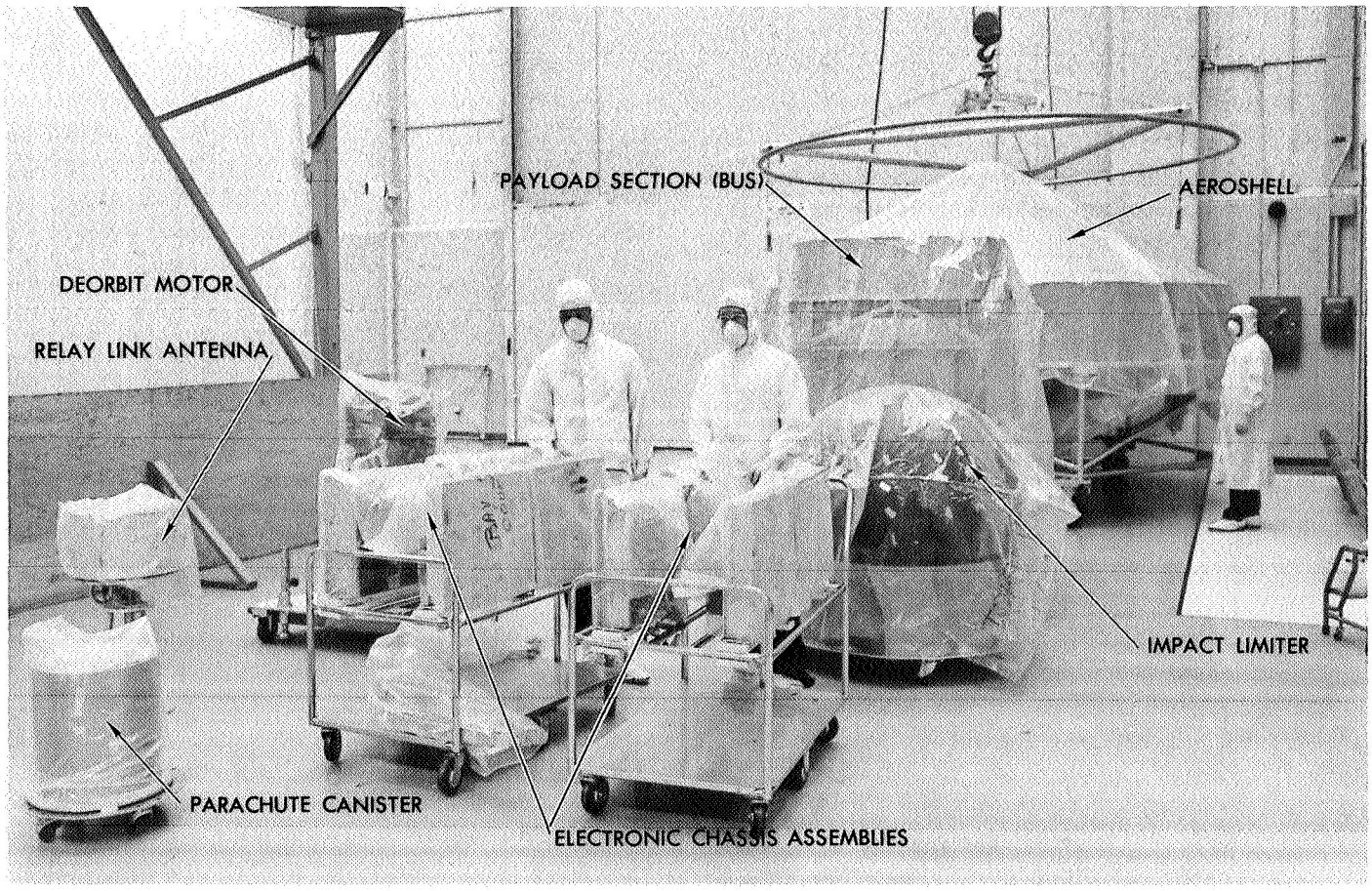

Fig. 1. Capsule mechanical training model subassemblies

The monitoring plan treats coupon allotment as though burden can exist only at discrete levels. The classes of expected contamination levels were defined by the above zoning procedure, where zone 1 would have the heaviest burden level and zone 4 the lightest.

c. Coupon allotment. The following conditions and definitions were established as a statistical basis for the coupon allocation plan:

(1) The open CMTM surface areas at a given assembly stage are defined to be identifiable areas that are exposed and accessible within the normally defined operations of the assembly process.

(2) The various segments of the open CMTM surface areas at a given assembly stage are categorized into one of the four expected burden-level zones.

(3) Independent burden estimates are to be derived relative to the total open assembled CMTM surface areas at 16 defined assembly stages.

(4) The total number of coupons to be assayed in a given CMTM assembly in the SADL facility is limited to 600.

(5) A minimum of three completed CMTM assembly operations is to be performed for each test configuration.

The objective of the coupon allocation plan is to apportion the 600 coupons in such a manner that the precision of estimates would be maximized. The precision of burden estimates is greatly influenced by the sample size or number of coupons associated with a given estimate and the inherent variability of the burden distribution relative to the open CMTM surface areas sampled (the greater the variability, the less precise the estimate).

A stratified, randomization sampling procedure was selected for the coupon allocation plan. This procedure consisted of subdividing (zoning) the respective surface area population into subpopulations and selecting a given number of coupons (subsamples) from the respective subpopulations. The formula used to allot coupons to the identified zones on the subassemblies was

$$n_i = \frac{a_i \cdot s_i}{\sum_{i=1}^{k} a_i \cdot s_i} \cdot 600$$

where

n_i = number of coupons to be apportioned to the ith subpopulation (surface areas of like zone at a given estimation point)

a_i = area size of the ith subpopulation

s_i = standard deviation (measure of burden variability of the ith subpopulation)

k = number of identified subpopulations

i = identifying number of a given subpopulation

Using this formula, some subpopulations, due to size of zone, would require more than 60 coupons and others less than 7, depending on the areas of the zones. Both conditions represent extremes from the statistical estimation standpoint: small gain of information for additional samples over 60; large loss of information for samples less than 7. Therefore, no subpopulation to be sampled at an estimation point would be assigned more than 60 coupons or less than 7 coupons.

The defined allocation formula requires known standard deviation (s_i) values. Since estimates of these values were not available, comparable relative variability factor weights were selected on the basis of biological judgment, which consisted of scoring a relative variability factor of 1 to 8 to the various subpopulation zone categories. Type 1 zone was assigned variability factors of 5 to 8, depending on how soon the subpopulation was sampled following contact by personnel; type 2 zone was assigned a variability factor of 4; type 3 zone a factor of 2; and type 4 zone a factor of 1.

In addition to the 600 coupons assigned by the coupon allocation plan, 700 "dummy" coupons were allocated for the following reasons:

(1) Personnel assembling the CMTM can bias the results by their conscious or subconscious awareness of coupons.

(2) In the event some coupons fall from their sites or are damaged during assembly, other coupons are available for substitution.

(3) Additional coupons may be desired for special studies.

d. Coupon removal procedure. As the final step in the development of the monitoring plan, a coupon removal

procedure was established to determine when the coupons should be removed in the assembly sequence:

(1) Immediately prior to the assembly of any subassembly, to serve as a control to identify initial burden.

(2) Before and after the eight chassis were assembled to the payload assembly.

(3) Before and after the impact limiter was lowered onto the payload structure.

(4) Before and after the aeroshell was assembled onto the payload structure.

(5) Before and after the parachute canister was assembled onto the payload structure.

(6) Before and after the deorbit motor was assembled to the payload structure.

(7) Before and after the relay link antenna was assembled to the payload structure. (At this point the CMTM is completely assembled.)

(8) Before and after a quarantine period. In this case representative samples were removed from all the exposed surfaces of the entire CMTM.

(9) Before and after the CMTM was lowered into the lower half of the sterilization canister.

(10) Just prior to mating the two halves of the sterilization canister.

Samples taken before steps 2 through 7 monitored those subassembly areas that would be occluded, mated, or made inaccessible by the assembly operation. Surfaces were sampled immediately before the subassembly was locked into place. To determine the amount of burden associated with assembly of any one subassembly, sampling data derived "before" installation of the subassembly was added to data derived "after" installation.

e. Test constraints. Extraneous variables affecting the biological burden must be controlled during assembly or the monitoring plan is subverted. For control of hardware, all subassemblies were wiped down with 90% isopropyl alcohol before sampling coupons were placed on the sites. Each coupon was then placed aseptically within 2 in. of its marked site. Immediately after the coupons were placed on a given subassembly, the unit was covered with a decontaminated (ethylene oxide) antistatic plastic cover. The subassembly remained covered until required in the assembly operation. Swab samples (numbering 47) were taken from all subassemblies before and after alcohol wipedown to establish a baseline for initial burden on the hardware for each assembly.

Test plans involving biological monitoring must define the decontamination of tools and equipment to be used in the assembly, the clothing to be worn by all personnel associated with the assembly operation, and the environmental control of assembly areas.

References

1. Redmann, G. H., "EASL/SADL Test and Operations," in *Semiannual Review of Research and Advanced Development, Vol. I*, Technical Memorandum 33-353, pp. 499–502. Jet Propulsion Laboratory, Pasadena, Calif., July 31, 1967.
2. Taylor, D. M., "Monitoring CMTM for Biological Burden During Assembly," paper presented at the American Society for Microbiology Meeting, Detroit, Mich., May 19, 1968.
3. *The NASA Standard Procedures for the Microbiological Examination of Space Hardware*, NHB 5340.1. National Aeronautics and Space Administration, Washington, Aug. 1967.

C. Propulsion

1. Chemical Heat Sources

a. Introduction. Research and advanced development studies are being conducted on potential chemical heat sources for the thermal control of future spacecraft and capsules. The long range goal of this effort is to develop a working prototype chemical heater model and demonstrate its continuous operation in a "breadboard" system configuration. Exothermic chemical reactions in general show a significant advantage over batteries in terms of the energy yield per unit weight of the heating system. However, various mission requirements impose a number of constraints on the design and operation of spacecraft chemical heaters, which in turn limit the number of chemical reactions that can be considered.

Scientific objectives, for example, require that a chemical heat source aboard a planetary lander produces no gaseous products of combustion that are vented overboard, for these could be detected by the capsule's scientific instrumentation and erroneously interpreted to be indigenous to the planet. Such a restriction eliminates from consideration ordinary liquid- or solid-propellant combinations, which produce large volumes of gaseous products containing such species as carbon, hydrogen, nitrogen, and halogens. Sterilization requirements make it necessary that a chemical heater withstand elevated temperatures (on the order of 275°F) for extended periods of time prior to launch, thus disqualifying chemical reactants that would thermally decompose or exhibit inordinately high vapor pressures under those conditions.

Furthermore, a heater used aboard a "hard-landing" capsule is required to be impact-resistant and to operate in any position (even upside down or sideways) depending on the orientation of the capsule when it comes to rest on the planet's surface.

Three major classes of exothermic chemical reaction have been selected for preliminary evaluation in this program. They are classified in terms of the state of the *reactants* at room temperature as solid–solid, solid–liquid, and liquid–liquid reactions. Within these classes, only those reactions whose *products* are all solids at room temperature are being considered. Since no gases are produced, none of these chemical agents can be regarded as propellants. This article presents the results of the analysis and experimentation carried out to date with the solid–solid class of reactions. Future articles will be devoted to the solid–liquid and liquid–liquid work.

b. All-solid chemical reactions. An all-solid chemical reaction is defined as one in which all the reactants and products are in the solid state at room temperature. Depending on the quantity of heat released by a reaction and the nature of its products, it may be possible in some cases for one or more of the products to temporarily exist in the liquid or even the gaseous state prior to cool-down.

All-solid reactions are not unfamiliar in modern technology. Spice and Staveley (Ref. 1) studied the heats of reaction (ΔH_r) and rates of burning for 18 all-solid reactions. Taylor (Ref. 2) reports a number of commercial applications, including the Goldschmidt welding process, photoflash and incendiary munitions, and various kinds of fuses and detonators. Another application was a self-heating food can (Ref. 3) used by the Allies in World War II. There are also several patents[3] for devices using the all-solid reactants in plastic or sheet form.

Although the all-solid reactions generally release only 20–25% of the energy (in Btu/lbm of reactants) available from liquid–liquid or liquid–solid reactions, they may still prove to be competitive because of their increased simplicity and reliability. The reactants could be intimately mixed and prepackaged into a number of small modules that would remain quiescent until activated in sequence on demand by a simple firing circuit. The need for liquids or gases under pressure would be eliminated, thus reducing overall system weight and eliminating liquid and gas leak sources. The lack of any liquid components would also facilitate sterilization.

Five all-solid reactions were selected for a series of initial screening tests to choose the most promising candidate for use in a prototype chemical heater design. These were:

$$8Al + 3KClO_4 \rightarrow 3KCl + 4Al_2O_3 \quad (\Delta H_r = -4320 \text{ Btu/lbm reactants}) \tag{1}$$

$$2Al + 3CuO \rightarrow 3Cu + Al_2O_3 \quad (\Delta H_r = -1750 \text{ Btu/lbm reactants}) \tag{2}$$

$$8Al + 3Fe_3O_4 \rightarrow 9Fe + 4Al_2O_3 \quad (\Delta H_r = -1530 \text{ Btu/lbm reactants}) \tag{3}$$

$$3Mn + KMnO_4 \quad (\Delta H_r = -1325 \text{ Btu/lbm reactants}) \tag{4}$$

$$CaSi_2 + 0.416\,Fe_3O_4 \quad (\Delta H_r = -1035 \text{ Btu/lbm reactants}) \tag{5}$$

The first reaction is perhaps the most energetic all-solid reaction known. Mixtures of aluminum and potassium perchlorate have been commercially available[4] for over 25 yr, and have been used in applications such as torpedo fuses. However, one of the products, potassium chloride, is a relatively volatile salt which may temporarily exist in the vapor state at the transient elevated temperatures associated with the reaction. It was anticipated that this property might lead to rupture of a completely enclosed container.

Reaction (3) is the familiar thermite reaction used in the Goldschmidt welding process, producing molten iron and alumina slag. Reaction (2) is similar to (3), except that the metal involved is copper, and the energy release is somewhat higher. The proportions of reactants for reactions (4) and (5) are not necessarily stoichiometric; some doubt exists as to the products formed, although they are apparently all solids. Reaction (4) exhibited the highest energy yield of all the reactions studied in Ref. 1, while reaction (5) was the composition chosen for use in the self-heating food can (Ref. 3).

These combinations span a relatively wide heat-of-reaction range, the theoretical ΔH_r of reaction (1) being

[3] Francis, T., and Jones, M. H., *Chemical Heating Device in Sheet Form*, U. S. Patent No. 3311459, Mar. 28, 1967; Beale, J., and Crathorne, J. A., *Exothermic Compositions*, British Patent No. 1063050, Mar. 30, 1967.

[4] Aerojet-General Corp., Chemical Power Dept., Azusa, Calif.

over four times that of (5). In addition, all use commercially available materials, which are reported to be readily ignited, and may be intimately mixed without spontaneous ignition taking place.

A brief experimental program was conducted to screen the five reactions and to uncover any potential problem areas associated with their use in chemical heater elements.

c. Apparatus and procedures. Three types of expedient containers for the reactants were used: single capsules or "modules," single tubes, and multiple-module configurations. All three types were fabricated from stock materials on hand at JPL's Edwards Test Station; detailed heat transfer or thermal stress calculations were not considered in their design.

The single capsules were constructed as shown in Fig. 2a. The powdered reaction mixture was contained in a short section of 1-in. stainless-steel tubing enclosed at the bottom by a welded plate and at the top by a flared-tube fitting and threaded cap. Cavities of different volumes were machined into the caps, so that the ullage (free space above the reacting mixture) could be varied under controlled conditions. An igniter assembly, incorporating a length of nichrome resistance wire, is shown in the foreground of Fig. 2a. The wire entered the capsule through a series of fittings in the bottom plate. When the capsule was charged with reactants, the igniter assembly was short-circuited with a spring-clip until firing time. A direct current of 28 V was used to energize the firing circuit. A chromel-alumel thermocouple, referenced to 150°F, was attached to the exterior surface of each device.

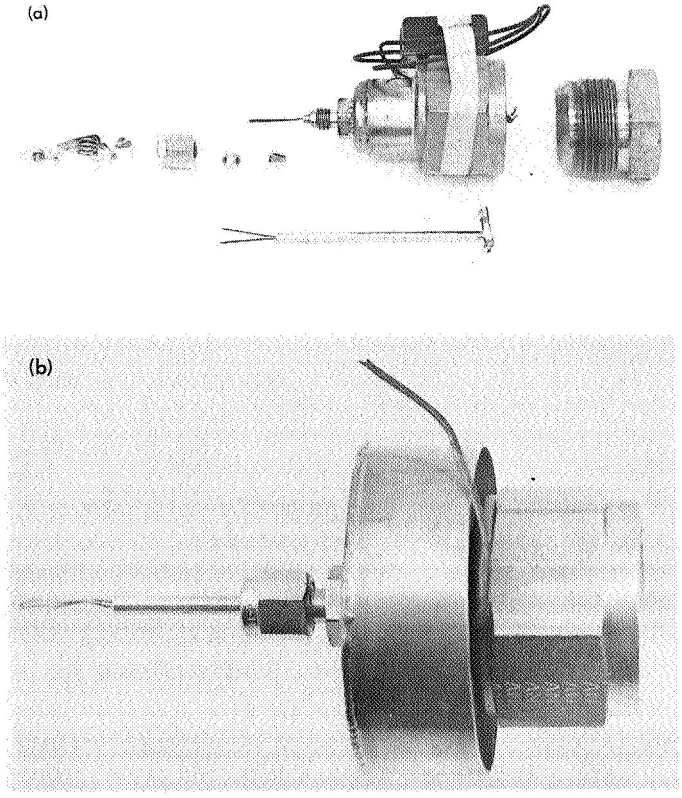

Fig. 2. Single capsule test device: (a) typical configuration, (b) modified for Mn/$KMnO_4$ test

The single tubes were fabricated from 0.25-in. outside-diameter, nominally 0.030-in.-wall copper tubing. Each tube was 13.5 in. long and crimped at both ends. The igniter wire (0.025 × 1.5-in. nichrome) entered the assembly at one end, and a thermocouple was welded to the opposite end. These tubes were filled with a packed mixture of aluminum and copper oxide. A primer, when used, consisted of a loose mixture of aluminum and barium dioxide in contact with the igniter wire. The single-tube configuration was screened to assess the feasibility of using it as the basic element of a "tube-bundle" heater. Similar tubular heaters, containing a gasless pyrotechnic mixture of proprietary composition, are available commercially,[5] so the evaluation of this particular configuration represented a relatively minor portion of the total effort.

[5] Atlas Chemical Industries, Inc., Valley Forge, Pa.

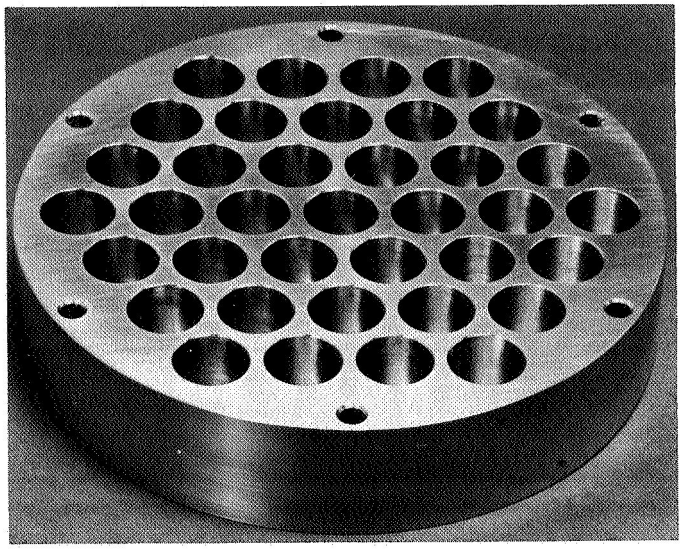

Fig. 3. Multiple-module test device

The multiple-module configuration (Fig. 3) consisted of a 4.5-in.-diam copper plate containing 37 cylindrical compartments each 0.5 in. in diameter and 0.75 in. deep arranged on 0.6-in. equilateral triangular centers. A mating top plate and asbestos gasket enclosed the reactants and sealed the individual containers. The igniter wires were introduced into each compartment through the cover plate. The main purpose of this device was to determine if the ignition of one charge would trigger the spontaneous ignition of surrounding charges in a high-conductivity, high-heat-capacity configuration such as might be found in a prototype heater. Thermocouples were attached to the bottom of those compartments where ignition was to take place. Ullage was varied by adjusting the volume of charge placed in each compartment.

The charges of reactants were tightly compacted into the various containers. In some cases, to facilitate ignition, priming mixtures were poured on top of the main charges in loose layers in contact with the igniter wires.

d. Results and discussion.

Al/$KClO_4$ reaction. A single test of the Al/$KClO_4$ combination was made. An 8-g charge containing 34.2 wt % aluminum was packed into a single steel container of the type shown in Fig. 2a. The primer was 1.2 g of a loose mixture of the same composition. The capsule was half full (50% of its total volume was ullage space). The test device exploded upon ignition; inspection of the failed capsule indicated that severe internal overpressurization had occurred. Whether this was the result of temporary volatilization of the solid products, or of oxygen being released from the decomposing potassium perchlorate faster than it could be consumed in formation of the aluminum oxide, has not been established. The net result, however, was that this combination was determined to be infeasible for use in spacecraft heaters. Thick-walled reaction vessels would be required to contain the high-pressure gases generated, or some complex provision for harmless expansion would have to be made.

Al/CuO reactions. Two tests of the Al/CuO system in single steel capsules were made. In one, the capsule was essentially full, containing 29.9 g of tightly packed charge consisting of 18.4 wt % aluminum. In the other, approximately 50% ullage was used, the charge being 14.7 g of the same composition. In both cases, the primer was a loose layer of a mixture containing equal weight proportions of aluminum and barium dioxide. This material is typically used as a primer for the thermite reaction. Ignition was smooth and rapid, with the outside wall of the essentially full capsule attaining a maximum temperature of 1860°F in 3 s. The temperature–response curve for this reaction is shown in Fig. 4. The half-full capsule reached a maximum temperature of only 1090°F. In both tests, however, failures occurred in the stainless-steel containers (Fig. 5a) resulting in the expulsion of a portion of the molten copper-alumina product mixture. A metallographic analysis of the failed capsules indicated that failure occurred because of the presence of microcracks in the tubing wall (Fig. 6), which acted as stress risers. These were apparently created during the field-expedient welding process, during which no effective process controls were applied. The microcracks appeared to have been enlarged by the extreme thermal stresses associated with the rapid heat release of the reactions, providing routes for penetration of the very hot and fluid metallic reaction products. Once the tubing had been breached, the holes evidently continued to enlarge due to the flow of the molten metal. However, no evidence was found of any internal pressurization as a result of the reaction, which substantiates the gasless nature of the reaction.

Another effect associated with this solid–solid system (as with others studied) was a decrease in total volume and an increase in bulk density as a result of the reaction. As shown in Fig. 5b, considerable contraction of the solid mix typically resulted after the reaction took place.

The copper multiple-module test device (Fig. 3) was used next. The central hole and the 6 holes immediately surrounding it were all loaded about 75% full (approximately 5.5 g each) with the same, compacted, Al/CuO composition. A small quantity of loose Al/BaO_2 primer was loaded on top of the main charge in the central container. The central charge was successfully ignited, but none of the surrounding charges was set off, indicating sufficient flow of heat from the area surrounding the central charge into the copper heat sink that the autoignition temperature of the other charges was not attained. A peak temperature of 605°F was recorded in the area of the central charge 0.9 s after ignition (Fig. 7). The temperature of the test device remained fairly constant (~120°F) after 20 s, cooling only slowly due to the high heat capacity of the copper. The test device was undamaged, and there were no signs of melting, cracking, or burning through. These results were to be expected, considering the one-piece, relatively stress-free construction of the test device, and the thermal properties of the material from which it was made.

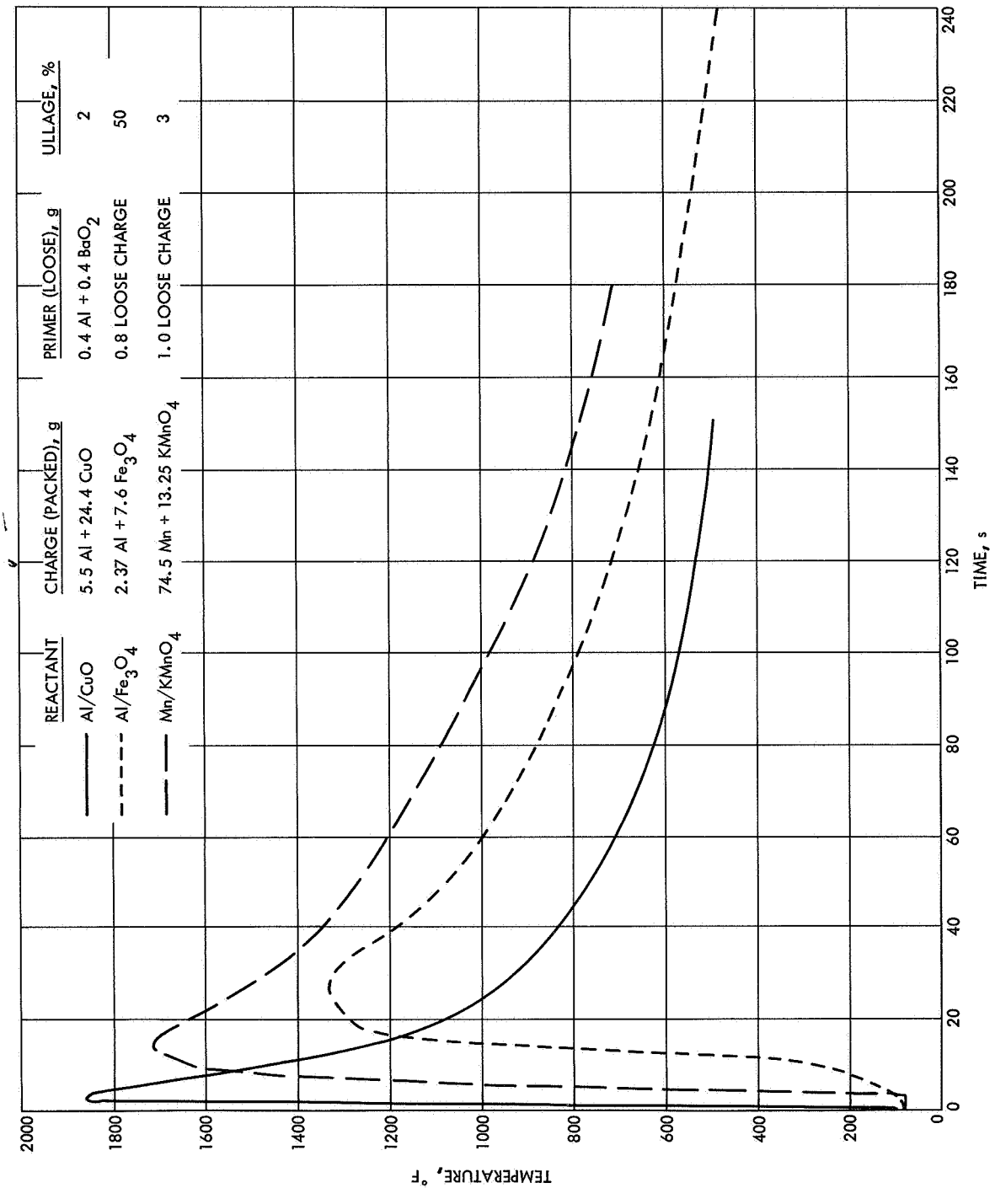

Fig. 4. Temperature response at outside wall of single steel capsule during Al/CuO, Al/Fe_3O_4, and Mn/$KMnO_4$ reactions

A chemical analysis performed on the residue from the central hole determined that the reaction was 96.8% complete. This is in agreement with the results obtained with the other reactions, and indicates the near-theoretical energy release to be expected with the all-solid reactions.

Another test was made with this configuration, with all conditions being the same except that no primer was used. The results were essentially identical. The central charge successfully ignited, but none of the surrounding charges were set off. Despite the lack of primer, ignition was normal. No delay was encountered, and the temperature–time history of this test was nearly identical to that of the previous one.

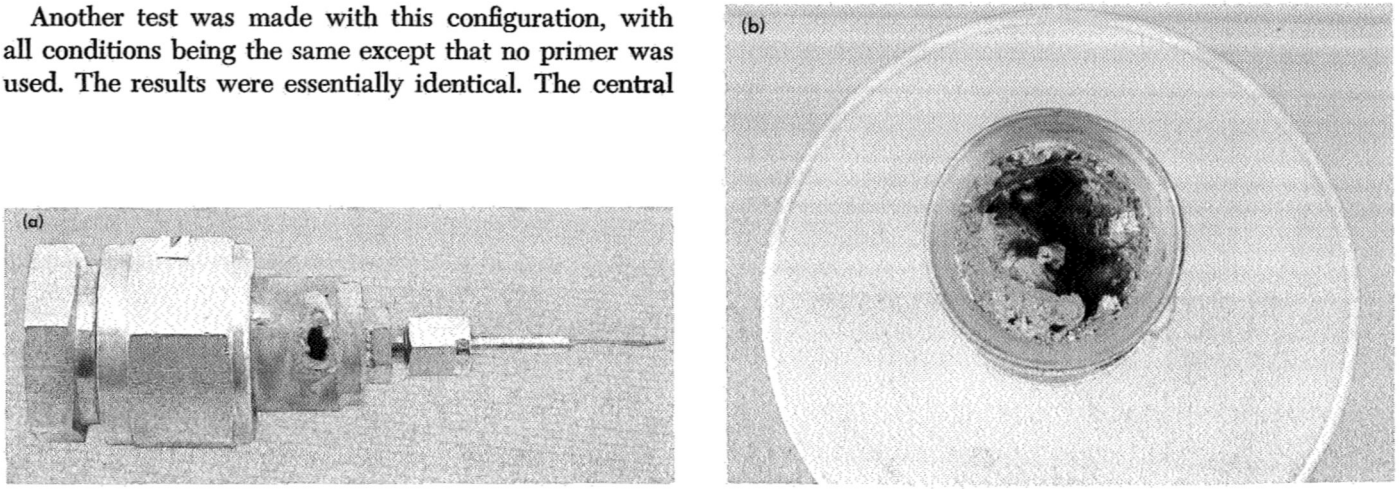

Fig. 5. Post-test appearance of steel capsules used for Al/CuO reaction: (a) capsule half full, (b) capsule full

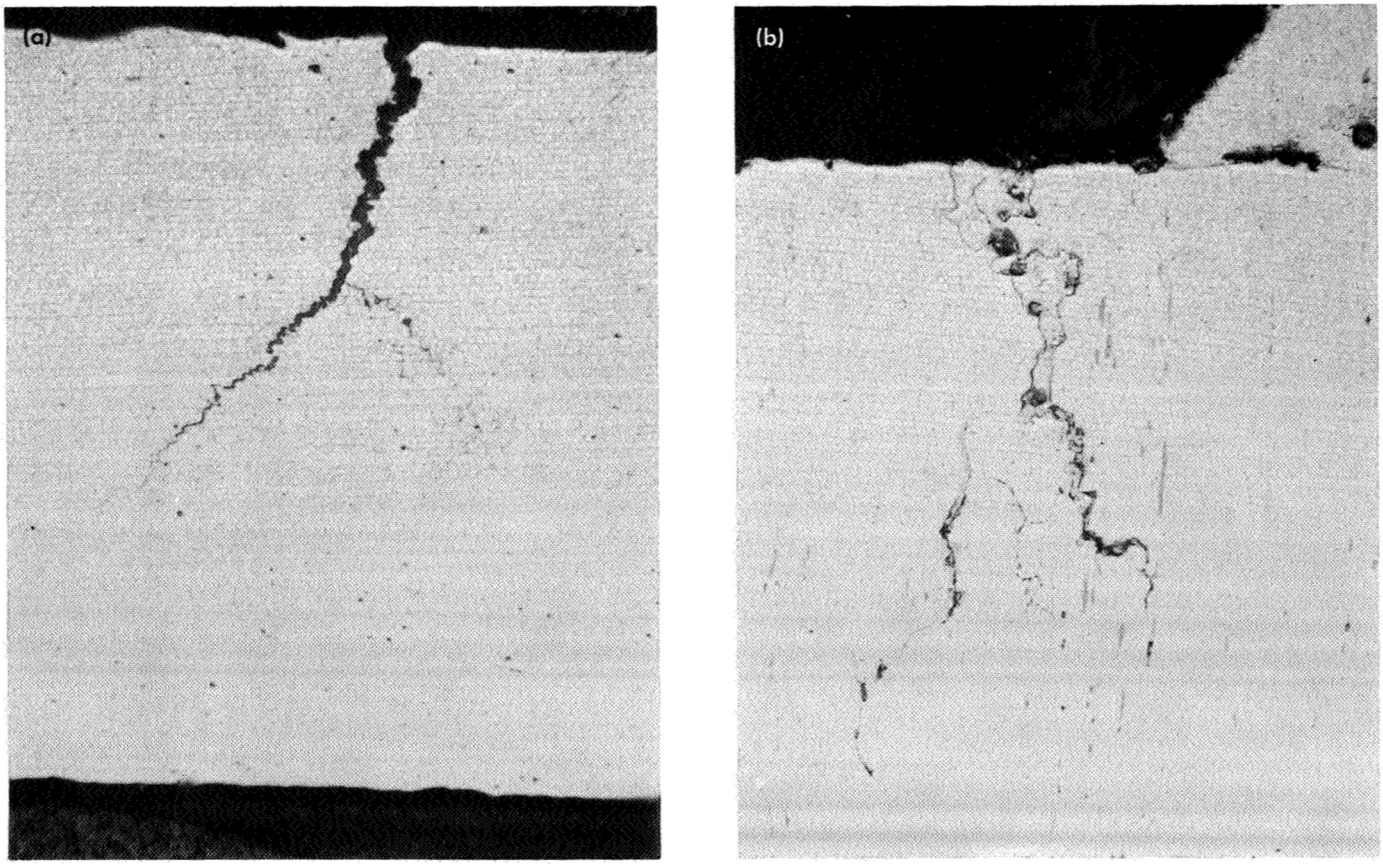

Fig. 6. Microcracks in walls of steel capsules: (a) enlarged by thermal stress, (b) infiltrated with molten metal

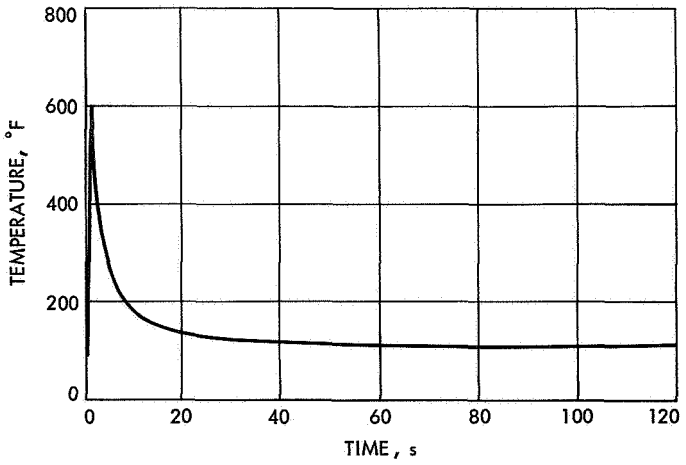

Fig. 7. Temperature response at outside wall of copper multiple-module test device during Al/CuO reaction

Finally, three tests of the Al/CuO system were made using the single-copper-tube containers. In two of these, employing 20.7 g of packed charge and 1.1 g of loose primer, ignition failed to occur. In the third, conducted without a primer, ignition was accomplished, but the reaction propagated only several inches down the tube, and then became extinguished. The copper walls of the tube melted in the reaction zone. Further experimentation with the tube configuration was not made due to the successful demonstration of the multiple-module concept, and the reported availability of commercial tubular devices. The results suggest, however, that the relative ease of ignition and propagation of all-solid reactions may depend on the reactor geometry. The amount of heat dissipated through the relatively large surface area of the tubular configuration, compared to that of the capsules, may be too great for ignition and propagation to take place.

Al/Fe_3O_4 reactions. Three tests of the Al/Fe_3O_4 (thermite) mixture in single steel capsules were carried out. In the first, the capsule was essentially full of compacted charge and no primer was used. An 8.5-s ignition delay was encountered (the nichrome wire burned out in 0.67 s) and failure occurred in the capsule, expelling most of its contents. Again, metallurgical analysis showed the cause of failure as microcracks in the parent metal adjacent to the welds, which probably resulted from the field-expedient fabrication techniques.

The next two tests used 50% ullage space above the charge; one had a loose layer of Al/BaO_2 primer on top of the main charge while the other did not. Smooth ignition was obtained in both cases and neither capsule failed, probably due to the smaller quantities of reactants. As shown in Fig. 4, the capsule outside-wall temperatures reached typical maxima of about 1330°F, but the peaks occurred between 20 and 30 s after ignition, indicating a slower reaction rate than with the Al/CuO combination. The results of these experiments leave some doubt as to whether a primer is actually required for the Al/Fe_3O_4 system. However, in view of the ignition delay recorded in one instance when no primer was used, it appears that a primer would be desirable. The residue from the last two tests was subjected to chemical analysis, which determined that 99.25 wt % of the reactants had reacted to form products in one case, and 99.50 wt % in the other. The degree of completion of this reaction indicates that a near-theoretical heat release (reaction 3) may be expected.

Mn/$KMnO_4$ reactions. The fourth chemical combination to be screened was Mn/$KMnO_4$. Three tests were conducted, the first two being in single capsule devices similar to that shown in Fig. 2a. The last employed a single capsule apparatus modified by welding an open-topped cylindrical can in position around it (Fig. 2b). This can was then filled with the Mn/$KMnO_4$ mixture to check for autoignition when the central charge was set off.

In the first test, 20.7 g of a mixture containing 36 wt % manganese powder was tightly tamped into a single steel capsule which was essentially full (3% ullage). The primer consisted of 1.0 g of loose main charge, while a 0.75-in.-long, 0.025-in.-diam nichrome wire formed the igniter.

Although the igniter wire burned through completely after carrying current for 0.66 s, ignition failed to occur. Therefore, the test was repeated with a greater length (2.5 in.) of nichrome wire, all else being the same. This time smooth ignition took place (after what appeared to be a 5-s delay) and the outside-wall thermocouple registered a maximum temperature of 1715°F at 15 s (Fig. 4). The capsule remained intact. In the final test, 74.2 g of lightly packed powder in the external can surrounded the 21-g main charge in the capsule. Again, using the longer igniter wire, smooth ignition was obtained and the surrounding charge did not spontaneously ignite, even though the outer wall of the inner capsule attained a peak temperature of 1756°F.

A chemical analysis of the residues from the two successful Mn/$KMnO_4$ tests indicated that 98.1 wt % of

the reactants had reacted to form products in one case, and 91.2 wt % in the other. The difference between these two figures may be due to samples taken from two different locations within the residue, but the indicated degrees of completion of the reaction are nevertheless encouraging.

$CaSi_2/Fe_3O_4$ reactions. Three tests of the $CaSi_2/Fe_3O_4$ system in single steel capsules were made. In all three tests, the primer mixture recommended in Ref. 3 (30% $CaSi_2$ and 70% Pb_3O_4) was used. In each case the primer was successfully ignited, but the main charge could not be made to react. In one test, a layer of thermite was placed between the primer and the main charge, but it also failed to ignite. Further effort with this combination was considered to be unwarranted due to its low theoretical energy yield.

e. Conclusions. The results of this work have demonstrated that the chemical combinations Al/CuO, Al/Fe_3O_4, and Mn/$KMnO_4$ are essentially gasless, generating only solid products, and may be reacted in completely sealed containers with no ill effects, provided that sufficient attention is paid to the design of the reaction containers. All fabrication processes should be carefully controlled to eliminate stress risers, such as internal defects, tool marks, or microcracks resulting from welding. The combustion devices should be annealed after fabrication. The order in which the reactions are listed is also the order of decreasing thermal energy release and maximum temperature attained in a given reactor configuration. Reliable ignition of these combinations seems quite feasible, but is predicated on the use of a suitable priming compound and igniter wire combination. Considerable attention should be paid to igniter design during the development of a prototype chemical heater.

Since these reactions are generally rapid (completed in a matter of seconds), the reactants release their heat very quickly. The temperature rise and decay curves will depend on the thermal properties and geometry of the particular reactor within which the reaction is confined. Since the chemical reactions proceed essentially to completion, it may be inferred that nearly 100% of the thermal energy release predicted from heat-of-formation data (reactions 2–4) may be actually realized.

The experiments have also demonstrated the feasibility of using the solid–solid reactants in multiple-module or other configurations wherein a number of discrete charges are prepackaged in close proximity to each other. The lack of autoignition under these circumstances indicates that these compounds will not prematurely ignite under the relatively milder thermal conditions encountered during a sterilization cycle.

Although not specifically investigated, other environmental conditions such as impact, orientation, or gravity effects are not expected to affect the performance of completely filled devices containing tightly tamped heating compounds. The insensitivity of the reactions to ullage was demonstrated.

Based on the results of these preliminary screening tests, the all-solid class of exothermic reactions, in general, and the chemical combinations Al/CuO, Al/Fe_3O_4, and Mn/$KMnO_4$, in particular, is considered to be feasible for use as chemical heat sources for spacecraft. Chemical heaters based on these reactions should be simple, economical, rugged, and reliable, containing no moving parts, producing no gaseous products, and involving no liquids or gases under pressure.

Chemical combinations Al/$KClO_4$ and $CaSi_2/Fe_3O_4$ were determined to be unsuitable for application to a spacecraft heater; the first because it reacted explosively, and the second because of a combination of low-energy yield and difficulty in ignition.

References

1. Spice, J. E., and Staveley, L. A. K., "The Propagation of Exothermic Reactions in Solid Systems," *J. Soc. Chem. Ind.*, Vol. 68, p. 348, Dec. 1949.
2. Taylor, J., "Solid Propellant and Exothermic Compositions," *Interscience*, p. 135, New York, 1959.
3. Caldwell, W. A., and Gillies, J., "The Development of a Self-Heating Food Can," *The Industrial Chemist*, p. 301, July 1950.

D. Environmental Sciences

1. Blunt Cone Base Pressure

Tests were conducted in the JPL supersonic wind tunnel to determine the detailed base pressure distribution on two blunted cones. The two models, 60- and 45-deg half-angle cones, were investigated through a Mach number (M) range of 0.3 to 3.5 at angles of attack of 0 and 20 deg. Both sharp edge models had a nose radius to base diameter ratio of 0.1 (Fig. 8). The 2-in.-diam aluminum cones were both mounted on a common base which, in turn, was attached to a tapered sting having a 0.25-in. diam at the model base. The 0.05-in.-diam pressure ports were aligned in a radial line on the base–sting apparatus common to both models.

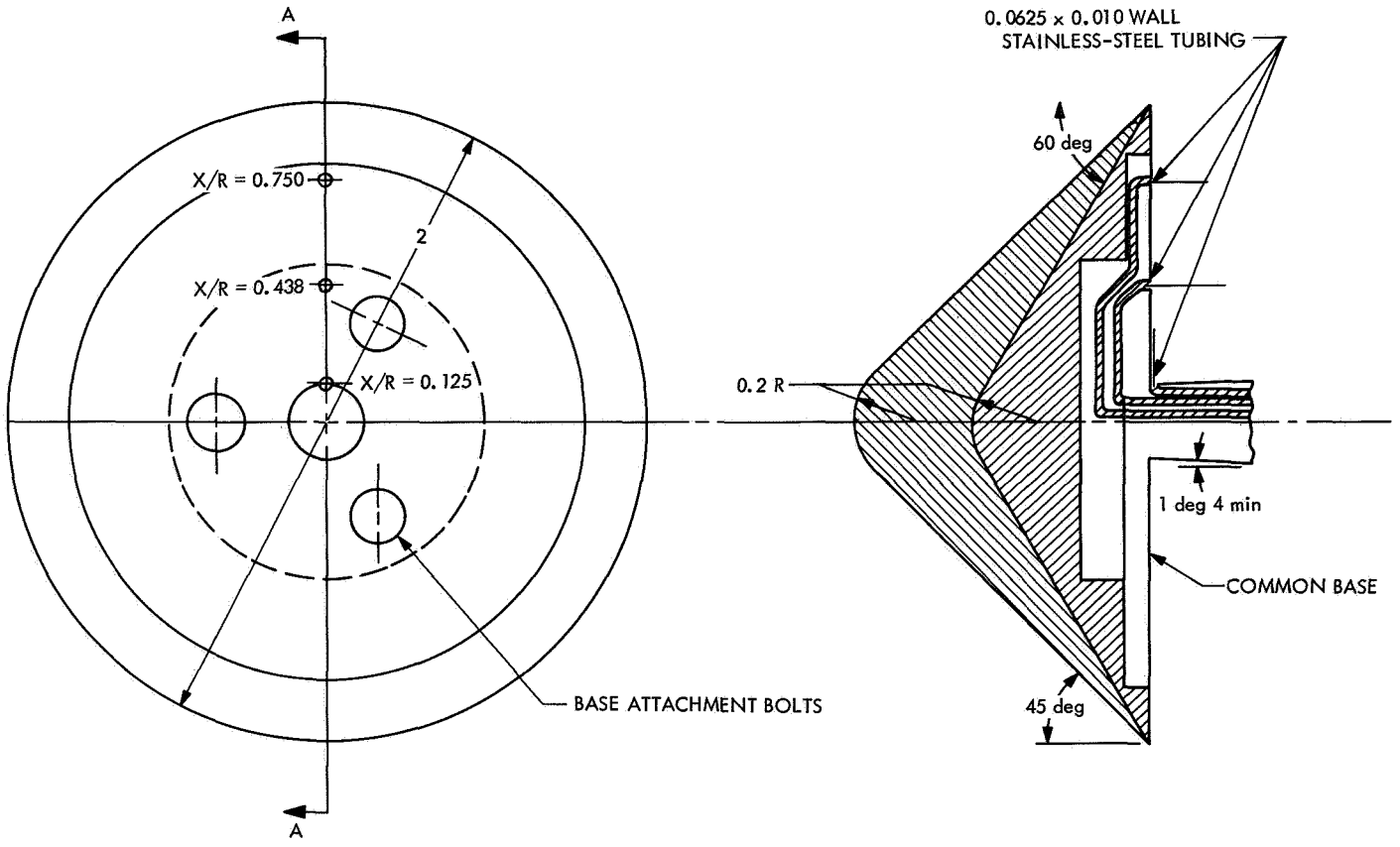

Fig. 8. Configuration of the 60- and 45-deg half-angle cones

To obtain a distribution over the base, the cones were rolled through a total angle of 180 deg at 90-deg intervals at each angle of attack. With the model at zero roll angle, the base port ray was in a horizontal position; positive roll was then clockwise as viewed facing upstream.

The JPL 100-port multiple-pressure measuring system was used to measure and record the base pressures. The system was advanced automatically after lag times had been established.

Several spark shadowgraphs were taken of both models at all Mach numbers to define and study the wake shapes and flows.[6]

The wake boundary behind a blunted cone at subsonic Mach numbers is very similar to that predicted by hydrodynamic free-streamline theory; i.e., the flow sheds off the model edge and a wide eddying wake with no discernible neck or throat forms aft of the body. Subsonically, the shape of this boundary is very insensitive to Mach number variation. A "dead air" region forms immediately behind the body in the near wake, and no reverse flow condition exists. With a similar body in supersonic flow, an expansion fan occurs at the model edge as the flow is turned back towards the longitudinal body axis. At some distance aft of the model base, the wake necks down and a recompression shock is formed (Fig. 9).

Figure 10 presents the average base pressure ratio of the three base ports as a function of Mach number for the two bodies at two angles of attack. Three phases are evident: (1) a subsonic regime in which the ratio, though changing rapidly with Mach number, is quite insensitive to body shape and angle of attack in the ranges investigated; (2) a transonic and low supersonic regime in which the effects of variation in these parameters become more distinct; and (3), as the Mach number is increased still further, a minimum in the base pressure ratio is reached for $2.5 < M < 3.0$.

The Reynolds number has a distinctive influence on the viscous mixing and wake boundary layer. In the transition region from laminar to turbulent wake, an increase in Reynolds number resulted in a reduction in the pressure ratio.

[6]Kurtz, D. W., and Kerr, W. R., *Base Pressure Distribution of Two Blunted Cones at Mach Numbers From 0.3 to 0.8 and 1.81 to 3.51*, Technical Memorandum 33-403. Jet Propulsion Laboratory, Pasadena, Calif. (in press).

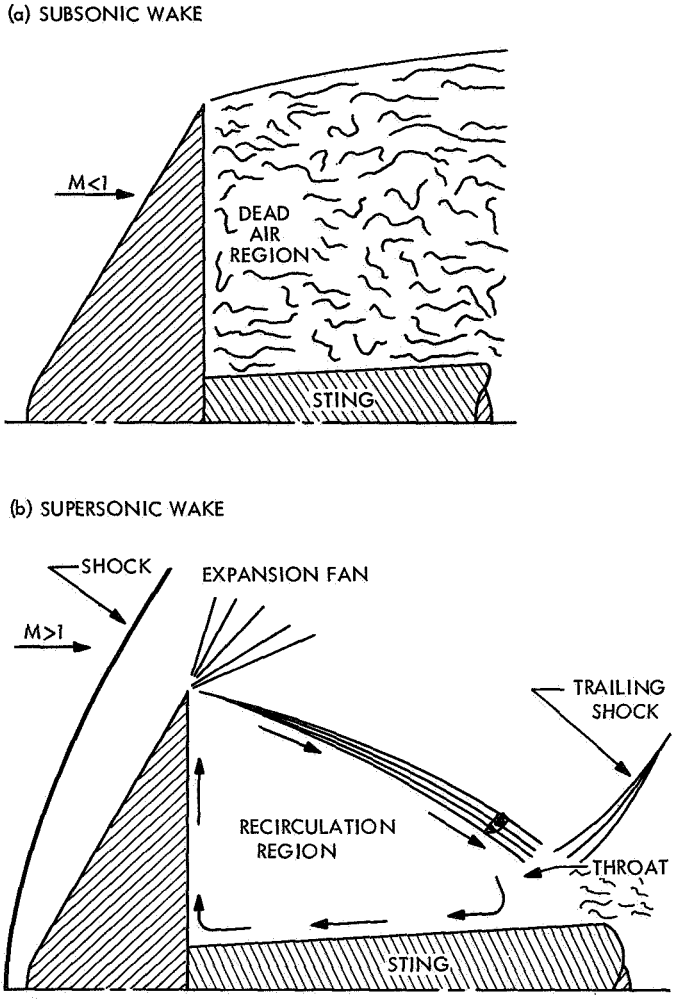

Fig. 9. Typical subsonic and supersonic wake flow patterns

In general, the base pressure decreases with increasing cone angle due to the expansion fan strength at the cone edge.

2. Entry Capsule Dynamics During Terminal Descent

As an entry capsule approaches terminal conditions, the once-negligible gravity force becomes comparable in size to the aerodynamic forces and has a strong influence on the angle-of-attack motion.

The two important effects occur near and at terminal conditions, making this regime different from others:

(1) The normally destabilizing effect of aerodynamic drag is substantially, if not totally, nullified by gravity, since gravity acts opposite to the drag force.

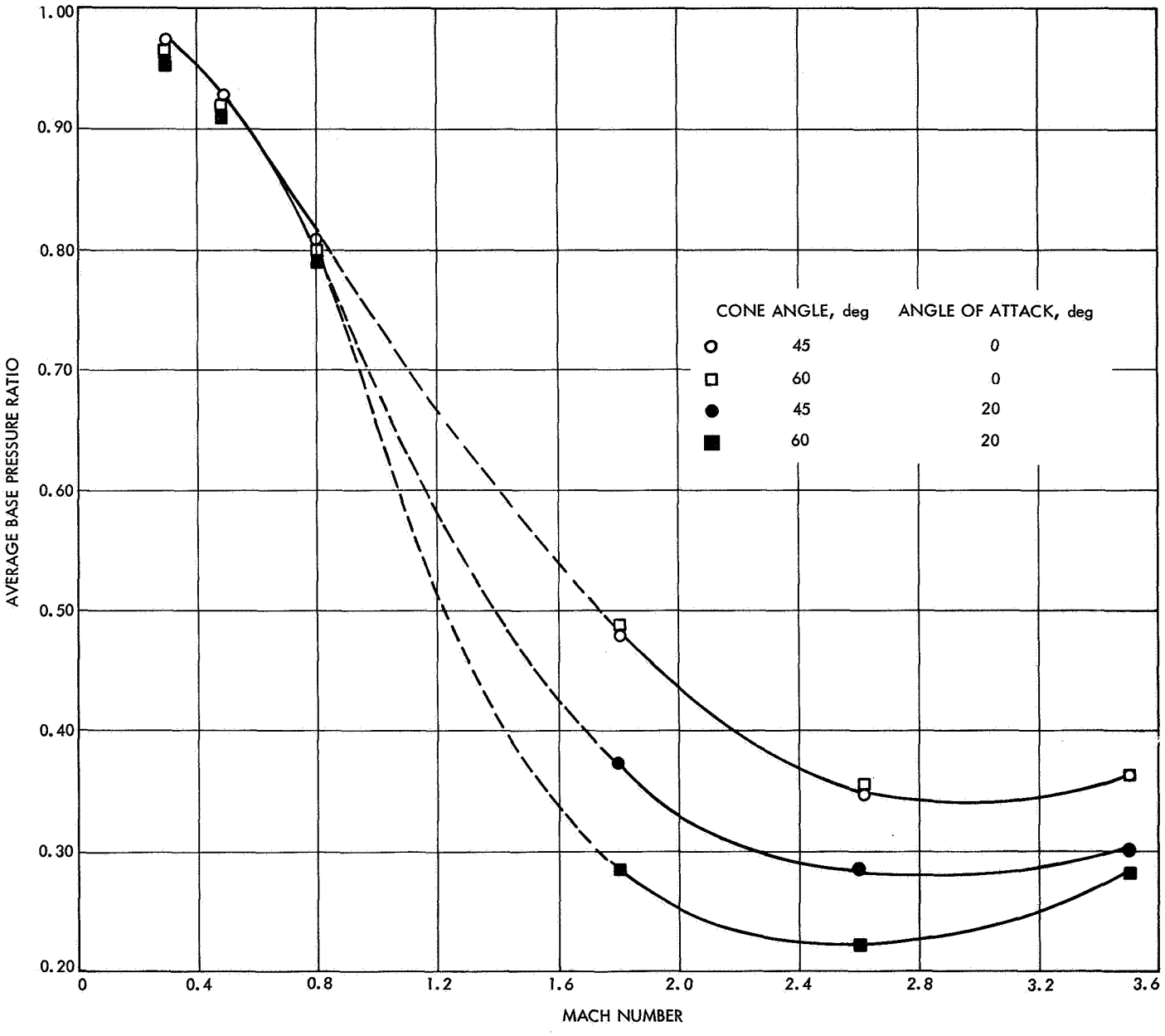

Fig. 10. Average base pressure ratio trend over a range of Mach numbers

(2) A small component of gravity acting opposite to the aerodynamic normal force produces a negative normal force, which has a destabilizing effect.

The orientation of the capsule and the forces acting on it are depicted in Fig. 11, wherein γ is the inertial reference angle measured between the inertial X axis and the body centerline x; ξ is the total angle of attack measured between the velocity vector $\overline{V}$ and x. The inertial X axis is referenced to the planet's gravity vector by the angle θ. For easy visualization, X and x have been drawn in the same plane. In general, however, x and $\overline{V}$ will not be in the same plane as X and gravity.

By viewing ξ as a complex angle $\beta + i\alpha$, assuming linear aerodynamics and small angles of attack ($\sin \xi = \xi$; $\cos \xi = 1$), and using the distance traveled along X as the independent variable, the following differential equation can be developed:

$$\xi'' + \xi'\left[\rho\overline{H} + 2\left(\frac{\dot{X}'}{\dot{X}}\right) - iP\right] - \xi\left[\rho M + i\rho P\overline{T} + iP\left(\frac{\dot{X}'}{\dot{X}}\right) - \rho'\frac{A}{2m}C_{N_\alpha} - \frac{d\left(\frac{\dot{X}'}{\dot{X}}\right)}{dX}\right] = 0 \qquad (1)$$

where

$$\overline{H} = \frac{A}{2m}\left[C_{N_\alpha} - \frac{md^2}{I}\left(C_{m_q} + C_{m_{\dot{\alpha}}}\right)\right] - \frac{g}{\rho V^2}\frac{\sin(\theta+\gamma)}{\xi} \qquad (2a)$$

$$\overline{T} = \frac{A}{2m}\left[C_{N_\alpha} + \frac{md^2}{I_x}C_{m_{p_\alpha}}\right] - \frac{g}{\rho V^2}\frac{\sin(\theta+\gamma)}{\xi} \qquad (2b)$$

$$M = \frac{Ad}{2I}C_{m_\alpha} \qquad (2c)$$

$$P = \frac{I_x}{I}\frac{p}{V} \qquad (2d)$$

$$\frac{\dot{X}'}{\dot{X}} = \rho\left\{-\frac{AC_D}{2m} + \frac{g}{\rho V^2}\cos[\theta + (\gamma - \xi)]\right\} \qquad (2e)$$

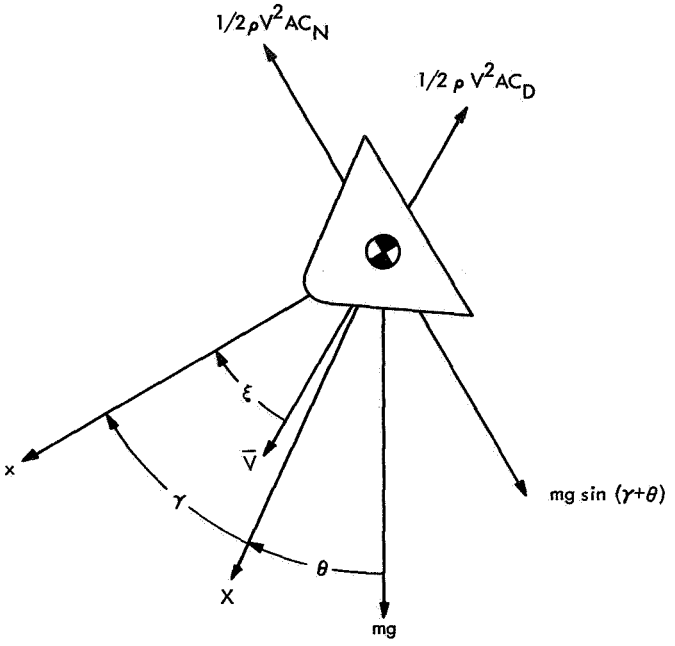

Fig. 11. Orientation of capsule and forces acting on capsule

with

A = cross-sectional area of body

m = mass

C_{N_α} = normal force slope coefficient

d = cross-sectional diameter of body (reference length)

I = transverse moment of inertia

$(C_{m_q} + C_{m_{\dot{\alpha}}})$ = dynamic stability coefficient

g = gravitational acceleration

V = velocity

I_x = longitudinal moment of inertia

$C_{m_{p_\alpha}}$ = magnus moment coefficient

p = roll rate

and

$(\,)'$ denotes derivative operation with respect to X

$(\dot{\cdot})$ denotes derivative operation with respect to time

When terminal conditions have been reached, the total force action on the body along its flight path remains

constant, and is stated mathematically as

$$m\dot{V} = -\frac{1}{2}\rho V^2 AC_D + mg\cos[\theta + (\gamma - \xi)]$$
$$= \text{constant} \tag{3a}$$

As this terminal condition is approached, gravity tends to take hold and bend the flight path so that it is normal to the planet surface and collinear with the gravity vector, which is approximately equivalent to $\theta = 0$. Furthermore, the angle $(\gamma - \xi)$ is extremely small, generally less than half a degree, and can be assumed to be zero. Thus, Eq. (3a) reduces to

$$m\dot{V} = -\frac{1}{2}\rho V^2 AC_D + mg = \text{constant} \tag{3b}$$

For a constant drag coefficient, which is a basic assumption of linear aerodynamics, this equation implies that the dynamic pressure $1/2\rho V^2$ is constant during the terminal portion of entry.

The gravity producing negative normal force appears to be small when the flight path is collinear with gravity (since θ is essentially zero); however, since it is proportional to sin ξ (or ξ for small angles), it can be the same order of magnitude as the aerodynamic normal force:

$$\text{Total normal force} = \frac{1}{2}\rho V^2 AC_{N_\alpha}\xi - mg\xi$$
$$= m\rho V^2 \xi\left(\frac{A}{2m}C_{N_\alpha} - \frac{g}{\rho V^2}\right) \tag{4}$$

During the early phase of entry, the quantity ρV^2 is several orders of magnitude greater than g. However, during terminal descent, it becomes substantially smaller resulting in $g/\rho V^2$ having an influence on the total normal force and perhaps even becoming dominant.

If the above simplifications for flight-path angle and small $(\gamma - \xi)$ are incorporated into $\bar{H}$, $\bar{T}$, and $(\dot{X}'/\dot{X})$, they reduce to

$$\bar{H} = \frac{A}{2m}\left[C_{N_\alpha} - \frac{md^2}{I}(C_{m_q} + C_{m_{\dot{\alpha}}})\right] - \frac{g}{\rho V^2}$$
$$= \text{constant} \tag{5a}$$

$$\bar{T} = \frac{A}{2m}\left(C_{N_\alpha} + \frac{md^2}{I_x}C_{m_{p_\alpha}}\right) - \frac{g}{\rho V^2} = \text{constant} \tag{5b}$$

$$\frac{\dot{X}'}{\dot{X}} = \rho\left(-\frac{AC_D}{2m} + \frac{g}{\rho V^2}\right) = \rho \cdot \text{constant} \tag{5c}$$

For atmospheric entry, where the medium density ρ is constantly changing, Eq. (1) is nonlinear and cannot be solved explicitly. However, an accurate approximate solution can be obtained using the Wentzel–Kramers–Brillouin (WKB) method (Ref. 1) and assuming an exponentially changing density. This approach yields the solution

$$\xi = \frac{\exp\left\{-\frac{1}{2}\int_0^X\left[\rho\bar{H} + 2\left(\frac{\dot{X}'}{\dot{X}}\right)\right]dX\right\}}{\left(\frac{G}{2}\right)^{1/2}}$$
$$\times\left\{K_1\exp\left[\frac{1}{2}i\int_0^X(P+G)\,dX\right]\right.$$
$$\left. + K_2\exp\left[\frac{1}{2}i\int_0^X(P-G)\,dX\right]\right\} \tag{6}$$

where

$$G^2 = P^2 - 4\rho M - 4\rho\bar{H}\left(\frac{\dot{X}'}{\dot{X}}\right) + 4\left(\frac{\dot{X}'}{\dot{X}}\right)'$$
$$- 2\rho'\bar{H} + 4\rho'\left(\frac{A}{2m}C_{N_\alpha} - \frac{g}{\rho V^2}\right) - \rho^2\bar{H}^2$$
$$+ i\left[-4\rho P\bar{T} + 2\rho\bar{H}P - 2P\left(\frac{\dot{X}'}{\dot{X}}\right)\right]$$

Ignoring third and fourth order terms, G can be approximated as

$$G = (P^2 - 4\rho M)^{1/2} + i\frac{P}{(P^2 - 4\rho M)^{1/2}}$$
$$\times\left[\rho(\bar{H} = 2\bar{T}) - \left(\frac{\dot{X}'}{\dot{X}}\right)\right] \tag{7}$$

By relating this solution to the initial entry conditions (denoted by the subscript E) when the medium density is essentially zero, K_1 and K_2 are determined to be

$$K_1 = -\frac{i\,\xi_E'}{(2P_E)^{1/2}} \tag{8a}$$

$$K_2 = \frac{\xi_E(P_E)^{1/2} - i\frac{\xi_E}{(P_E)^{1/2}}}{2^{1/2}} \tag{8b}$$

However, these constants are valid only as long as the flight-path angle remains constant and would only be correct for a 90-deg entry. Nevertheless, six-degree-of freedom numerical calculations do indicate that the type of motion observed during the initial portion of entry continues through the terminal portion. For instance, if the capsule has no initial transverse angular velocity ($\xi'_E = 0$), K_1 will be zero and the motion will be essentially circular. The six-degree-of-freedom computation confirms this fact and further indicates that the circular motion will continue after the flight-path angle has changed appreciably.

For this analysis, it will be assumed (1) that the motion is initially circular, (2) that it remains circular near terminal conditions, and (3) that this is reflected in K_1 being zero at terminal conditions. Incorporating this assumption into Eq. (5) and using the approximate form of G, the equation defining the total angle of attack becomes

$$\xi = \xi_0 \frac{(P_0 - 4\rho_0 M)^{1/4}}{(P - 4\rho M)^{1/4}} \exp\left\{-\frac{1}{2}\int_0^X \left[\rho\bar{H} + 2\left(\frac{\dot{X}'}{\dot{X}}\right)\right] dX\right\}$$
$$\times \exp\left\{\frac{1}{2} i \int_0^X \left[P - (P^2 - 4\rho M)^{1/2} - i\frac{P\left\{\rho(\bar{H} - 2\bar{T}) - \left(\frac{\dot{X}'}{\dot{X}}\right)\right\}}{(P^2 - 4\rho M)^{1/2}}\right] dX\right\} \tag{9}$$

where the zero subscript refers to values at the beginning of terminal conditions. The angle-of-attack envelope is given by the amplitude portion of the solution:

$$\xi_{env} = \xi_{env_0} \frac{(P_0 - 4\rho_0 M)^{1/4}}{(P - 4\rho M)^{1/4}} \exp\left\{-\frac{1}{2}\int_0^X \left[\rho\bar{H} + 2\left(\frac{\dot{X}'}{\dot{X}}\right) - \frac{P}{(P^2 - 4\rho M)^{1/2}}\left\{\rho(\bar{H} - 2\bar{T}) - \left(\frac{\dot{X}'}{\dot{X}}\right)\right\}\right] dX\right\} \tag{10}$$

During terminal descent the divergence or convergence of the envelope is determined almost completely by the exponential term. The criteria for stability, then, is the integrand

$$\rho\bar{H} + 2\left(\frac{\dot{X}'}{\dot{X}}\right) - \frac{P}{(P^2 - 4\rho M)^{1/2}}\left[\rho(\bar{H} - 2\bar{T}) - \left(\frac{\dot{X}'}{\dot{X}}\right)\right] \tag{11}$$

where a positive value indicates stability and a negative value instability. Recalling that $\dot{X}'/\dot{X}$ during terminal descent is

$$-\rho\left[\frac{AC_D}{2m} - \frac{g}{\rho V^2}\right]$$

and noting that the velocity during terminal condition is equivalent to $V_0(\rho_0/\rho)^{1/2}$, the stability criteria can be put into the alternate form

$$\rho\left\{\bar{H} - \frac{AC_D}{m} + \frac{2g}{\rho V^2} - \frac{\frac{P_0}{\rho_0^{1/2}}}{\left(\frac{P_0^2}{\rho_0} - 4M\right)^{1/2}}\left[\bar{H} - 2\bar{T} + \frac{AC_D}{2m} - \frac{g}{\rho V^2}\right]\right\} \tag{12}$$

By incorporating the assumption of an exponentially changing density ($\rho - \rho_0 e^{\beta X}$) into the above equation and integrating the envelope equation (Eq. 10), the closed-form solution for the angle-of-attack envelope is obtained:

$$\frac{\xi_{env}}{\xi_{env_0}} = \frac{(P_0 - 4\rho_0 M)^{1/4}}{(P - 4\rho M)^{1/4}} \exp\left(\left[\frac{\rho - \rho_0}{\beta}\right]\left\{\bar{H} - \frac{AC_D}{m} + \frac{2g}{\rho V^2} - \frac{\frac{P_0}{\rho_0^{1/2}}}{\left(\frac{P_0^2}{\rho_0} - 4M\right)^{1/2}}\left[\bar{H} - 2\bar{T} + \frac{AC_D}{2m} - \frac{g}{\rho V^2}\right]\right\}\right) \tag{13}$$

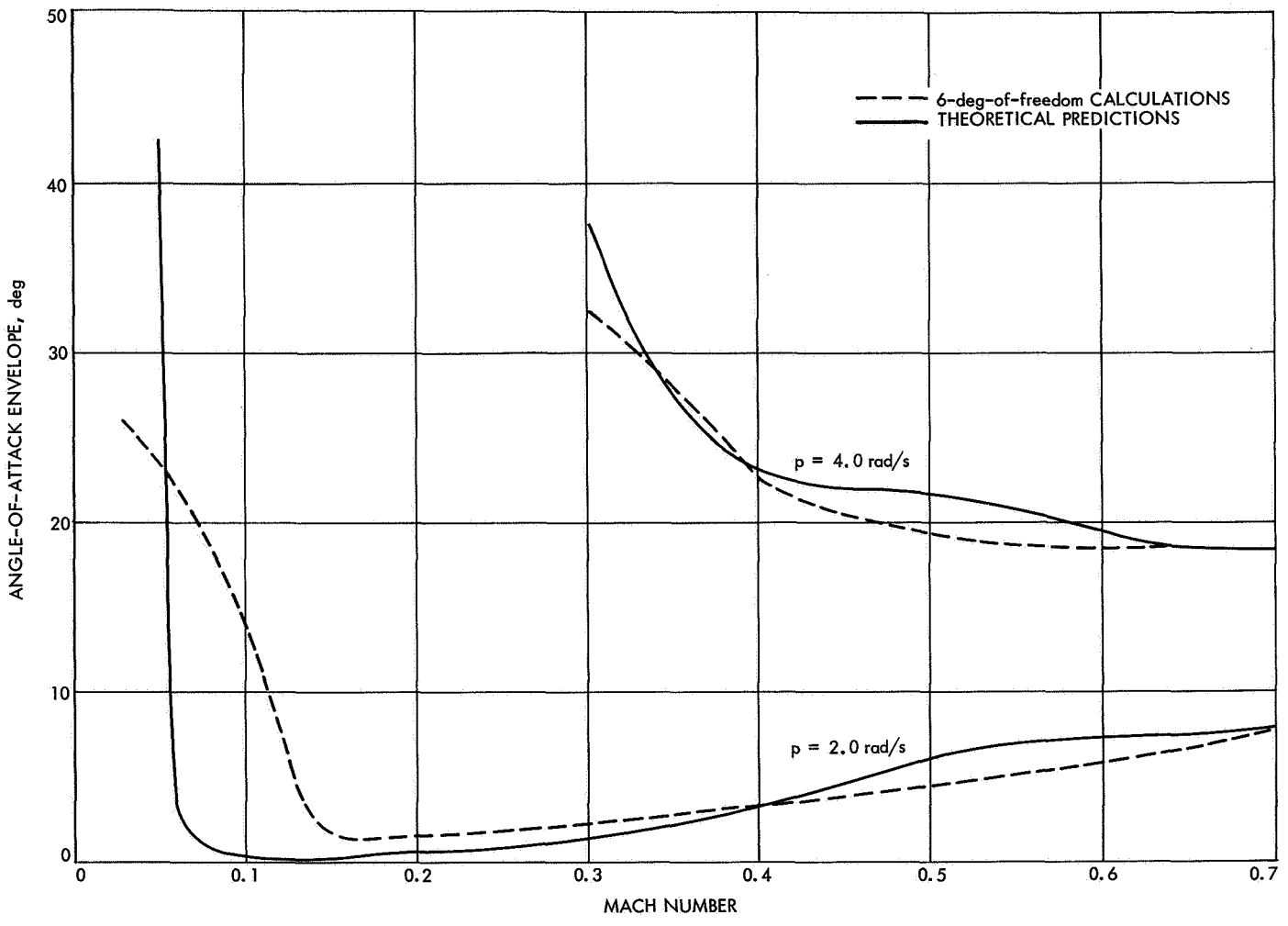

Fig. 12. Angle-of-attack envelope during terminal Venus entry

Figure 12 shows two applications of this solution for entry into a dense Venus 50-bar atmosphere. The lower pair of curves is for a roll rate of 2.0 rad/s and the upper curve for 4.0 rad/s. The dashed curves were generated with a six-degree-of-freedom computer program and the solid curves with Eq. (13). Although the analytic solutions deviated somewhat from the computer solutions, the predicted trends did agree quite well. Furthermore, the terminal dynamics of a particular entry body and mission lie in a precarious balance between stability and instability, where minute changes in the aerodynamic coefficients used could shift the balance from stability to instability or vice versa. For instance, if the dynamic stability coefficient were shifted negatively (toward greater stability) by 0.05 (which is about the accuracy to which this coefficient can be measured) from the values used, then calculations for both the 2.0- and 4.0-rad/s roll cases would demonstrate strong angle-of-attack stability for the entire terminal portion of entry. Similarly, if the coefficient were shifted positively by 0.05, catastrophic instability would be predicted for both cases at even higher Mach numbers. In attempting to determine the stability of a vehicle in this regime where small changes can have large effects, it is essential that appropriate accuracy tolerances of the aerodynamic coefficients, roll rate, and atmospheric definition be included in the analysis.

Reference

1. White, F. M., Jr., *The Use of the WKB Method in Applied Mechanics*, proceedings of the First Southwest Symposium on Applied Mechanics, Gatlinburg, Tenn., May 1962.

3. Estimates of the Aerodynamic Forces and Moments Acting on Parabolic Antennas in the Martian Surface Atmosphere[7]

Information obtained by a large scientific payload landed on Mars will probably be transmitted either via a relay system or directly back to earth. In either case, the antenna used on the landed vehicle could be a parabolic type, thus requiring aerodynamic considerations prior to final design. The purpose of this study was to set bounds on the magnitudes of the expected aerodynamic coefficients and, thus, the forces that would influence the design. The aerodynamic coefficient is defined as the aerodynamic force divided by the freestream dynamic pressure times the reference area. For this study the dynamic pressure was 5.95 psi and the area was 12.56 ft^2.

The three most dominant factors that determine the aerodynamic coefficients are: (1) shape and position of the antenna, (2) antenna geometric porosity, and (3) the Reynolds number of the flow around the antenna.

The extremes of possible shapes for the antenna are the flat plate and the hemisphere. The final shape will probably be somewhere in between but closer to the flat plate. The flat plate normal to the flow has a drag coefficient between 1.18 and 1.33, while the hemisphere has a coefficient of 1.4 to 1.6 (open end into flow). The drag coefficient for the latter shape will decrease whenever the antenna is not pointed directly into the wind.

A maximum sideforce coefficient of 1.4 occurs when the angle between the wind vector (see Fig. 13 for axis system) and the antenna centerline is 55 deg.

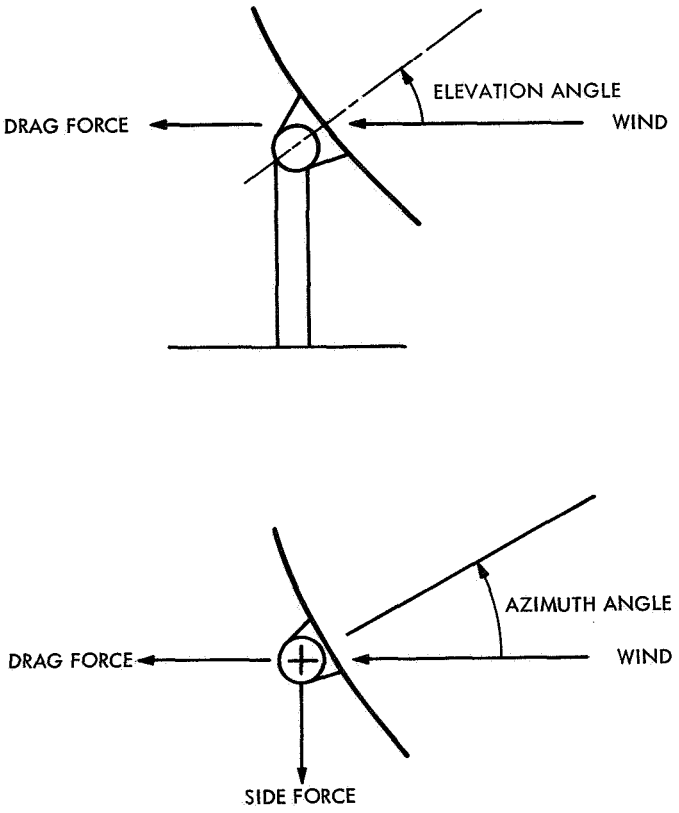

Fig. 13. Axis reference system

[7]Based on data obtained for anemometer cup design (Ref. 1) and drag body studies (Ref. 2). Results must necessarily be considered estimates.

When the antenna is at an angle to the wind, there is also a moment generated about the vertex of the antenna. The moment coefficient has a maximum value of 0.1 at about a 55-deg angle off the wind vector. Thus, the maximum force acting through the center of the antenna (assuming a 400-ft/s wind in the VM-10 Martian atmosphere) will be 120 lb at a zero-off-wind angle. Where the off-wind angle is 55 deg, the force is 110 lb perpendicular to the wind vector with a moment of 30 ft-lb also acting about the vertex. These values are for a zero-porosity antenna; an increase in porosity will result in lower forces (Fig. 14). The effect of porosity on the moment is not well known, but limited available information indicates that bilinear decreases can be expected.

An indirect effect on the forces can also occur depending on how the antenna is made porous. If one large hole is used, the effect on the forces will be different from those obtained if an infinite number of minute holes were drilled. The upper bound on the hole size will probably be set by antenna radiative power loss considerations but the minimum size hole will be determined for aerodynamic reasons.

As the wind flows through the holes in the antenna, a boundary layer is built up on the edges of the holes. If this boundary layer is too large (or the holes too small), the hole will be in a choked condition. When this choking occurs, the resulting forces will be equivalent to the forces on a much lower porosity configuration. Therefore, the size of the actual opening in the antenna must not be smaller than twice the expected boundary layer thickness. For a maximum expected boundary layer thickness of 0.1 in., the openings in the antenna must be at least 0.2 in.

References

1. Brevoort, M. J., and Joyner, U. T., *Experimental Investigation of the Robinson-Type Cup Anemometer,"* NACA No. 513. National Advisory Committee on Aeronautics, Washington, May 1935.

2. Hoerner, S. F., *Fluid Dynamic Drag,* published by the author (Library of Congress Catalog No. 57-13009), 1958.

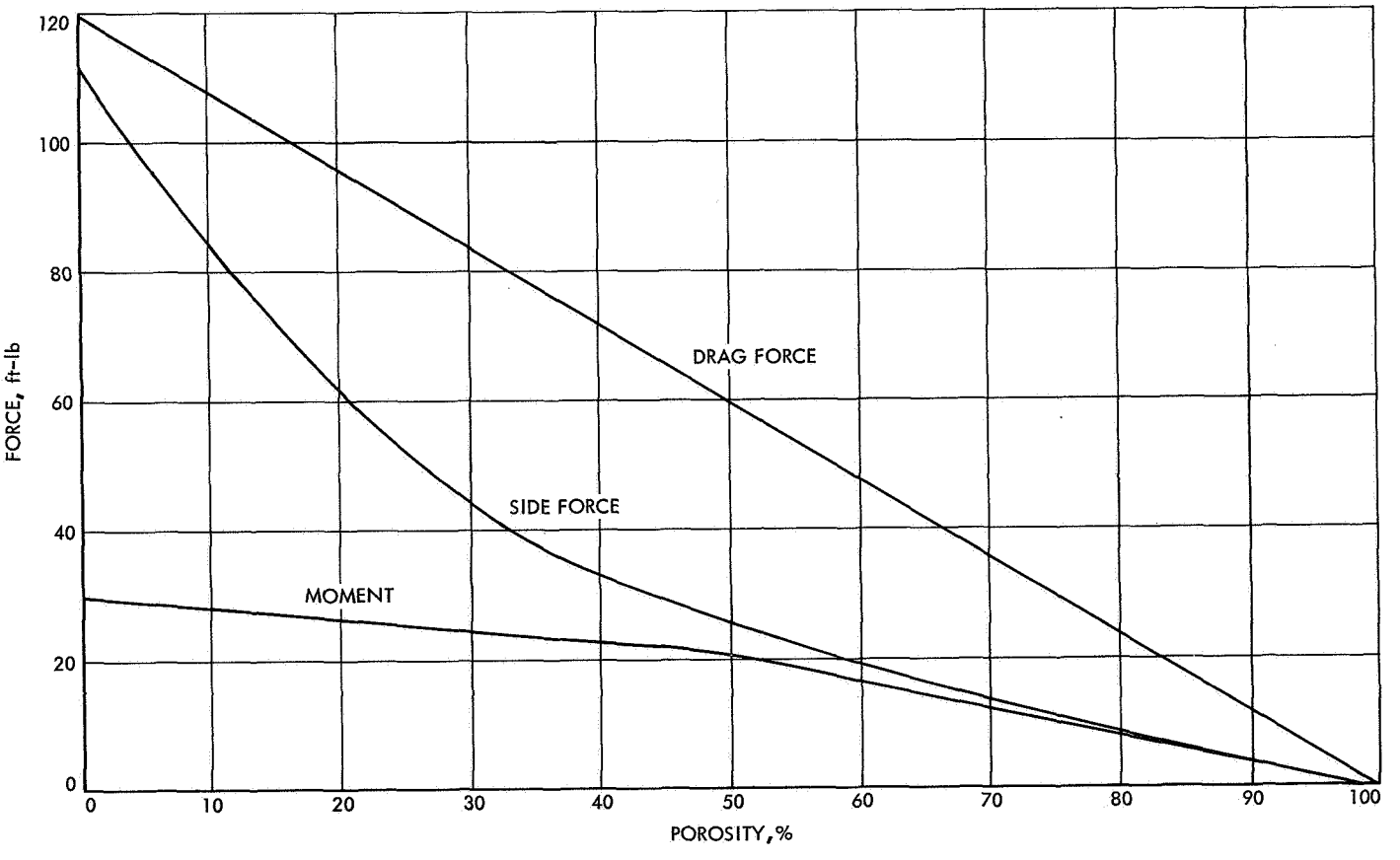

Fig. 14. Force versus antenna porosity